

A New Method for Indirect Mass Measurements using the Integral Charge Asymmetry at the LHC

G. Steve Muanza,¹ and Thomas Serre

*Aix Marseille Université, CNRS/IN2P3,
CPPM UMR 7346, Marseille, France*

E-mail: muanza@in2p3.fr

ABSTRACT: Processes producing a charged final state at the LHC have a positive or null integral charge asymmetry. We propose a novel method for an indirect measurement of the mass of these final states based upon the process integral charge asymmetry. We present this method in three stages. Firstly, the theoretical prediction of the integral charge asymmetry and its related uncertainties are studied through parton level cross sections calculations. Secondly, the experimental extraction of the integral charge asymmetry of a given signal, in the presence of some background, is performed using particle level simulations. Process dependent templates enable to convert the measured integral charge asymmetry into an estimated mass of the charged final state. Thirdly, a combination of the experimental and the theoretical uncertainties determines the full uncertainty of the indirect mass measurement. This new method applies to all charged current processes at the LHC. In this article, we demonstrate its effectiveness at extracting the mass of the W boson, as a first step, and the sum of the masses of a chargino and a neutralino in case these supersymmetric particles are produced by pair, as a second step.

¹Corresponding author.

Contents

1	Introduction	1
2	Inclusive Production of $W^\pm \rightarrow \ell^\pm \nu$	4
2.1	Theoretical Prediction of $A_C(W^\pm \rightarrow \ell^\pm \nu)$	4
2.1.1	Sources of Theoretical Uncertainties on A_C	4
2.1.2	Setup and Tools for the Computation of A_C	5
2.1.3	Modeling of the Theoretical $A_C(W^\pm \rightarrow e^\pm \nu_e)$ Template Curves	5
2.1.4	$A_C(W^\pm \rightarrow e^\pm \nu_e)$ Template Curves for MRST	6
2.1.5	$A_C(W^\pm \rightarrow e^\pm \nu_e)$ Template Curves for CTEQ6	8
2.1.6	$A_C(W^\pm \rightarrow e^\pm \nu_e)$ Template Curves for MSTW2008	8
2.1.7	Comparing the Different A_C Template Curves	9
2.2	Experimental Measurement of $A_C(W^\pm \rightarrow \ell^\pm \nu)$	11
2.2.1	Monte Carlo Generation	13
2.2.2	Fast Simulation of the Detector Response	14
2.2.3	Analyses of the $W^\pm \rightarrow \ell^\pm \nu$ Process	14
2.3	Indirect Determination of M_{W^\pm}	22
2.3.1	Results in the Individual Channels	22
2.3.2	Combination of the Electron and the Muon Channels	22
2.4	Final Result for MRST2007lomod	23
2.5	Final Results for the Other Parton Density Functions	23
2.6	Summary of the M_{W^\pm} Measurements and their Accuracy	27
3	Inclusive Production of $\tilde{\chi}_1^\pm + \tilde{\chi}_2^0 \rightarrow 3\ell^\pm + \cancel{E}_T$	28
3.1	Theoretical Prediction of $A_C(\tilde{\chi}_1^\pm + \tilde{\chi}_2^0)$	28
3.1.1	$A_C(\tilde{\chi}_1^\pm + \tilde{\chi}_2^0)$ Template Curves for MRST	29
3.1.2	$A_C(\tilde{\chi}_1^\pm + \tilde{\chi}_2^0)$ Template Curves for CTEQ6	30
3.1.3	$A_C(\tilde{\chi}_1^\pm + \tilde{\chi}_2^0)$ Template Curves for MSTW2008	35
3.1.4	Comparing the different A_C Template Curves	36
3.2	Experimental Measurement of $A_C(\tilde{\chi}_1^\pm + \tilde{\chi}_2^0 \rightarrow 3\ell^\pm + \cancel{E}_T)$	37
3.2.1	Monte Carlo Generation	39
3.2.2	Analysis of the $\tilde{\chi}_1^\pm \tilde{\chi}_2^0 \rightarrow 3\ell^\pm + \cancel{E}_T$ Process	40
3.3	Indirect Determination of $M_{\tilde{\chi}_1^\pm} + M_{\tilde{\chi}_2^0}$	43
3.3.1	Experimental Result for the S1 Signal	43
3.3.2	Experimental Result for the S2 Signal	44
3.4	Final Result for MRST2007lomod	50
3.4.1	Final Result for the S1 Signal	50
3.4.2	Final Result for the S2 Signal	51
3.5	Summary of the $M_{\tilde{\chi}_1^\pm} + M_{\tilde{\chi}_2^0}$ Measurements and their Accuracy	51
3.6	Comparison with Other Mass Measurement Methods	54
3.6.1	Dilepton Mass Edge	54

3.6.2	Stransverse Mass End-Point	59
4	Conclusions	78
5	Prospects	79
A	Appendix: Toy Models for the Evolution of A_C	81
A.1	Numerical Example of Evolution of the PDFs, the Quark Currents and A_C	81
A.2	Toy Models for the Main Properties of A_C^{Fit}	81
A.2.1	Polynomials of $Log(x)$	83
A.2.2	Polynomials of $Log(Log(x))$	84
A.2.3	Laguerre Polynomials $L_n(x)$	84

1 Introduction

Contrarily to most of the previous high energy particle colliders, the LHC is a charge asymmetric machine. For charged final states ¹, denoted FS^\pm , the integral charge asymmetry, denoted A_C , is defined by

$$A_C = \frac{N(FS^+) - N(FS^-)}{N(FS^+) + N(FS^-)} \quad (1.1)$$

where $N(FS^+)$ and $N(FS^-)$ represent respectively the number of events bearing a positive and a negative charge in the FS.

For a FS^\pm produced at the LHC in $p + p$ collisions, this quantity is positive or null, whilst it is always compatible with zero for a FS^\pm produced at the TEVATRON in $p + \bar{p}$ collisions.

To illustrate the A_C observable, let's consider the Drell-Yan production of W^\pm bosons in $p + p$ collisions. It is obvious for this simple $2 \rightarrow 2$ s-channel process that more W^+ than W^- are produced. Indeed, denoting y_W the rapidity of the W boson, the corresponding range of the Björken x's: $x_{1,2} = \frac{M_{W^\pm}}{\sqrt{s}} \times e^{\pm y_W}$, probes the charge asymmetric valence parton densities within the proton. This results in having more $U + \bar{D} \rightarrow W^+$ than $\bar{U} + D \rightarrow W^-$ configurations in the initial state (IS). Here U and D collectively and respectively represent the up and the down quarks.

In the latter case the dominant contribution to A_C comes from the difference in rate between the $u + \bar{d}$ and the $d + \bar{u}$ quark currents in the IS. Using the usual notation $f(x, Q^2)$ for the parton density functions (PDF) and within the leading order (LO) approximation, this can be expressed as:

¹We defined these as event topologies containing an odd number of high p_T charged and isolated leptons within the fiducial volume of the detector.

$$A_C \approx \frac{u(x_{1,2}, M_W^2) \bar{d}(x_{2,1}, M_W^2) - \bar{u}(x_{1,2}, M_W^2) d(x_{2,1}, M_W^2)}{u(x_{1,2}, M_W^2) \bar{d}(x_{2,1}, M_W^2) + \bar{u}(x_{1,2}, M_W^2) d(x_{2,1}, M_W^2)} \quad (1.2)$$

where the squared four-momentum transfer Q^2 is set to M_W^2 .

From equation 1.2, we can see that the Q^2 evolution of the parton density functions (PDFs) governs the Q^2 evolution of A_C . The former are known, up-to the NNLO in QCD, as solutions of the DGLAP equations [2]. One could therefore think of using an analytical functional form to relate A_C to the squared mass of the s-channel propagator, here M_W^2 . However there are additional contributions to the W^\pm inclusive production. At the Born level, some come from other flavour combinations in the IS of the s-channel, and some come from the u-channel and the t-channel. On top of this, there are higher order corrections. These extra contributions render the analytical expression of the Q^2 dependence of A_C much more complicated. Therefore we choose to build process-dependent numerical mass template curves for A_C by varying M_{FS^\pm} . These mass templates constitute inclusive and flexible tools into which all the above-mentioned contributions to A_C can be incorporated, they can very easily be built within restricted domain of the signal phase space imposed by kinematic cuts.

The A_C for the $W^\pm \rightarrow \ell^\pm \nu$ production at the LHC is large enough to be measured and it has relatively small systematic uncertainties since it's a ratio of cross sections. The differential charge asymmetry of this process in $p + p$ collisions have indeed been measured by the ATLAS [3], the CMS [4] [5] and the LHCb [6] experiments [7] for the first times in their 2011 datasets.

In this article we exploit the A_C to set a new type of constraint on the mass of the charged FS^\pm as initially proposed in [10][11].

We'll separate the study into two parts. The first one, in section 2, is dedicated to present in full length the method of indirect mass measurement that we propose on a known Standard Model (SM) process. We choose the $W^\pm \rightarrow \ell^\pm + \cancel{E}_T$ inclusive production at the LHC to serve as a test bench.

In the second part, in section 3, we shall repeat the method on a "Beyond the Standard Model" (BSM) process. We choose a SUSY search process of high interest, namely

$$\tilde{\chi}_1^\pm + \tilde{\chi}_2^0 \rightarrow 3\ell^\pm + \cancel{E}_T. \quad (1.3)$$

For both the SM and the BSM processes, we obviously tag the sign of the FS by choosing a decay into one (or three) charged lepton(s) for which the sign is experimentally easily accessible.

It's obvious that for these two physics cases other mass reconstruction methods exist. These standard mass reconstruction techniques are all based on the kinematics of the FS. For the $W^\pm \rightarrow \ell^\pm + \cancel{E}_T$ process mass templates based upon the transverse mass allow to extract M_{W^\pm} with an excellent precision that the new technique proposed here cannot match. In contrast, for the $\tilde{\chi}_1^\pm + \tilde{\chi}_2^0 \rightarrow 3\ell^\pm + \cancel{E}_T$ process, even if astute extensions of the transverse mass enable to accurately measure some mass differences, no standard techniques is able to measure accurately the mass of the charged FS: $M_{FS^\pm} = M_{\tilde{\chi}_1^\pm} + M_{\tilde{\chi}_2^0}$.

Therefore this new mass reconstruction technique should not be viewed as an alternative to the standard techniques but rather as an unmined complement to them. In a few cases, especially where many FS particles escape detection, this new technique can be more accurate than the standard ones. It also has the advantage of being almost model independent.

For each signal process we sub-divide the method into four steps that are described in four sub-sections. In the first sub-sections 2.1 and 3.1, we start by deriving the theoretical A_C template curves at the parton level.

In the second sub-sections 2.2 and 3.2, we place ourselves in the situation of an experimental measurement of the A_C of the signal in the presence of some background. For that we generate samples of Monte Carlo (MC) events that we reconstruct using a fast simulation of the response of the ATLAS detector. This enables to account for the bias of the signal A_C induced by the event selection. In addition we can quantify the bias of A_C due to the residual contribution of some background processes passing this event selection.

Then, in the third sub-sections 2.3 and 3.3, we convert the measured A_C into an estimated M_{FS} using fitted experimental A_C template curves that account for all the experimental uncertainties.

In the fourth sub-sections 2.4 and 3.4, we combine the theoretical and the experimental uncertainties on the signal A_C to derive the full uncertainty of the indirect mass measurement. The conclusions are presented in section 4 and the prospects in section 5.

Note that we'll always express the integral charge asymmetry in % and the mass of the charged final state in GeV throughout this article. The uncertainty on the integral charge asymmetry δA_C will also be expressed in % but will always represent an absolute uncertainty as opposed to a relative uncertainty with respect to A_C .

2 Inclusive Production of $W^\pm \rightarrow \ell^\pm \nu$

2.1 Theoretical Prediction of $A_C(W^\pm \rightarrow \ell^\pm \nu)$

In this section we calculate separately the cross sections of the "signed processes", i.e. the cross sections of the positive and negative FS: $\sigma^+ = \sigma(p + p \rightarrow W^+ \rightarrow \ell^+ \nu)$ and $\sigma^- = \sigma(p + p \rightarrow W^- \rightarrow \ell^- \bar{\nu})$. The process integral charge asymmetry therefore writes:

$$A_C = \frac{\sigma^+ - \sigma^-}{\sigma^+ + \sigma^-} \quad (2.1)$$

2.1.1 Sources of Theoretical Uncertainties on A_C

Since these cross sections integration are numerical rather than analytical, they each have an associated statistical uncertainty $\delta\sigma_{Stat}^\pm$ due to the finite sampling of the process phase space. Even though these are relatively small we explicitly include them and we calculate the resulting statistical uncertainty on the process integral charge asymmetry: $\delta(A_C)_{Stat}$ for which we treat $\delta\sigma_{Stat}^+$ and $\delta\sigma_{Stat}^-$ as uncorrelated uncertainties. Hence:

$$\delta(A_C)_{Stat} = \frac{2}{(\sigma^+ + \sigma^-)^2} \sqrt{(\sigma^- \cdot \delta\sigma_{Stat}^+)^2 + (\sigma^+ \cdot \delta\sigma_{Stat}^-)^2} \quad (2.2)$$

For each cross section calculation we choose the central Parton Density Function (PDF) from a PDF set (or just the single PDF when there's no associated uncertainty set). Whenever we use a PDF set, it contains $2N_{PDF}$ uncertainty PDFs on top of the central PDF fit, the PDF uncertainty is calculated as proposed in [23]:

$$\begin{cases} \delta(A_C)_{PDF}^{Up} = \sqrt{\sum_{i=1}^{N_{PDF}} (Max[A_C(i)^{up} - A_C(0), A_C(i)^{down} - A_C(0), 0])^2} \\ \delta(A_C)_{PDF}^{Down} = \sqrt{\sum_{i=1}^{N_{PDF}} (Max[A_C(0) - A_C(i)^{up}, A_C(0) - A_C(i)^{down}, 0])^2} \end{cases} \quad (2.3)$$

where $A_C(0)$, $A_C(i)^{up}$, and $A_C(i)^{down}$ represent the integral charge asymmetries calculated with σ_0 , σ_i^{up} , and σ_i^{down} , respectively. σ_0 represents the cross section calculated with the central PDF fit. σ_i^{up} represent the N_{PDF} upward uncertainty PDFs such that generally $\sigma_i^{up} > \sigma_0$, and σ_i^{down} represent the N_{PDF} downward uncertainty PDFs such that generally $\sigma_i^{down} < \sigma_0$.

We choose the QCD renormalization and factorization scales: $\mu_R = \mu_F = \mu_0$ to be equal, and we choose a process dependent dynamical option to adjust the value of μ_0 to the actual kinematics event by event. The scale uncertainty is evaluated using the usual factors 1/2 and 2 to calculate variations with respect to the central value μ_0 :

$$\begin{cases} \delta(A_C)_{Scale}^{Up} = A_C(\mu_0/2) - A_C(\mu_0) \\ \delta(A_C)_{Scale}^{Down} = A_C(2\mu_0) - A_C(\mu_0) \end{cases} \quad (2.4)$$

The total theoretical uncertainty is defined as the sum in quadrature of the 3 sources:

$$\begin{cases} \delta(A_C)_{Total}^{Up} = \sqrt{[\delta(A_C)_{PDF}^{Up}]^2 + [\delta(A_C)_{Scale}^{Up}]^2 + [\delta(A_C)_{Stat}]^2} \\ \delta(A_C)_{Total}^{Down} = \sqrt{[\delta(A_C)_{PDF}^{Down}]^2 + [\delta(A_C)_{Scale}^{Down}]^2 + [\delta(A_C)_{Stat}]^2} \end{cases} \quad (2.5)$$

2.1.2 Setup and Tools for the Computation of A_C

We calculate the $\sigma^+ = \sigma(p + p \rightarrow W^+ \rightarrow \ell^+ \nu)$ and $\sigma^- = \sigma(p + p \rightarrow W^- \rightarrow \ell^- \bar{\nu})$ cross sections and their uncertainties at $\sqrt{s} = 7$ TeV using MCFM v5.8 [33][34][35]. We include both the $W^\pm + 0Lp$ and the $W^\pm + 1Lp$ matrix elements (ME) in the calculation in order to have a better representation of the W^\pm inclusive production (the notation "Lp" stands for "light parton", i.e. u/d/s quarks or gluons). We set the QCD scales as $\mu_R = \mu_F = \mu_0 = \sqrt{M^2(W^\pm) + p_T^2(W^\pm)}$ and we run the calculation at the QCD leading order (LO) and next-to-leading order (NLO). For both the phase space pre-sampling and the actual cross section integration, we run 10 times 20,000 sweeps of VEGAS [12]. We impose the following parton level cuts: $M(\ell^\pm \nu) > 10$ GeV, $|\eta(\ell^\pm)| < 2.4$ and $p_T(\ell^\pm) > 20$ GeV. We artificially vary the input mass of the W^\pm boson and we repeat the computations for the 3 following couples of respective LO and NLO PDFs: MRST2007lomod [19] - MRST2004nlo [20], CTEQ6L1 [17] - CTEQ6.6 [18], and MSTW2008lo68cl - MSTW2008nlo68cl [22] which are interfaced to MCFM through LHAPDF v5.7.1 [24]. As the LO is sufficient to present the method in detail, we'll restrict ourselves to LO MEs and LO PDFs throughout the article for the sake of simplicity. We shall however provide the theoretical A_C mass templates up to the NLO for the W process. And we recommend to establish them using the best theoretical calculations available for any use in a real data analysis, including at the minimum the QCD NLO corrections.

The MRST2007lomod is chosen as the default PDF throughout this article. The two other LO PDFs serve for comparison of the central value and the uncertainty of A_C with respect to MRST2007lomod. In that regard, MSTW2008lo68cl is especially useful to estimate the impact of the $\delta(A_C)_{PDF}$.

2.1.3 Modeling of the Theoretical $A_C(W^\pm \rightarrow e^\pm \nu_e)$ Template Curves

The theoretical MRST2007lomod and MRST2004nlo raw template curves are obtained by sampling A_C^{Raw} at different values of M_{W^\pm} . The corresponding theoretical uncertainties are also calculated: $A_C^{Raw} \pm \delta A_C^{Raw}$. This discrete sampling is then transformed into a continuous template curve through a fit using a functional form $A_C^{Fit} = f(M_{W^\pm})$ which is constrained by the theoretical uncertainties.

We have considered three different types of functional forms for these fits with f being either a:

1. polynomial of logarithms: $f(x) = \sum_{i=0}^{N_{FP}} A_i \times \{Log(x)\}^i$
2. polynomial of logarithms of logarithms: $f(x) = \sum_{i=0}^{N_{FP}} A_i \times \{Log[Log(x)]\}^i$

3. series of Laguerre polynomials: $f(x) = \sum_{i=0}^{N_{FP}} A_i \times L_n(x)$ where $L_n(x) = \frac{e^x}{n!} \frac{d^n}{dx^n} (e^{-x} x^n)$.

The types of functional forms that we're considering are not arbitrary, they are all related to parametrizations of solutions of the DGLAP equations for the evolution of the PDFs. The polynomial of logarithms of logarithms is inspired by an expansion of the PDF in series of $\text{Log}[\text{Log}(Q^2)]$ as suggested in [2]. The polynomial of logarithms was just the simplest approximation of the aforementioned series that we first considered. And the expansion of the PDF in series of Laguerre polynomials is proposed in [8].

In the Appendix A, we give a numerical example of the evolution of the $u(x, Q^2)$, $\bar{u}(x, Q^2)$, $d(x, Q^2)$, $\bar{d}(x, Q^2)$ proton density functions calculated with QCDNUM [9] and the MSTW2008nlo68cl PDF. We also provide a few toy models to justify the main properties of the functional forms used for A_C^{Fit} .

Ultimately, the model of the theoretical template curve uses the functional form f for the A_C^{Fit} central values and re-calculate their uncertainty δA_C^{Fit} by accounting for the correlations between the uncertainties of the fit parameters:

$$(\delta A_C^{Fit})^2 = (\delta f)^2 = \sum_{i=0}^{N_{FP}} \sum_{j>i}^{N_{FP}} \left(\frac{\partial f}{\partial A_i} \right)^2 \cdot \text{VAR}(A_i) + 2 \cdot \frac{\partial f}{\partial A_i} \cdot \frac{\partial f}{\partial A_j} \cdot \text{COVAR}(A_i, A_j) \quad (2.6)$$

The diagonal and off-diagonal elements of the fit uncertainty matrix are denoted $\text{VAR}(A_i)$ and $\text{COVAR}(A_i, A_j)$, they correspond to the usual variances of the parameters and the covariances amongst them, respectively.

The number of fit parameters N_{FP} is taken as the minimum integer necessary to get a good χ^2/N_{dof} for the fit and it is adjustable for each A_C template curve.

Comparing the three types of polynomials cited above as functional forms to fit all the A_C template curves of sub-sections 2.1 and 3.1, we find that the polynomials of logarithms of logarithms of Q give the best fits. They are henceforth chosen as the default functional form to model the Q evolution of A_C throughout this article.

2.1.4 $A_C(W^\pm \rightarrow e^\pm \nu_e)$ Template Curves for MRST

The theoretical MRST2007lomod and MRST2004nlo A_C template curves are obtained from the signed cross sections used for table 1. Since there is no MRST2007lomod PDF uncertainty set, we simply set $\delta(A_C)_{PDF} = 0$. In this case, $\delta_{Total}^{Theory} A_C = \sqrt{\delta_{Stat}^2 A_C + \delta_{Scale}^2 A_C}$. Figure 1 displays the fit to the A_C template curve using a polynomial of $\text{Log}(\text{Log}(Q))$. In the case of the MRST2007lomod PDF, it is sufficient to limit the polynomial to the degree $N_{FP} = 5$ to fit the A_C template curve in the following (default) range: $M_{W^\pm} \in [15, 1500]$ GeV.

M_{W^\pm} (GeV)	A_C (%)	$\delta(A_C)_{Stat}$ (%)	$\delta(A_C)_{Scale}$ (%)	$\delta(A_C)_{PDF}$ (%)	$\delta(A_C)_{Total}$ (%)
20.1	LO: 2.20	± 0.24	$+0.47$ $+0.10$	0.00	$+0.52$ -0.26
	NLO: 2.09	± 0.11	$+0.04$ -0.14	0.00	$+0.12$ -0.18
40.2	LO: 6.77	± 0.12	$+0.02$ -0.11	0.00	$+0.12$ -0.16
	NLO: 8.05	± 0.07	-0.18 -0.06	0.00	$+0.19$ -0.09
<u>80.4</u>	LO: 20.18	± 0.06	$+0.05$ -0.03	0.00	$+0.08$ -0.07
	NLO: 21.49	± 0.03	-0.08 -0.00	0.00	$+0.09$ -0.03
160.8	LO: 29.39	± 0.05	$+0.00$ $+0.03$	0.00	$+0.05$ -0.06
	NLO: 30.55	± 0.03	-0.02 -0.01	0.00	$+0.04$ -0.03
321.6	LO: 35.92	± 0.05	-0.11 $+0.10$	0.00	$+0.11$ -0.11
	NLO: 36.90	± 0.03	-0.05 -0.04	0.00	$+0.06$ -0.05
643.2	LO: 43.99	± 0.05	-0.14 $+0.13$	0.00	$+0.15$ -0.14
	NLO: 45.11	± 0.03	-0.05 -0.05	0.00	$+0.06$ -0.06
1286.4	LO: 52.36	± 0.06	$+0.03$ -0.02	0.00	$+0.07$ -0.07
	NLO: 55.33	± 0.04	$+0.01$ -0.02	0.00	$+0.04$ -0.04

Table 1. The MRST A_C table with the breakdown of the different sources of theoretical uncertainty. The MRST2007lomod PDF is used for the LO and the MRST2004nlo for the NLO.

M_{W^\pm} (GeV)	A_C^{Fit} (%)	δA_C^{Fit} (%)
20.1	LO: 1.35	± 0.10
	NLO: 2.00	± 0.12
40.2	LO: 7.27	± 0.07
	NLO: 8.31	± 0.08
<u>80.4</u>	LO: 19.93	± 0.05
	NLO: 21.12	± 0.05
160.8	LO: 29.46	± 0.04
	NLO: 30.49	± 0.04
321.6	LO: 36.29	± 0.04
	NLO: 37.29	± 0.04
643.2	LO: 43.07	± 0.05
	NLO: 44.61	± 0.04
1286.4	LO: 52.43	± 0.06
	NLO: 55.40	± 0.04

Table 2. The MRST A_C^{Fit} table with δA_C^{Fit} calculated using Eq. 2.6. The MRST2007lomod PDF is used at LO and the MRST2004nlo one is used at NLO.

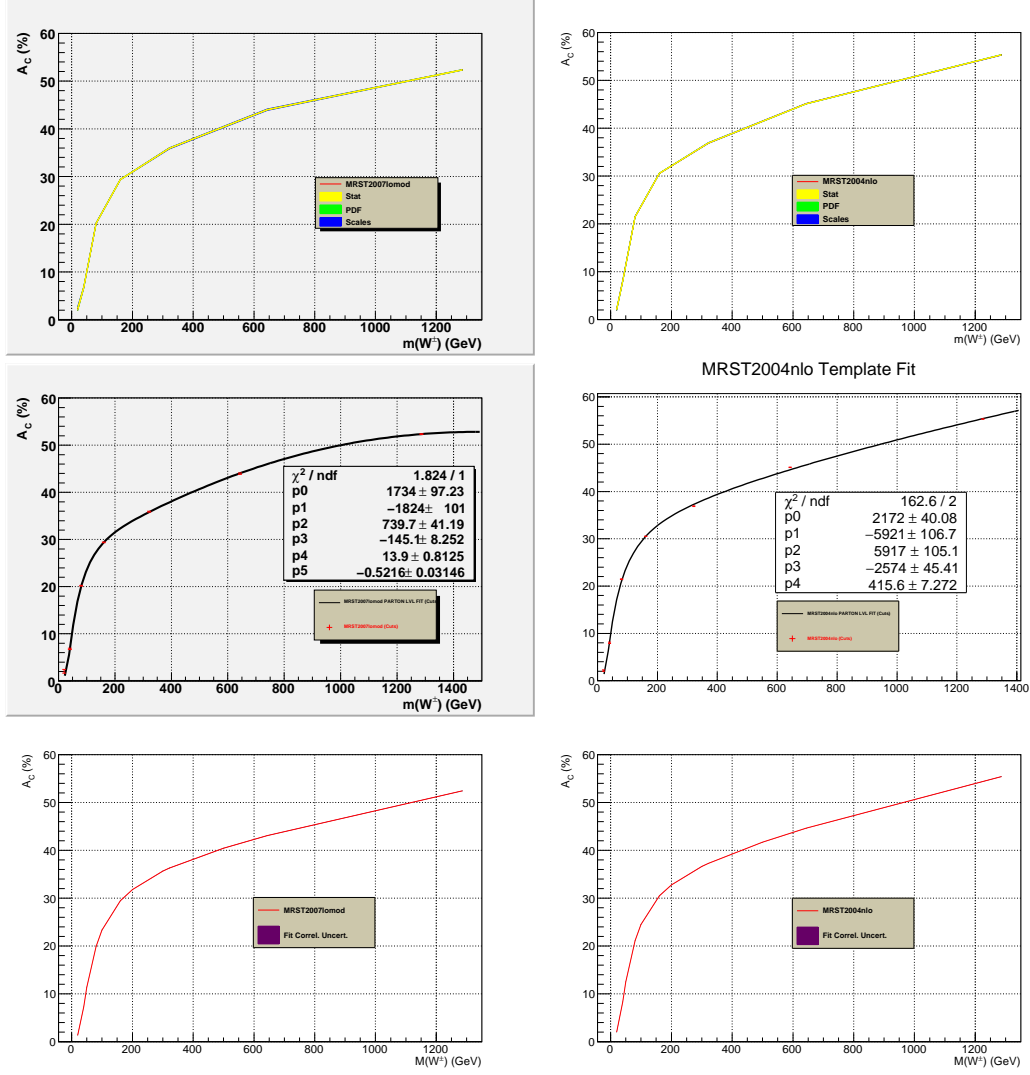


Figure 1. The theoretical MRST A_C template curves at LO with MRST2007lomod on the left-hand side (LHS) and NLO with the MRST2004nlo on the right-hand side (RHS). The raw curve with its uncertainty bands, the corresponding fitted curve and the fitted curve with the correlations between the fit parameters uncertainties are displayed on the top, the middle and the bottom rows, respectively.

2.1.5 $A_C(W^\pm \rightarrow e^\pm \nu_e)$ Template Curves for CTEQ6

The theoretical CTEQ6L1 and CTEQ6.1 A_C template curves are obtained from the signed cross sections used for table 3.

2.1.6 $A_C(W^\pm \rightarrow e^\pm \nu_e)$ Template Curves for MSTW2008

The theoretical MSTW2008lo68cl and MSTW2008nlo68cl A_C template curves are obtained from the signed cross sections used for table 5.

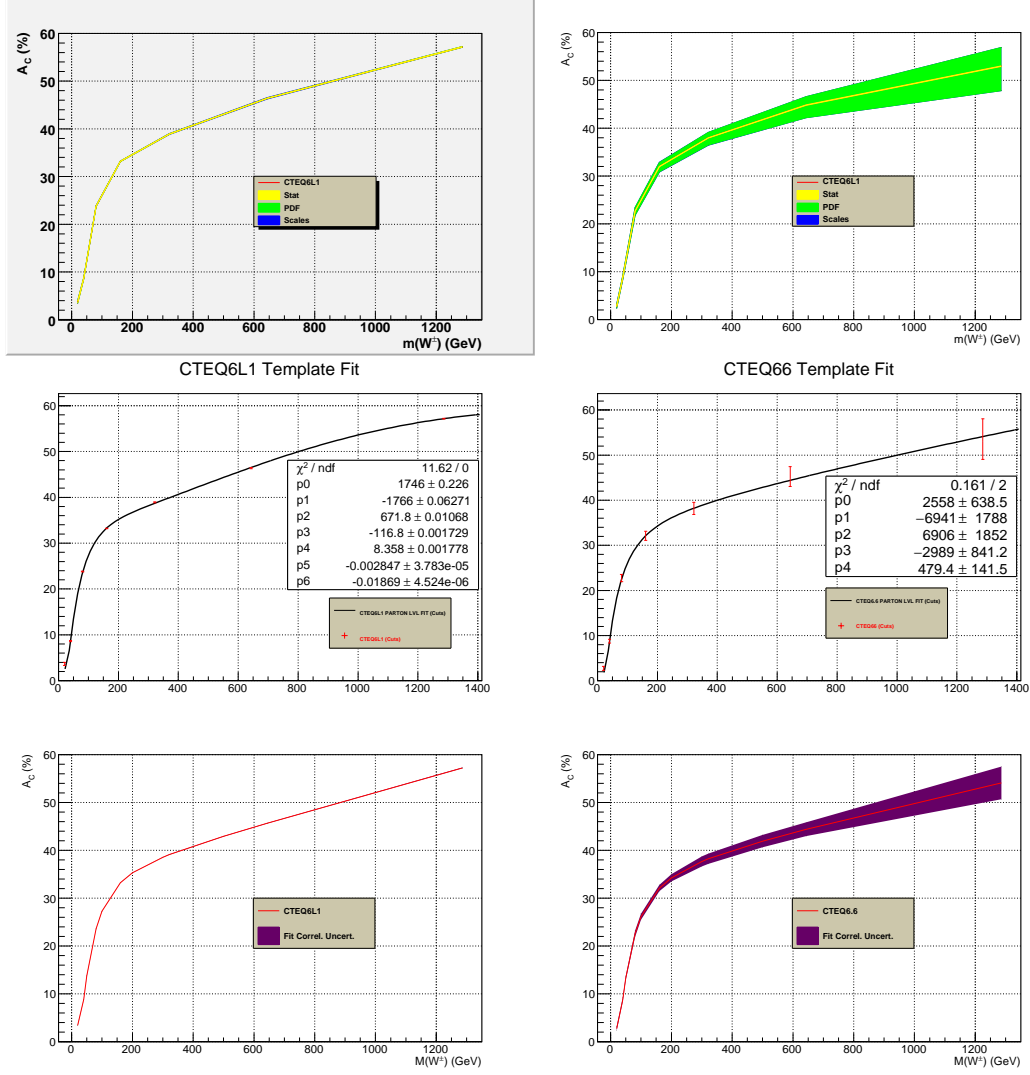


Figure 2. The theoretical CTEQ6 A_C template curves at LO with CTEQ6L1 (LHS) and NLO with the CTEQ6.6 (RHS). The raw curve with its uncertainty bands, the corresponding fitted curve and the fitted curve with the correlations between the fit parameters uncertainties are displayed on the top, the middle and the bottom rows, respectively.

In this case, the PDF uncertainty is provided and it turns out to be the dominant source of theoretical uncertainty on A_C .

2.1.7 Comparing the Different A_C Template Curves

At this stage, it's interesting to compare the A_C template curves produced with different PDFs using MCFM. From figure 4 we can see that the A_C of the different PDF used at LO and at NLO are in agreement at the $\pm 2\sigma$ level, provided that we switch the reference to a PDF set containing uncertainty PDFs. This figure also displays the $\frac{A_C^{NLO}}{A_C^{LO}}$ ratios for

M_{W^\pm} (GeV)	A_C (%)	$\delta(A_C)_{Stat}$ (%)	$\delta(A_C)_{Scale}$ (%)	$\delta(A_C)_{PDF}$ (%)	$\delta(A_C)_{Total}$ (%)
20.1	LO: 3.70 NLO: 2.76	± 0.24 ± 0.11	-0.27 $+0.11$ -0.24 -0.13	0.00 $+0.37$ -0.39	$+0.36$ -0.26 $+0.45$ -0.43
40.2	LO: 8.65 NLO: 8.75	± 0.12 ± 0.07	-0.02 -0.00 $+0.09$ -0.09	0.00 $+0.38$ -0.41	$+0.12$ -0.12 $+0.40$ -0.43
<u>80.4</u>	LO: 23.81 NLO: 22.67	± 0.06 ± 0.03	$+0.07$ -0.06 $+0.14$ -0.20	0.00 $+0.74$ -0.85	$+0.09$ -0.08 $+0.75$ -0.87
160.8	LO: 33.21 NLO: 31.99	± 0.05 ± 0.02	$+0.01$ -0.00 $+0.23$ -0.24	0.00 $+0.86$ -1.11	$+0.05$ -0.05 $+0.89$ -1.14
321.6	LO: 38.90 NLO: 37.99	± 0.05 ± 0.03	-0.09 $+0.07$ $+0.18$ -0.18	0.00 $+1.11$ -1.52	$+0.10$ -0.09 $+1.12$ -1.53
643.2	LO: 46.38 NLO: 44.83	± 0.05 ± 0.03	-0.14 0.13 $+0.06$ -0.09	0.00 $+1.76$ -2.64	$+0.15$ -0.14 $+1.76$ -2.64
1286.4	LO: 57.17 NLO: 52.97	± 0.06 ± 0.04	-0.06 $+0.06$ $+0.05$ $+0.04$	0.00 $+3.90$ -5.10	$+0.08$ -0.08 $+3.90$ -5.10

Table 3. The CTEQ6 A_C table with the breakdown of the different sources of theoretical uncertainty. The CTEQ6L1 PDF is used at LO and the CTEQ6.6 one is used at NLO.

M_{W^\pm} (GeV)	A_C^{Fit} (%)	δA_C^{Fit} (%)
20.1	LO: 3.40 NLO: 2.76	± 0.09 ± 0.44
40.2	LO: 8.85 NLO: 8.76	± 0.06 ± 0.42
<u>80.4</u>	LO: 23.59 NLO: 22.57	± 0.04 ± 0.64
160.8	LO: 33.24 NLO: 32.11	± 0.04 ± 0.66
321.6	LO: 39.11 NLO: 38.23	± 0.04 ± 1.08
643.2	LO: 45.67 NLO: 44.41	± 0.05 ± 1.43
1286.4	LO: 57.24 NLO: 54.11	± 0.07 ± 3.42

Table 4. The CTEQ6 A_C^{Fit} table with δA_C^{Fit} calculated using Eq. 2.6. The CTEQ6L1 PDF is used at LO and the CTEQ6.6 one is used at NLO.

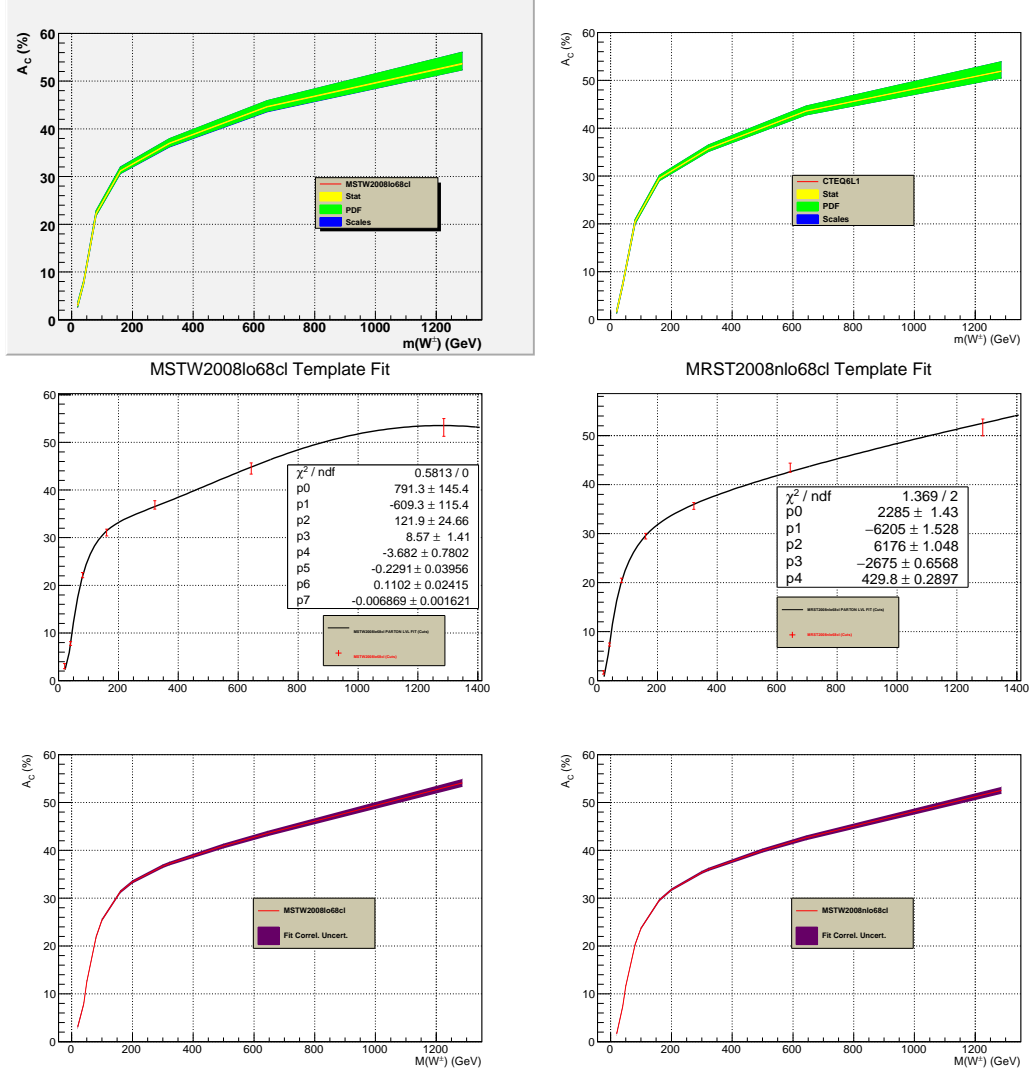


Figure 3. The theoretical MSTW2008 A_C template curves at LO with MSTW2008lo68cl (LHS) and NLO with the MSTW2008nlo68cl (RHS). The raw curve with its uncertainty bands and the corresponding fitted curve are displayed on the LHS and on the RHS, respectively.

the three families of PDFs used. These ratios are almost flat with respect to M_{W^\pm} over the largest part of our range of interest. However at the low mass ends they vary rapidly. As we illustrate in the Appendix A, these integral charge asymmetry ratios can be fitted by the same functional forms as the A_C^{LO} and A_C^{NLO} .

2.2 Experimental Measurement of $A_C(W^\pm \rightarrow \ell^\pm \nu)$

The aim of this sub-section is to study the biases on A_C due to two different sources: the event selection and the residual background remaining after the latter cuts are applied.

M_{W^\pm} (GeV)	A_C (%)	$\delta(A_C)_{Stat}$ (%)	$\delta(A_C)_{Scale}$ (%)	$\delta(A_C)_{PDF}$ (%)	$\delta(A_C)_{Total}$ (%)
20.1	LO: 3.07	± 0.24	-0.21	$+0.46$	$+0.56$
	NLO: 1.64	± 0.12	$+0.14$ -0.08 -0.17	-0.40 $+0.29$ -0.31	-0.49 $+0.32$ -0.37
40.2	LO: 7.85	± 0.12	$+0.10$	$+0.43$	$+0.46$
	NLO: 7.35	± 0.07	$+0.07$ $+0.05$ -0.06	-0.33 $+0.30$ -0.33	-0.36 $+0.31$ -0.34
<u>80.4</u>	LO: 22.24	± 0.06	$+0.15$	$+0.64$	$+0.66$
	NLO: 20.47	± 0.03	$+0.13$ -0.06 -0.01	-0.42 $+0.48$ -0.46	-0.44 $+0.48$ -0.46
160.8	LO: 31.19	± 0.05	$+0.21$	$+0.78$	$+0.81$
	NLO: 29.52	± 0.03	$+0.19$ -0.10 $+0.02$	-0.53 $+0.62$ -0.51	-0.57 $+0.63$ -0.51
321.6	LO: 36.96	± 0.05	$+0.16$	$+0.96$	$+0.97$
	NLO: 35.73	± 0.03	$+0.33$ -0.05 -0.05	-0.70 $+0.76$ -0.59	-0.77 $+0.76$ -0.59
643.2	LO: 44.63	± 0.06	$+0.17$	$+1.28$	$+1.29$
	NLO: 43.58	± 0.03	$+0.41$ -0.08 -0.03	-0.96 $+1.05$ -0.78	-1.05 $+1.05$ -0.78
1286.4	LO: 53.66	± 0.07	$+0.31$	$+2.39$	$+2.42$
	NLO: 51.92	± 0.04	$+0.33$ $+0.03$ $+0.02$	-1.28 $+1.99$ -1.45	-1.32 $+1.99$ -1.45

Table 5. The MSTW2008lo68cl A_C table with the breakdown of the different sources of theoretical uncertainty. The MSTW2008lo68cl PDF is used at LO and the MSTW2008nlo68cl one is used at NLO.

M_{W^\pm} (GeV)	A_C^{Fit} (%)	δA_C^{Fit} (%)
20.1	LO: 3.05	± 0.38
	NLO: 1.63	± 0.26
40.2	LO: 7.90	± 0.26
	NLO: 7.39	± 0.21
<u>80.4</u>	LO: 21.89	± 0.27
	NLO: 20.30	± 0.22
160.8	LO: 31.35	± 0.31
	NLO: 29.59	± 0.26
321.6	LO: 37.22	± 0.40
	NLO: 35.99	± 0.34
643.2	LO: 43.49	± 0.57
	NLO: 42.61	± 0.51
1286.4	LO: 54.08	± 0.83
	NLO: 52.53	± 0.74

Table 6. The MSTW2008lo68cl A_C^{Fit} table with δA_C^{Fit} calculated using equation 2.6. The MSTW2008lo68cl PDF is used at LO and the MSTW2008nlo68cl one is used at NLO.

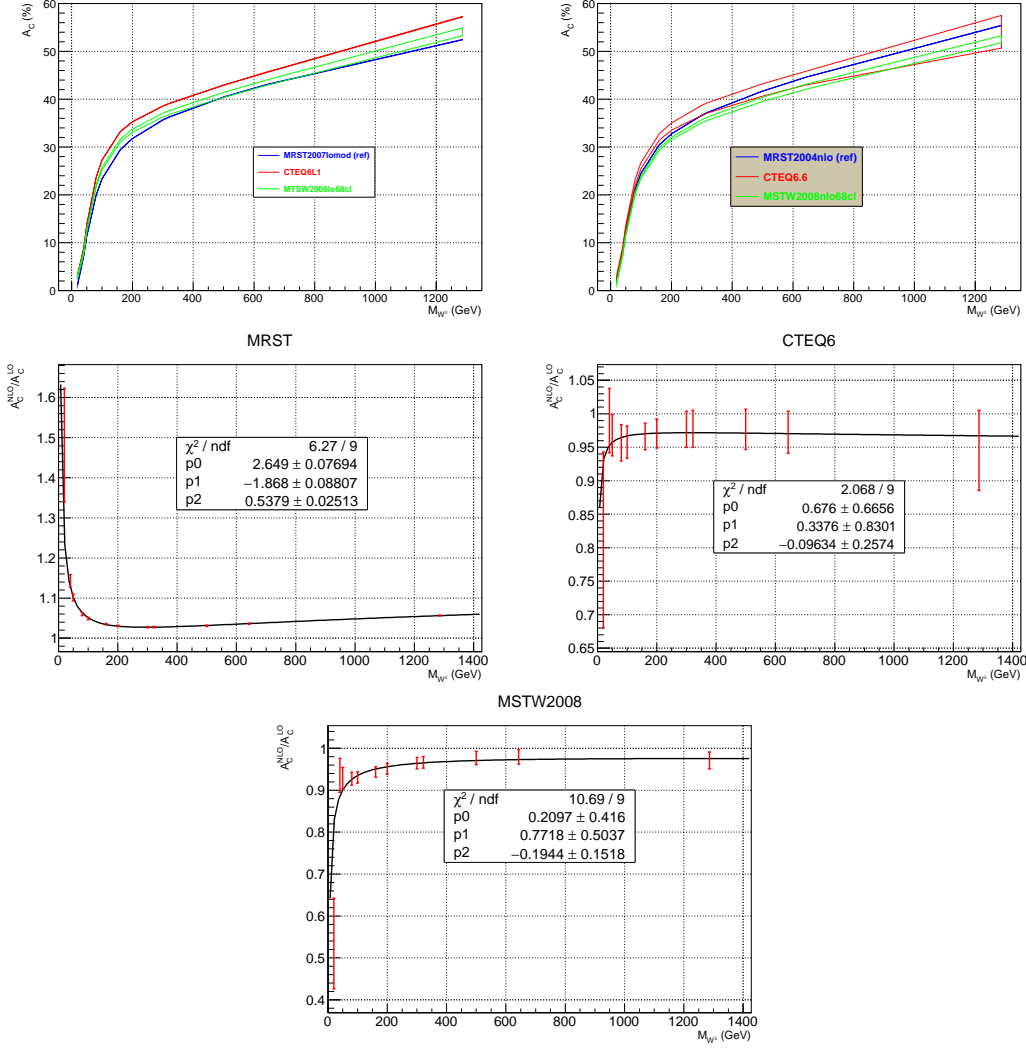


Figure 4. Comparison between the A_C template curves. The top LHS plot compares the LO PDFs: MRST2007lomod (blue, ref. curve), CTEQ6L1 (red), MSTW2008lo68cl (green). The top RHS plot compares the NLO PDFs: MRST2004nlo (blue, ref. curve), CTEQ6.6 (red), MSTW2008nlo68cl (green). The middle and the bottom rows display the $\frac{A_C^{NLO}}{A_C^{LO}}$ fitted by the same functional forms as the A_C^{LO} template curves.

2.2.1 Monte Carlo Generation

To quantify these biases we generate Monte Carlo (MC) event samples using the following LO generator: Herwig++ v2.5.0 [41]. We adopt a tune of the underlying event derived by the ATLAS collaboration [27] and we use accordingly the MRST2007lomod [19] PDF.

Herwig++ mainly uses $2 \rightarrow 2$ LO ME that we denote in the standard way: $1+2 \rightarrow 3+4$. For all the non-resonant processes, the production is splitted into bins of M , where $M = M(3,4)$ is the invariant mass of the two outgoing particles.

For the single vector boson ("V+jets") production, where V stands for W^\pm and γ^*/Z , we mix in the same MC samples the contributions from the pure Drell-Yan process V+0Lp ME and the V+1Lp ME. For all the SM processes a common cut of $M > 10$ GeV is applied.

All the samples are normalized using the Herwig++ cross section multiplied by a K-factor that includes at least the NLO QCD corrections. We'll denote NLO (respectively NNLO) K-factor the ratio: $\frac{\sigma_{NLO}}{\sigma_{LO}}$ (respectively $\frac{\sigma_{NNLO}}{\sigma_{LO}}$). We choose not to apply such higher order corrections to the normalization of the following non-resonant inclusive processes:

- light flavour QCD (denoted QCD LF): $2 \rightarrow 2$ MEs involving $u/d/s/g$ partons
- heavy flavour QCD (denoted QCD HF): $c + \bar{c}$ and $b + \bar{b}$
- prompt photon productions: $\gamma + jets$ and $\gamma + \gamma$

Despite their large cross sections these non-resonant processes will turn out to have very low efficiencies and to represent a small fraction of the remaining background in the event selection used in the analyses we perform.

The NNLO K-factors for the $\gamma^*/Z(\rightarrow \ell^\pm \ell^\mp)$ process are derived from PHOZR [44] with $\mu_R = \mu_F = M(\ell^\pm \ell^\mp)$ and using the MSTW2008nnlo68cl PDF for σ_{NNLO} and the MRST2007lomod one for σ_{LO} .

The top pairs and single top [46][45] NLO K-factors are obtained by running MCFM v5.8 using the MSTW2008nlo68cl and the MSTW2008lo68cl PDFs for the numerator and the denominator respectively, with the QCD scales set as follows: $\mu_R = \mu_F = \hat{s}$.

2.2.2 Fast Simulation of the Detector Response

We use the following setup of Delphes v1.9 [29] to get a fast simulation of the ATLAS detector response as well as a crude emulation of its trigger. The generated MC samples are written in the HepMC v2.04.02 format [30] and passed through Delphes.

For the object reconstruction we also use Delphes defaults, with the exception of utilizing the "anti-kT" jet finder [32] with a cone radius of $\Delta R = \sqrt{(\Delta\eta)^2 + (\Delta\phi)^2} = 0.4$.

2.2.3 Analyses of the $W^\pm \rightarrow \ell^\pm \nu$ Process

We consider only the electron and the muon channels. For these analyses we set the integrated luminosity to $\int \mathcal{L} dt = 1 \text{ fb}^{-1}$.

Instead of trying to derive unreliable systematic uncertainties for these analyses using Delphes, we choose to use realistic values as quoted in actual LHC data analysis publications. We choose the analyses with the largest data samples so as to reduce as much as possible the statistical uncertainties in their measurements but also to benefit from the largest statistics for the data samples utilized to derive their systematic uncertainties. This choice leads us to quote systematic uncertainties from analyses performed by the CMS collaboration. Namely we use:

$$\delta_{Syst} A_C(W^\pm \rightarrow e^\pm \nu_e) = 1.0\% \quad (2.7)$$

$$\delta_{Syst} A_C(W^\pm \rightarrow \mu^\pm \nu_\mu) = 0.4\% \quad (2.8)$$

The values quoted in equations 2.7 and 2.8 come from references [4] and [5], respectively. And to get an estimate of the uncertainty on a ratio of number of expected events we use the systematics related to the measurement of the following cross sections ratio

$$\sigma(pp \rightarrow W^\pm \rightarrow \ell^\pm \nu_\ell) / \sigma(pp \rightarrow \gamma^* / Z \rightarrow \ell^\pm \ell^\mp) \quad (2.9)$$

which amounts to 1.0% [48].

2.2.4. a. The Electron Channel

2.2.4. a.1. Event Selection in the Electron Channel

The following cuts are applied:

- $p_T(e^\pm) > 25 \text{ GeV}$
- $|\eta(e^\pm)| < 1.37$ or $1.53 < |\eta(e^\pm)| < 2.4$
- Tracker Isolation: reject events with additional tracks of $p_T > 2 \text{ GeV}$ within a cone of $\Delta R = 0.5$ around the direction of the e^\pm track
- Calorimeter Isolation: the ratio of, the scalar sum of E_T deposits in the calorimeter within a cone of $\Delta R = 0.5$ around the direction of the e^\pm , to the $p_T(e^\pm)$, must be less than 1.2
- $\cancel{E}_T > 25 \text{ GeV}$
- $M_T = \sqrt{2p_T(\ell^\pm)\cancel{E}_T[1 - \cos\Delta\phi(\ell^\pm, \cancel{E}_T)]} > 40 \text{ GeV}$
- Reject events with an additional leading isolated muon: μ_1^\pm
- Reject events with an additional trailing isolated electron: e_2^\pm
- Reject events with an additional second track ($Track_2$) such that:

$$\begin{cases} Q(e_1^\pm) = -Q(Track_2) \\ 3 < p_T(Track_2) < 10 \text{ GeV} \\ M[e_1^\pm, Track_2] > 50 \text{ GeV} \end{cases}$$

The corresponding selection efficiencies and event yields (expressed in thousandths of events) are reported in table 7. Figure 5 displays the \cancel{E}_T distribution after the event selection in the electron channel (LHS) and in the muon channel (RHS).

The non-resonant background processes represent just $\sim 4\%$ of the total background after the event selection, this justifies the approximation of not to include the NLO QCD corrections to their normalizations.

<i>Process</i>	ϵ (%)	N_{exp} (k evts)	$A_C \pm \delta A_C^{Stat}$ (%)
Signal: $W^\pm \rightarrow e^\pm \nu_e$			
$M(W^\pm) = 40.2$ GeV	0.81 ± 0.01	290.367	9.66 ± 1.57
$M(W^\pm) = 60.3$ GeV	13.69 ± 0.05	2561.508	11.22 ± 0.38
$M(W^\pm) = \underline{80.4}$ GeV	29.59 ± 0.04	3343.195	16.70 ± 0.18
$M(W^\pm) = 100.5$ GeV	39.19 ± 0.07	2926.093	20.77 ± 0.22
$M(W^\pm) = 120.6$ GeV	44.84 ± 0.07	2357.557	23.19 ± 0.21
$M(W^\pm) = 140.7$ GeV	48.66 ± 0.07	1899.820	25.29 ± 0.20
$M(W^\pm) = 160.8$ GeV	51.28 ± 0.07	1527.360	26.87 ± 0.19
$M(W^\pm) = 201.0$ GeV	54.54 ± 0.07	1.032	29.06 ± 0.18
Background	-	91.614 ± 1.706	10.07 ± 0.15
$W^\pm \rightarrow \mu^\pm \nu_\mu / \tau^\pm \nu_\tau / q\bar{q}l$	0.211 ± 0.003	71.350	12.92 ± 1.25
$t\bar{t}$	5.76 ± 0.02	6.600	1.00 ± 0.37
$t + b, t + q(+b)$	3.59 ± 0.01	1.926	28.97 ± 0.35
$W + W, W + \gamma^*/Z, \gamma^*/Z + \gamma^*/Z$	2.94 ± 0.01	2.331	10.65 ± 0.35
$\gamma + \gamma, \gamma + jets, \gamma + W^\pm, \gamma + Z$	0.201 ± 0.001	0.759	17.25 ± 0.53
γ^*/Z	0.535 ± 0.001	5.746	4.43 ± 0.23
QCD HF	$(0.44 \pm 0.17) \times 10^{-4}$	1.347	14.29 ± 37.41
QCD LF	$(0.87 \pm 0.33) \times 10^{-4}$	1.555	71.43 ± 26.45

Table 7. Selection efficiencies, event yields and integral charge asymmetries for the $W^\pm \rightarrow e^\pm \nu_e$ analysis.

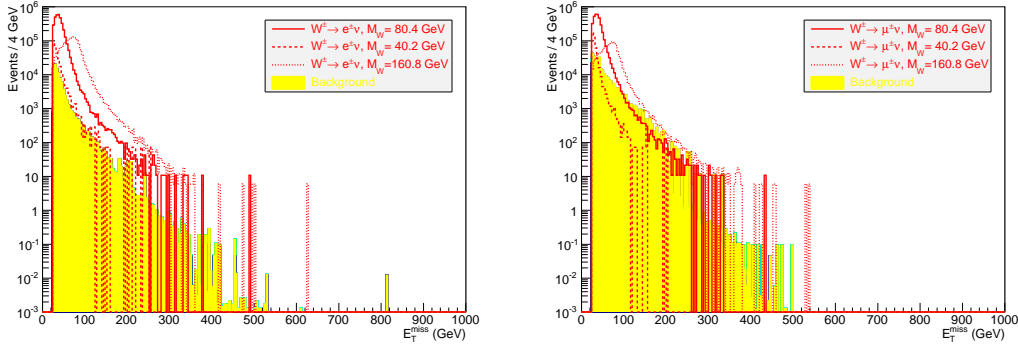


Figure 5. E_T^{miss} distribution after the event selection is applied for the $W^\pm \rightarrow e^\pm \nu_e$ (LHS) and for the $W^\pm \rightarrow \mu^\pm \nu_\mu$ (RHS) analysis.

2.2.4. a.2. Common Procedure for the Background Subtraction and the Propagation of the Experimental Uncertainty

If we were to apply such an analysis on real collider data, we would get in the end the measured integral charge asymmetry A_C^{Meas} of the data sample passing the selection cuts. And obviously we wouldn't know which event come from which sub-process. Since the MC enables to separate the different contributing sub-processes, it's possible to extract the

integral charge asymmetry of the signal (S), knowing that of the total background (B). If we denote $\alpha^{Exp} = \frac{N_B^{Exp}}{N_S^{Exp}}$ the ratio of the expected number of background events to the expected number of signal events, we can express $A_C^{Exp}(S+B)$, the integral charge asymmetry of all remaining events either from signal or from background, with respect to that quantity for signal only events $A_C^{Exp}(S)$, and for background only events $A_C^{Exp}(B)$. This writes:

$$A_C^{Exp}(S+B) = \frac{A_C^{Exp}(S) + \alpha^{Exp} \cdot A_C^{Exp}(B)}{1 + \alpha^{Exp}} \quad (2.10)$$

where the upper script "Exp" stands for "Expected".

This formula can easily be inverted to extract $A_C^{Exp}(S)$ in what we'll refer to as the "background subtraction equation":

$$A_C^{Exp}(S) = (1 + \alpha^{Exp}) \cdot A_C^{Exp}(S+B) - \alpha^{Exp} \cdot A_C^{Exp}(B) \quad (2.11)$$

Note that these expressions involve only ratios hence their experimental systematic uncertainty remains relatively small. The uncertainty on $A_C^{Exp}(S)$ is calculated by taking account the correlation between the uncertainties of α^{Exp} , $A_C^{Exp}(B)$, and $A_C^{Exp}(S+B)$.

$$\begin{aligned} [\delta A_C(S)]^2 &= [A_C(S+B) - A_C(B)]^2 \cdot [\delta \alpha]^2 + (1 + \alpha)^2 \cdot [\delta A_C(S+B)]^2 + \alpha^2 \cdot [\delta A_C(B)]^2 \\ &\quad + 2 \cdot [A_C(S+B) - A_C(B)] \cdot (1 + \alpha) \cdot COV[\alpha, A_C(S+B)] \\ &\quad - 2 \cdot [A_C(S+B) - A_C(B)] \cdot \alpha \cdot COV[\alpha, A_C(B)] \\ &\quad - 2 \cdot \alpha \cdot (1 + \alpha) \cdot COV[A_C(B), A_C(S+B)] \end{aligned} \quad (2.12)$$

In order to propagate the experimental uncertainties from equations 2.7, 2.8, and 2.9 to $\delta A_C(S)$, we perform pseudo-experiments running 10,000,000 trials for each. In these trials all quantities involved in the background subtraction equation 2.11 is allowed to fluctuate according to a gaussian smearing that has its central value as a mean and its total uncertainty as an RMS. In each of these pseudo-experiments, the signal S and the background B float separately. For each of the events categories (S or B) separately, the numbers of positively and negatively charged events also fluctuate but in full anti-correlation. This procedure enables to estimate numerically the values of the variances and covariances appearing in equation 2.12.

In a realistic analysis context, $A_C^{Exp}(S)$ can be obtained from a full simulation of the signal, $A_C^{Exp}(B)$ and α^{Exp} can also be obtained this way or through data-driven techniques. The experimental systematic uncertainties can be propagated as usually done to each of these quantities. And one can extract $A_C^{Obs}(S)$ from a data sample using the following form of equation 2.11:

$$A_C^{Obs}(S) = (1 + \alpha^{Meas}) \cdot A_C(Data) - \alpha^{Meas} \cdot A_C^{Meas}(B) \quad (2.13)$$

provided a good estimate of the number of remaining signal and background events after the event selection as well as the integral charge asymmetries of the signal and of the background are established. The upper script "Obs" stands for observed.

2.2.4. a.3. The Measured A_C in the Electron Channel

For the nominal W mass, we calculate $A_C^{Meas}(S)$ using the inputs from the analysis in the electron channel only with their statistical uncertainties:

- $A_C^{Exp}(S) = (16.70 \pm 0.18)\%$
- $A_C^{Exp}(B) = (10.07 \pm 0.15)\%$
- $A_C^{Exp}(S + B) = (16.52 \pm 0.11)\%$
- $\alpha^{Exp} = (2.74 \pm 0.05) \times 10^{-2}$

After the background subtraction and the propagation of the experimental systematic uncertainties, we get:

$$A_C^{Meas}(S) = (16.70 \pm 0.76)\% \quad (2.14)$$

2.2.4. a.4. The A_C Template Curve in the Electron Channel

In order to establish the experimental A_C template curve, we apply a "multitag and probe method". We consider all the $W^\pm \rightarrow e^\pm \nu_e$ MC samples with a non-nominal W mass as the multitag and the one with the nominal W mass as the probe. We apply equation 2.11 to each of the multitag samples and plot their $A_C^{Meas}(S)$ as a function of M_{W^\pm} . A second degree polynomial of logarithms of logarithms is well suited to fit the template curve as shown in the LHS of figure 6, for the electron channel. The fit to this template curve can be expressed by equation 2.15. Note that we do not include the probe sample in the template curve since we want to estimate the accuracy of its indirect mass measurement.

$$A_C^{Meas}(W^\pm \rightarrow e^\pm + \nu_e) = -107.1 - 183.5 \times \text{Log}(\text{Log}(M_{W^\pm})) + 82.69 \times \text{Log}(\text{Log}(M_{W^\pm}))^2 \quad (2.15)$$

<i>Process</i>	$\alpha^{Exp} \pm \delta\alpha^{Stat}$	Z_N (σ)	$A_C^{Meas.}$ (%)	$\delta A_C^{Meas.}$ (%)	$\delta A_C^{Meas.Fit}$ (%)
Signal: $W^\pm \rightarrow e^\pm \nu_e$					
$M(W^\pm) = 40.2$ GeV	$(31.55 \pm 0.77) \times 10^{-2}$	37.25	9.66	1.05	0.60
$M(W^\pm) = 60.3$ GeV	$(3.58 \pm 0.07) \times 10^{-2}$	$>> 5.00$	11.22	0.78	0.52
$M(W^\pm) = \underline{80.4}$ GeV	$(2.74 \pm 0.05) \times 10^{-2}$	$>> 5.00$	16.70	0.76	0.35
$M(W^\pm) = 100.5$ GeV	$(3.13 \pm 0.06) \times 10^{-2}$	$>> 5.00$	20.77	0.77	0.33
$M(W^\pm) = 120.6$ GeV	$(3.89 \pm 0.07) \times 10^{-2}$	$>> 5.00$	23.19	0.78	0.35
$M(W^\pm) = 140.7$ GeV	$(4.82 \pm 0.09) \times 10^{-2}$	$>> 5.00$	25.29	0.78	0.39
$M(W^\pm) = 160.8$ GeV	$(6.00 \pm 0.11) \times 10^{-2}$	$>> 5.00$	26.86	0.79	0.42
$M(W^\pm) = 201.0$ GeV	$(88.77 \pm 1.66) \times 10^0$	0.19	29.07	2.03	0.48

Table 8. Noise to signal ratio, signal statistical significance, and expected and measured integral charge asymmetries for the signal after the event selection in the electron channel.

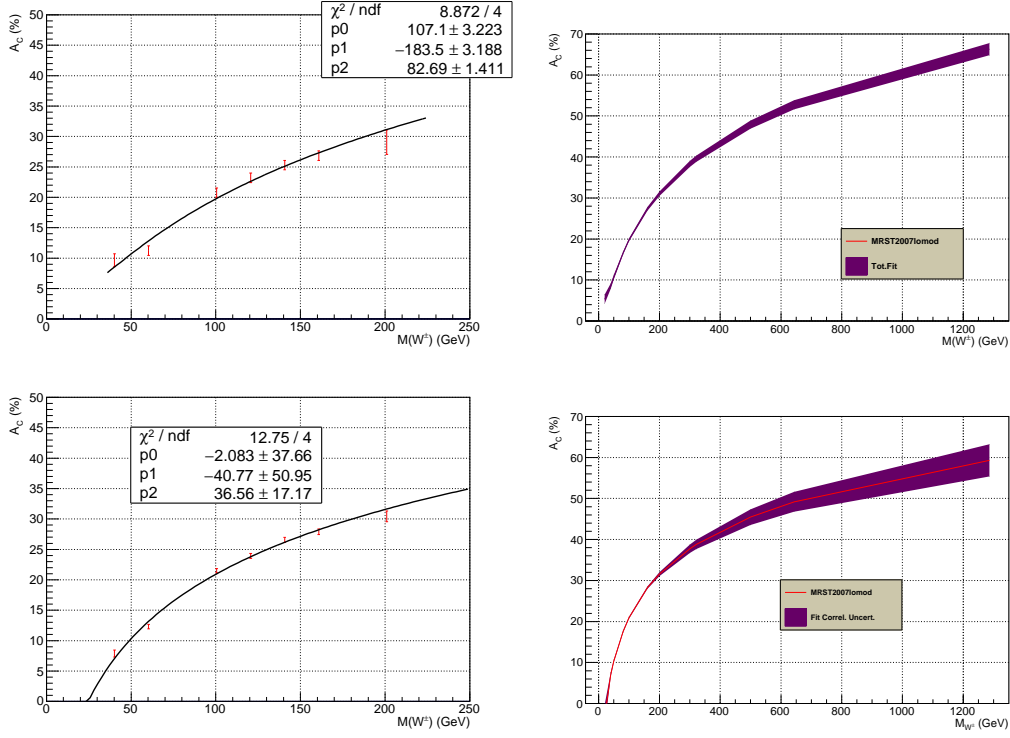


Figure 6. The A_C^{Meas} template curves for the electron channel (top) and the muon channel (bottom). The fits to the $A_C^{Meas}(S)$ are presented on the LHS. These fits with uncertainty bands accounting for the correlation between the uncertainties of the fit parameters are shown on the RHS.

The values of the noise to signal ratio (α^{Exp}), the signal statistical significance (Z_N , defined in the next paragraph), the expected (A_C^{Exp}), and the measured (A_C^{Meas}) integral charge asymmetries for the signal after the event selection in the electron channel are reported in table 8.

The signal significances reported are calculated using a conversion of the confidence level of the signal plus background hypothesis CL_{S+B} into an equivalent number of one-sided gaussian standard deviations Z_N as proposed in [52] and implemented in RooStats [53]. For these calculations the systematic uncertainty of the background was set to 5%, which completely covers the total uncertainty for the measurement of the inclusive cross section $\sigma(p + p \rightarrow W^\pm \rightarrow \ell^\pm \nu)$ as reported in [48].

We recalculate the uncertainty on $A_C^{Meas}(S)$ accounting for the correlation between the parameters when fitting the $A_C^{Meas}(S)$ template curve by applying equation 2.12. This results in a slightly reduced uncertainty as shown in equation 2.16.

$$A_C^{Meas.Fit}(S) = (16.70 \pm 0.35)\% \quad (2.16)$$

2.2.4. b. The Muon Channel

2.2.4. b.1. Event Selection in the Muon Channel

The following cuts are applied:

- $p_T(\mu) > 20 \text{ GeV}$
- $|\eta(\mu)| < 2.4$
- Tracker Isolation: reject events with additional tracks of $p_T > 2 \text{ GeV}$ within a cone of $\Delta R = 0.5$ around the direction of the μ^\pm track
- Calorimeter Isolation: the ratio of, the scalar sum of E_T deposits in the calorimeter within a cone of $\Delta R = 0.5$ around the direction of the μ^\pm , to the $p_T(\mu^\pm)$ must be less than 0.25
- $E_T > 25 \text{ GeV}$
- $M_T > 40 \text{ GeV}$
- Reject events with an additional trailing isolated muon: μ_2^\pm
- Reject events with an additional leading isolated electron: e_1^\pm
- Reject events with an additional second track ($Track_2$) such that :

$$\begin{cases} Q(\mu_1^\pm) = -Q(Track_2) \\ 3 < p_T(Track_2) < 10 \text{ GeV} \\ M[\mu_1^\pm, Track_2] > 50 \text{ GeV} \end{cases}$$

The corresponding selection efficiencies and event yields are reported in table 9. The RHS of figure 5 displays the E_T distribution after the event selection. The non-resonant background processes represent $\sim 3\%$ of the total background after the event selection.

2.2.4. b.2. The Measured A_C in the Muon Channel

The $A_C^{Meas}(S)$ treatment described in paragraph 2.2.4. a.2. is applied to the probe sample in the muon channel, starting from the following inputs:

- $A_C^{Exp}(S) = (17.42 \pm 0.18)\%$
- $A_C^{Exp}(B) = (7.36 \pm 0.15)\%$
- $A_C^{Exp}(S + B) = (16.64 \pm 0.12)\%$
- $\alpha^{Exp} = (8.38 \pm 0.65) \times 10^{-2}$

<i>Process</i>	ϵ (%)	N_{exp} (k evts)	$A_C(S) \pm \delta A_C^{Stat}(S)$ (%)
Signal: $W^\pm \rightarrow \mu^\pm \nu_\mu$			
$M(W^\pm) = 40.2$ GeV	1.22 ± 0.02	439.192	7.86 ± 1.28
$M(W^\pm) = 60.3$ GeV	12.27 ± 0.05	2295.224	12.30 ± 0.40
$M(W^\pm) = \underline{80.4}$ GeV	29.32 ± 0.04	3313.642	17.42 ± 0.18
$M(W^\pm) = 100.5$ GeV	54.03 ± 0.07	4034.779	21.48 ± 0.19
$M(W^\pm) = 120.6$ GeV	31.30 ± 0.07	1645.675	23.93 ± 0.25
$M(W^\pm) = 140.7$ GeV	33.71 ± 0.07	1316.121	26.56 ± 0.23
$M(W^\pm) = 160.8$ GeV	35.37 ± 0.07	1053.514	27.90 ± 0.23
$M(W^\pm) = 201.0$ GeV	82.84 ± 0.05	1.568	30.44 ± 0.15
Background	-	277.787 ± 21.555	7.36 ± 0.15
$W^\pm \rightarrow e^\pm \nu_e / \tau^\pm \nu_\tau / q\bar{q}l$	0.291 ± 0.003	177.500	8.70 ± 1.07
$t\bar{t}$	4.27 ± 0.02	4.895	-0.14 ± 0.43
$t + b, t + q(+b)$	0.485 ± 0.005	0.264	27.14 ± 0.96
$W + W, W + \gamma^*/Z, \gamma^*/Z + \gamma^*/Z$	3.25 ± 0.01	2.478	11.39 ± 0.33
$\gamma + \gamma, \gamma + jets, \gamma + W^\pm, \gamma + Z$	0.135 ± 0.001	0.497	17.48 ± 0.65
γ^*/Z	0.727 ± 0.001	43.382	5.79 ± 0.20
QCD HF	$(2.13 \pm 0.37) \times 10^{-4}$	17.983	-17.65 ± 16.88
QCD LF	$(1.38 \pm 0.41) \times 10^{-4}$	30.788	9.09 ± 30.03

Table 9. Event selection efficiencies, event yields and integral charge asymmetries for the $W^\pm \rightarrow \mu^\pm \nu_\mu$ analysis.

For the nominal W mass, this leads to a measured integral charge asymmetry of:

$$A_C^{Meas}(S) = (17.42 \pm 0.34)\% \quad (2.17)$$

where the uncertainty is also dominated by the value in equation 2.8.

2.2.4. b.3. The Template Curve in the Muon Channel

After applying the $A_C^{Meas}(S)$ treatment to the tag samples in the muon channel, we get the $A_C^{Meas}(S)$ template curve shown in the RHS of figure 6. The fit to this template curve is reported in equation 2.18.

$$A_C^{Meas}(W^\pm \rightarrow \mu^\pm \nu_\mu) = -2.08 - 40.77 \times \text{Log}(\text{Log}(M_{W^\pm})) + 36.56 \times \text{Log}(\text{Log}(M_{W^\pm}))^2 \quad (2.18)$$

The values of the noise to signal ratio (α^{Exp}), the signal statistical significance (Z_N), and the expected (A_C^{Exp}) and the measured (A_C^{Meas}) integral charge asymmetries for the signal after the event selection in the muon channel are reported in table 10.

Again, accounting for the correlation between the parameters when fitting the $A_C^{Meas}(S)$ template curve enables to reduce the uncertainty as shown in equation 2.19.

$$A_C^{Meas.Fit}(S) = (17.42 \pm 0.27)\% \quad (2.19)$$

<i>Process</i>	$\alpha^{Exp} \pm \delta\alpha^{Stat}$	Z_N (σ)	$A_C^{Meas.}$ (%)	$\delta A_C^{Meas.}$ (%)	$\delta A_C^{Meas.Fit}$ (%)
Signal: $W^\pm \rightarrow \mu^\pm \nu_\mu$					
$M(W^\pm) = 40.2$ GeV	$(63.25 \pm 4.97) \times 10^{-2}$	11.19	7.86	0.59	0.45
$M(W^\pm) = 60.3$ GeV	$(12.10 \pm 0.94) \times 10^{-2}$	2295.22	12.30	0.37	0.27
$M(W^\pm) = \underline{80.4}$ GeV	$(8.38 \pm 0.65) \times 10^{-2}$	3313.64	17.42	0.34	0.27
$M(W^\pm) = 100.5$ GeV	$(6.88 \pm 0.53) \times 10^{-2}$	4034.78	21.48	0.35	0.22
$M(W^\pm) = 120.6$ GeV	$(16.88 \pm 1.31) \times 10^{-2}$	1645.68	23.93	0.40	0.19
$M(W^\pm) = 140.7$ GeV	$(21.11 \pm 1.64) \times 10^{-2}$	1316.12	26.56	0.42	0.22
$M(W^\pm) = 160.8$ GeV	$(26.37 \pm 2.05) \times 10^{-2}$	1053.51	27.90	0.45	0.27
$M(W^\pm) = 201.0$ GeV	$(17.72 \pm 1.37) \times 10^{-1}$	1.57	30.44	0.87	0.40

Table 10. Noise to signal ratio, signal statistical significance, and expected and measured integral charge asymmetries for the signal after the event selection in the muon channel.

2.3 Indirect Determination of M_{W^\pm}

2.3.1 Results in the Individual Channels

The $A_C^{Meas}(S) \pm \delta A_C^{Meas.Fit}(S)$ in the electron and in the muon channels translate into indirect $M_{W^\pm}^{Meas.Fit} \pm \delta M_{W^\pm}$ measurements using the experimental A_C template curves from the RHS of figure 6 in each of these channels:

$$A_C^{Meas.Fit}(S) = (16.70 \pm 0.35)\% \Rightarrow M^{Meas.Fit}(W^\pm \rightarrow e^\pm \nu_e) = 81.07_{-2.01}^{+2.06} \text{ GeV}, \quad (2.20)$$

$$A_C^{Meas.Fit}(S) = (17.42 \pm 0.27)\% \Rightarrow M^{Meas.Fit}(W^\pm \rightarrow \mu^\pm \nu_\mu) = 79.67_{-1.39}^{+3.56} \text{ GeV}. \quad (2.21)$$

2.3.2 Combination of the Electron and the Muon Channels

We combine the electron and muon channels using a weighted mean for the measured W^\pm mass, the weight is the inverse of the uncertainty on the measured mass. In order to account for the asymmetric uncertainties, we slightly modify the expressions for the weighted mean and the weighted RMS of a quantity x as follows:

$$\langle x \rangle = \frac{\sum_{i=1}^N \frac{x_i}{\delta_i^2}}{\sum_{i=1}^N \frac{1}{\delta_i^2}} \rightarrow \langle x \rangle = \frac{\sum_{i=1}^N \left[\frac{x_i}{(\delta_i^{Up})^2} + \frac{x_i}{(\delta_i^{Down})^2} \right]}{\sum_{i=1}^N \left[\frac{1}{(\delta_i^{Up})^2} + \frac{1}{(\delta_i^{Down})^2} \right]} \quad (2.22)$$

$$\delta^2(\langle x \rangle) = \frac{1}{\sum_{i=1}^N \frac{x_i}{\delta_i^2}} \rightarrow \delta^2(\langle x \rangle) = \frac{1}{\sum_{i=1}^N \left[\frac{x_i}{(\delta_i^{Up})^2} + \frac{x_i}{(\delta_i^{Down})^2} \right]} \quad (2.23)$$

where x_i , δ_i^{Up} and δ_i^{Down} are respectively the central value, the upward uncertainty and the downward uncertainty of the mass derived in the channel i .

The result of the combination is:

$$M^{Comb.Meas.}(W^\pm) = 80.30 \pm 0.96 \text{ GeV [Expt. Comb.]} \quad (2.24)$$

2.4 Final Result for MRST2007lomod

The next step is to estimate the theoretical uncertainty corresponding to the measured mass and to combine it with the experimental uncertainty. We simply use the central value of the measured W^\pm mass and we read-off the theoretical template curve the intervals, defined by the intercepts with upper and lower fit curves.

$$M_{Theory}(W^\pm) = 80.30_{-0.21}^{+0.19} \text{ GeV [MRST2007lomod]} \quad (2.25)$$

Finally we just sum in quadrature the theoretical and experimental upward and downward uncertainties:

$$\delta_{Tot.} M(W^\pm) = 80.30 \begin{cases} +\sqrt{(0.96)^2 + (0.19)^2} = +0.98 \\ -\sqrt{(0.96)^2 + (0.21)^2} = -0.98 \end{cases} \text{ GeV} \quad (2.26)$$

Therefore the final result for the MRST2007lomod PDF reads:

$$M_{W^\pm} = 80.30_{-0.98}^{+0.98} \text{ GeV [Total MRST2007lomod]}. \quad (2.27)$$

This constitutes an indirect M_{W^\pm} measurement with a relative accuracy of 1.2%, where the experimental uncertainty largely dominates over the (underestimated) theoretical uncertainty.

2.5 Final Results for the Other Parton Density Functions

Since Delphes v1.9 does not store the set of variables $(x_1, x_2, flav_1, flav_2, Q^2)$ necessary to access the PDF information from the generator, we slightly modify it so as to retrieve the "HepMC::PdfInfo" object from the HepMC event record and to store it within the Delphes GEN branch as described in [49].

Based upon these variables we can apply PDF re-weightings so as to make experimental A_C predictions for the CTEQ6L1 and the MSTW2008lo68cl PDFs. The new event weight is calculated in the standard way:

$$\text{PDFweight(New PDF)} = \frac{f_{\text{Flav}_1}^{\text{New PDF}}(x_1, Q^2)}{f_{\text{Flav}_1}^{\text{Old PDF}}(x_1, Q^2)} \times \frac{f_{\text{Flav}_2}^{\text{New PDF}}(x_2, Q^2)}{f_{\text{Flav}_2}^{\text{Old PDF}}(x_2, Q^2)} \quad (2.28)$$

where the "Old PDF" is the default one, MRST2007lomod, and the "New PDF" is either CTEQ6L1 or MSTW2008lo68cl.

We re-run the electron and muon channel analyses and just change the weights of all the selected events. This results in signal event yields, and $A_C^{Exp}(S)$, $A_C^{Exp}(B)$ as reported in tables 11 and 12 for the CTEQ6L1 PDF and in tables 13 and 14 for the MSTW2008lo68cl one.

Then we produce the experimental A_C template curves for CTEQ6L1 and MSTW2008lo68cl and both analysis channels as displayed in figures 7 and 8.

For the CTEQ6L1 PDF, we find:

$$A_C^{Meas.Fit}(S) = (15.78 \pm 0.50)\% \Rightarrow M^{Meas}(W^\pm \rightarrow e^\pm \nu_e) = 73.39_{-2.30}^{+2.40} \text{ GeV}, \quad (2.29)$$

M_{W^\pm} (GeV)	$N_{Exp}(S)$ (k Evts)	$A_C^{Exp}(S)$ (%)
40.2 e^\pm	288.688 \pm 5.866	11.26 \pm 2.06
μ^\pm	947.643 \pm 11.535	7.86 \pm 1.28
60.3 e^\pm	2491.955 \pm 10.746	10.65 \pm 0.49
μ^\pm	5285.294 \pm 16.847	12.30 \pm 0.40
80.4 e^\pm	3766.569 \pm 8.423	15.78 \pm 0.29
μ^\pm	5551.710 \pm 6.752	17.42 \pm 0.18
100.5 e^\pm	4106.984 \pm 5.009	20.64 \pm 0.19
μ^\pm	4188.292 \pm 4.997	21.48 \pm 0.19
120.6 e^\pm	2739.825 \pm 4.796	23.54 \pm 0.26
μ^\pm	3777.497 \pm 4.730	23.93 \pm 0.25
140.7 e^\pm	2284.590 \pm 3.512	25.52 \pm 0.25
μ^\pm	3020.544 \pm 3.268	26.56 \pm 0.23
160.8 e^\pm	1584.146 \pm 2.512	27.07 \pm 0.24
μ^\pm	2461.819 \pm 2.255	27.90 \pm 0.23
201.0 e^\pm	1.259 \pm 0.002	29.57 \pm 0.23
μ^\pm	1.628 \pm 0.001	30.64 \pm 0.15

Table 11. Number of expected signal events and expected signal A_C as a function of $M(W^\pm)$ for the electron and muon analyses reweighted to the CTEQ6L1 PDF predictions.

W^\pm Decay Channel	$N_{Exp}(B)$ (k Evts)	$A_C^{Exp}(B)$ (%)
e^\pm	352.660 \pm 7.996	9.74 \pm 0.23
μ^\pm	707.617 \pm 29.944	7.45 \pm 0.15

Table 12. Number of expected background events and expected background A_C for the electron (upper line) and the muon (lower line) analyses reweighted to the CTEQ6L1 PDF predictions.

$$A_C^{Meas.Fit}(S) = (17.42 \pm 0.18)\% \Rightarrow M^{Meas}(W^\pm \rightarrow \mu^\pm \nu_\mu) = 79.82^{+0.94}_{-0.92} \text{ GeV} \quad (2.30)$$

which leads to the following combined value:

$$M^{Comb.Meas.}(W^\pm \rightarrow \ell^\pm \nu_\ell) = (78.95 \pm 0.61) \text{ GeV [Expt. CTEQ6L1]} \quad (2.31)$$

To this measured central value of the mass correspond the following theoretical uncertainties:

$$M(W^\pm) = 78.95^{+0.11}_{-0.13} \text{ GeV [Theory CTEQ6L1]}, \quad (2.32)$$

Therefore the final result for the CTEQ6L1 PDF reads:

$$M(W^\pm) = 78.95^{+0.62}_{-0.62} \text{ GeV [Total CTEQ6L1]} \quad (2.33)$$

and it's dominant uncertainty is also experimental, since its theoretical uncertainty is underestimated. This represents an indirect measurement of the W^\pm mass with a relative accuracy of 0.8%.

For the MSTW2008lo68cl PDF:

$$A_C^{Meas.Fit}(S) = (15.78 \pm 0.52)\% \Rightarrow M^{Meas}(W^\pm \rightarrow e^\pm \nu_e) = 76.91^{+2.80}_{-2.74} \text{ GeV}, \quad (2.34)$$

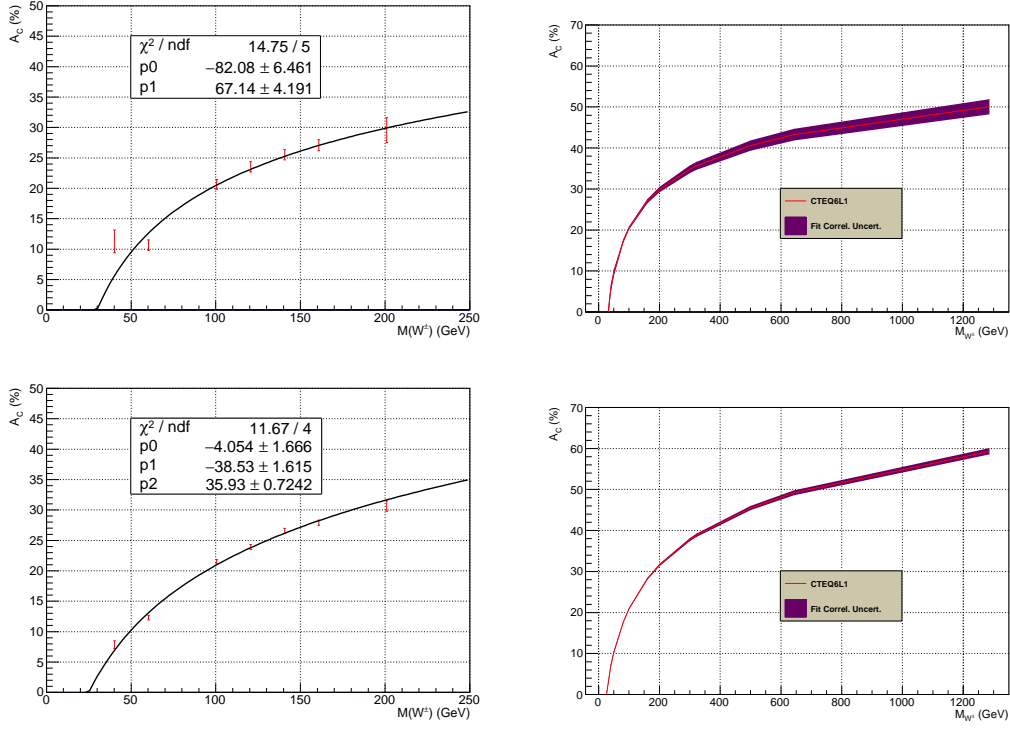


Figure 7. The CTEQ6L1 A_C template curves for the $W^\pm \rightarrow e^\pm \nu_e$ (top) and the $W^\pm \rightarrow \mu^\pm \nu_\mu$ (bottom) analyses. The fits to the $A_C^{Exp}(S)$ are presented on the LHS. These fits with uncertainty bands accounting for the correlation between the uncertainties of the fit parameters are shown on the RHS.

M_{W^\pm} (GeV)	$N_{Exp}(S)$ (k Evts)	$A_C^{Exp}(S)$ (%)
40.2 e^\pm	280.257 ± 5.781	11.26 ± 2.06
40.2 μ^\pm	913.868 ± 11.334	7.86 ± 1.28
60.3 e^\pm	2469.515 ± 10.705	10.65 ± 0.49
60.3 μ^\pm	5219.408 ± 16.783	12.30 ± 0.40
80.4 e^\pm	3663.615 ± 8.363	15.78 ± 0.29
80.4 μ^\pm	5711.468 ± 6.753	17.42 ± 0.18
100.5 e^\pm	4053.288 ± 5.016	20.64 ± 0.19
100.5 μ^\pm	4165.175 ± 5.000	21.48 ± 0.19
120.6 e^\pm	2665.994 ± 4.800	23.54 ± 0.26
120.6 μ^\pm	3811.380 ± 4.697	23.93 ± 0.25
140.7 e^\pm	2221.101 ± 3.530	25.52 ± 0.25
140.7 μ^\pm	3033.091 ± 3.252	26.56 ± 0.23
160.8 e^\pm	1539.501 ± 2.516	27.07 ± 0.24
160.8 μ^\pm	2446.996 ± 2.280	27.90 ± 0.23
201.0 e^\pm	1.230 ± 0.002	29.57 ± 0.23
201.0 μ^\pm	1.645 ± 0.001	30.64 ± 0.15

Table 13. Number of expected signal events and expected signal A_C as a function of $M(W^\pm)$ for the electron and muon analyses reweighted to the MSTW2008lo68cl PDF predictions.

$$A_C^{Meas.Fit}(S) = (17.42 \pm 0.18)\% \Rightarrow M^{Meas}(W^\pm \rightarrow \mu^\pm \nu_\mu) = 82.07^{+1.11}_{-1.10} \text{ GeV} \quad (2.35)$$

which leads to the following combined value:

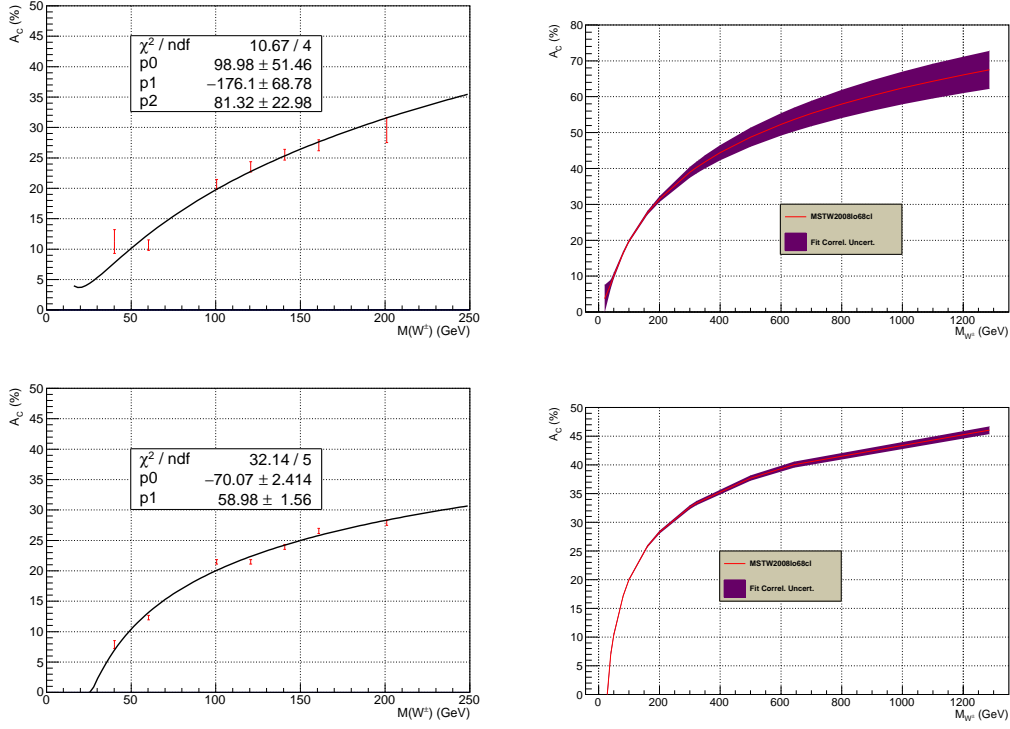


Figure 8. The MSTW2008lo68cl A_C template curves for the $W^\pm \rightarrow e^\pm \nu_e$ (top) and the $W^\pm \rightarrow \mu^\pm \nu_\mu$ (bottom) analyses. The fits to the $A_C^{Exp}(S)$ are presented on the LHS. These fits with uncertainty bands accounting for the correlation between the uncertainties of the fit parameters are shown on the RHS.

W^\pm Decay Channel	$N_{Exp}(B)$ (k Evts)	$A_C^{Exp}(B)$ (%)
e^\pm	371.956 ± 8.081	9.74 ± 0.23
μ^\pm	721.196 ± 29.968	7.45 ± 0.15

Table 14. Number of expected background events and expected background A_C for the electron (upper line) and muon (lower line) analyses reweighted to the MSTW2008lo68cl PDF predictions.

$$M^{Comb.Meas.}(W^\pm \rightarrow \ell^\pm \nu_\ell) = (81.36 \pm 0.73) \text{ GeV} \quad (2.36)$$

The corresponding theoretical uncertainties are:

$$M(W^\pm) = 81.36^{+1.50}_{-1.32} \text{ GeV [Theory MSTW2008lo68cl]}, \quad (2.37)$$

Therefore the final result for the MSTW2008lo68cl PDF reads:

$$M(W^\pm) = 81.36^{+1.67}_{-1.51} \text{ GeV [Total MSTW2008lo68cl]} \quad (2.38)$$

and it's dominant uncertainty comes from $\delta_{PDF}^{Theory} A_C$. In this case, this represents an indirect measurement of the W^\pm mass with a relative accuracy of 2.1%.

2.6 Summary of the M_{W^\pm} Measurements and their Accuracy

We sum up the indirect mass measurements of M_{W^\pm} extracted from the integral charge asymmetry of the $W^\pm \rightarrow \ell^\pm \nu$ inclusive process within table 15. Therein we also present a few figures of merit of the accuracy of these measurements:

1. $\frac{\delta M_{W^\pm}^{Fit}}{M_{W^\pm}^{Fit}}$
2. $\frac{(M_{W^\pm}^{Fit} - M_{W^\pm}^{True})}{M_{W^\pm}^{True}}$
3. $\frac{(M_{W^\pm}^{Fit} - M_{W^\pm}^{True})}{\delta M_{W^\pm}^{Fit}}$

In this notation, $M_{W^\pm}^{Fit}$ and $\delta M_{W^\pm}^{Fit}$ represent the indirectly measured M_{W^\pm} and its uncertainty, and $M_{W^\pm}^{True}$ stands for the nominal W^\pm boson mass.

The first figure of merit (1.) reflects the intrinsic resolution power of the indirect mass measurement, irrespective of its possible biases, it's expressed in %. The second and the third ones measure the accuracy with respect to the nominal W^\pm boson mass: firstly as a relative uncertainty in % irrespective of the precision of the method (2.) and secondly as a compatibility between the nominal and the predicted masses given the precision of the method (3.), expressed in number of standard deviations (σ).

Figures of Merit of the Accuracy	Considered LO PDFs		
	MRST2007lomod	CTEQ6L1	MSTW2008lo68cl
1. $\frac{\delta M_{W^\pm}^{Fit}}{M_{W^\pm}^{Fit}}$	1.2%	0.8%	2.1%
2. $\frac{(M_{W^\pm}^{Fit} - M_{W^\pm}^{True})}{M_{W^\pm}^{True}}$	-0.1%	-1.8%	+1.2%
3. $\frac{(M_{W^\pm}^{Fit} - M_{W^\pm}^{True})}{\delta M_{W^\pm}^{Fit}}$	-0.1 σ	-2.3 σ	+0.6 σ

Table 15. Summary of the indirect mass measurements of M_{W^\pm} extracted from the integral charge asymmetry of the $W^\pm \rightarrow \ell^\pm \nu$ process. Different figures of merit of the accuracy of these measurements are presented.

The values of the figures of merit in table 15 show that already at LO, this new method enables to get a good estimate of the W^\pm boson mass.

3 Inclusive Production of $\tilde{\chi}_1^\pm + \tilde{\chi}_2^0 \rightarrow 3\ell^\pm + \cancel{E}_T$

3.1 Theoretical Prediction of $A_C(\tilde{\chi}_1^\pm + \tilde{\chi}_2^0)$

In this section we repeat the types of calculations done in section 2.1 but now for a process of interest in R-parity conserving SUSY searches, namely the $p + p \rightarrow \tilde{\chi}_1^\pm + \tilde{\chi}_2^0 \rightarrow 3\ell^\pm + \cancel{E}_T$ inclusive production.

We use Resummino v1.0.0 [14] to calculate the $p + p \rightarrow \tilde{\chi}_1^\pm + \tilde{\chi}_2^0$ cross sections at different levels of theoretical accuracy. At fixed order in QCD we run these calculations at the LO and the NLO. In addition, we also run them starting from the NLO MEs and including the "Next-to-Leading Log" (NLL) analytically resummed corrections. The latter, sometimes referred to as "NLO+NLL" will simply be denoted "NLL" in the following.

We calculate these cross sections at $\sqrt{s} = 8$ TeV using "Simplified Models" [13] for the following masses:

$$M_{\tilde{\chi}_1^\pm} = M_{\tilde{\chi}_2^0} = 100, 105, 115, 125, 135, 145, 150, 200, 250, 300, 400, 500, 600, 700 \text{ GeV}$$

and using the PDFs reported in table 16. We set the QCD scales as $\mu_R = \mu_F = \mu_0 = M_{\tilde{\chi}_1^\pm} + M_{\tilde{\chi}_2^0}$. Regarding the phase space sampling, a statistical precision of 0.1% is requested for the numerical integration of the cross sections.

LO	NLO & NLL
MRST2007lomod	MRST2004nlo
CTEQ6L1	CTEQ6.1
MSTW2008lo68cl	MSTW2008nlo68cl

Table 16. PDFs used for the calculations of $\sigma(\tilde{\chi}_1^\pm + \tilde{\chi}_2^0)$ at the LO in QCD and the NLO and the NLL.

The integral charge asymmetries as functions of $M_{\tilde{\chi}_1^\pm} + M_{\tilde{\chi}_2^0}$ for this process are presented in tables 17, 19, and 21 for the MRST2007lomod/MRST2004nlo, the CTEQ6L1/CTEQ6.1, and the MSTW2008lo68cl/MSTW2008nlo68cl PDFs, respectively.

3.1.1 $A_C(\tilde{\chi}_1^\pm + \tilde{\chi}_2^0)$ Template Curves for MRST

The theoretical MRST A_C template curves are obtained by computing the A_C based upon the cross sections of the signed processes used for table 17. They are displayed in figure 9.

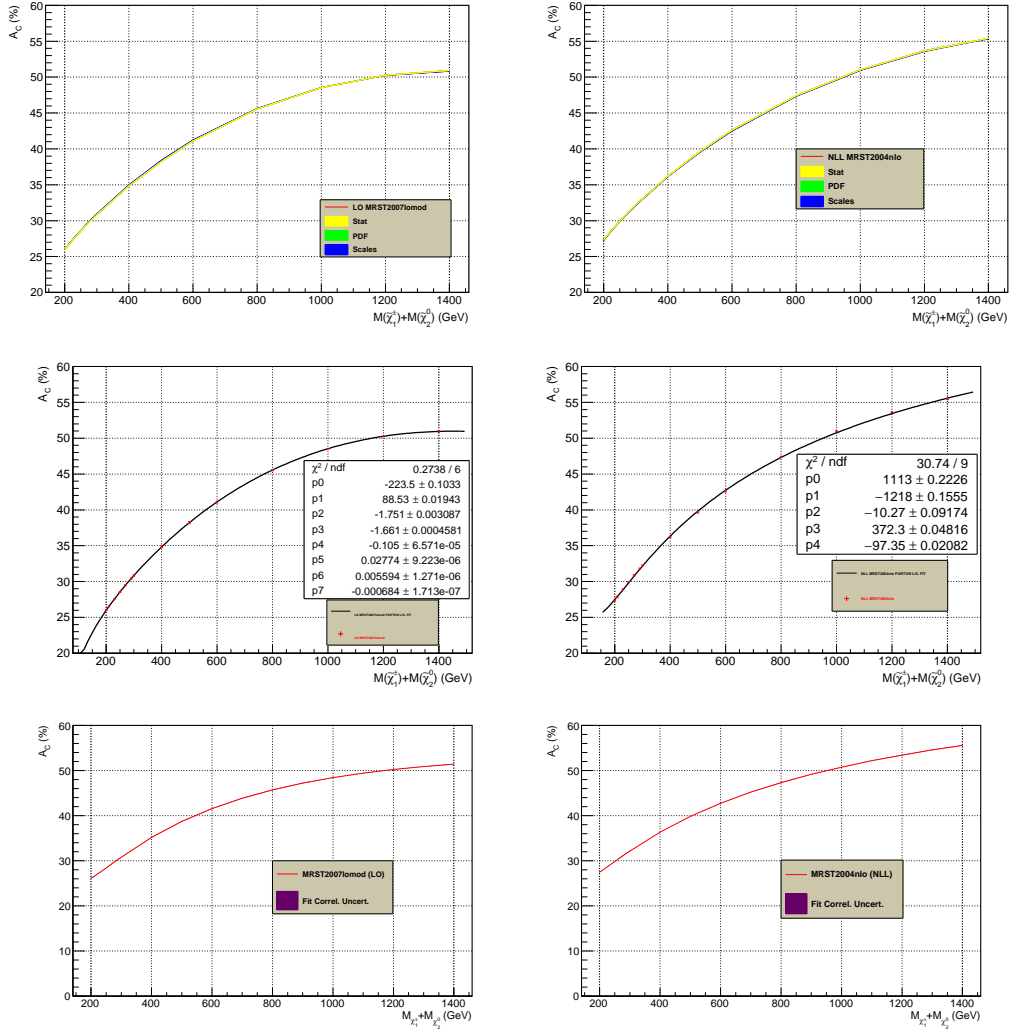


Figure 9. The theoretical MRST A_C template curves. The raw curve with its uncertainty bands and the corresponding fitted curve with uncorrelated and with correlated uncertainties are displayed on the top, the middle and the bottom rows, respectively. The LHS concerns the LO calculations based upon the MRST2007lomod PDF and the RHS concerns the NLL calculations using the MRST2004nlo PDF.

$M_{\chi_1^\pm + \chi_2^0}$ (GeV)	A_C (%)	$\delta(A_C)_{Stat}$ (%)	$\delta(A_C)_{Scale}$ (%)	$\delta(A_C)_{PDF}$ (%)	$\delta(A_C)_{Total}$ (%)
200.	LO: 25.991 NLL: 27.363	± 0.004 ± 0.011	-0.037 $+0.056$ $+0.092$ -0.074	0.000 not quoted	$+0.037$ -0.056 $+0.093$ -0.075
210.	LO: 26.52 NLL: 27.904	± 0.003 ± 0.009	-0.046 $+0.063$ $+0.100$ -0.066	0.000 not quoted	$+0.046$ -0.063 $+0.101$ -0.067
230.	LO: 27.562 NLL: 28.938	± 0.002 ± 0.006	-0.061 $+0.074$ $+0.098$ -0.056	0.000 not quoted	$+0.061$ -0.074 $+0.099$ -0.057
250.	LO: 28.549 NLL: 29.934	± 0.002 ± 0.004	-0.073 $+0.085$ $+0.084$ -0.072	0.000 not quoted	$+0.074$ -0.085 $+0.084$ -0.073
270.	LO: 29.495 NLL: 30.877	± 0.001 ± 0.003	-0.084 $+0.094$ $+0.085$ -0.088	0.000 not quoted	$+0.084$ -0.094 $+0.085$ -0.088
290.	LO: 30.403 NLL: 31.786	± 0.001 ± 0.002	-0.094 $+0.102$ $+0.079$ -0.091	0.000 not quoted	$+0.094$ -0.102 $+0.079$ -0.091
300.	LO: 30.844 NLL: 32.229	± 0.001 ± 0.002	-0.098 $+0.106$ $+0.076$ -0.093	0.000 not quoted	$+0.098$ -0.106 $+0.076$ -0.093
400.	LO: 34.847 NLL: 36.213	± 0.000 ± 0.001	-0.125 $+0.126$ $+0.086$ -0.069	0.000 not quoted	$+0.125$ -0.126 $+0.086$ -0.069
500.	LO: 38.230 NLL: 39.648	± 0.000 ± 0.000	-0.132 $+0.131$ $+0.101$ -0.100	0.000 not quoted	$+0.132$ -0.131 $+0.101$ -0.100
600.	LO: 41.101 NLL: 42.600	± 0.000 ± 0.000	-0.127 $+0.124$ $+0.104$ -0.129	0.000 not quoted	$+0.127$ -0.124 $+0.104$ -0.129
800.	LO: 45.548 NLL: 47.420	± 0.000 ± 0.000	-0.091 $+0.086$ $+0.118$ -0.073	0.000 not quoted	$+0.091$ -0.086 $+0.118$ -0.073
1000.	LO: 48.528 NLL: 51.035	± 0.000 ± 0.000	-0.038 $+0.033$ $+0.116$ -0.063	0.000 not quoted	$+0.038$ -0.033 $+0.116$ -0.063
1200.	LO: 50.264 NLL: 53.658	± 0.000 ± 0.000	$+0.024$ -0.025 $+0.101$ $+0.021$	0.000 not quoted	$+0.024$ -0.025 $+0.101$ -0.021
1400.	LO: 50.924 NLL: 55.404	± 0.000 ± 0.000	$+0.088$ -0.081 $+0.008$ -0.083	0.000 not quoted	$+0.088$ -0.081 $+0.008$ -0.083

Table 17. The MRST $A_C(\tilde{\chi}_1^\pm \tilde{\chi}_2^0)$ table with the breakdown of the different sources of theoretical uncertainty.

3.1.2 $A_C(\tilde{\chi}_1^\pm + \tilde{\chi}_2^0)$ Template Curves for CTEQ6

The theoretical CTEQ6 A_C template curves are obtained by computing the A_C based upon the cross sections of the signed processes used for table 19. They are displayed in figure 10.

$M_{\chi_1^\pm} + M_{\chi_2^0}$ (GeV) (GeV)	A_C^{Fit} (%)	δA_C^{Fit} (%)
200.	LO: 25.984 NLL: 27.435	± 0.025 ± 0.031
210.	LO: 26.530 NLL: 27.927	± 0.024 ± 0.030
230.	LO: 27.571 NLL: 28.904	± 0.024 ± 0.028
250.	LO: 28.557 NLL: 29.866	± 0.023 ± 0.027
270.	LO: 29.498 NLL: 30.807	± 0.023 ± 0.027
290.	LO: 30.400 NLL: 31.724	± 0.022 ± 0.026
300.	LO: 30.838 NLL: 32.172	± 0.022 ± 0.026
400.	LO: 34.824 NLL: 36.286	± 0.021 ± 0.025
500.	LO: 38.215 NLL: 39.768	± 0.020 ± 0.027
600.	LO: 41.102 NLL: 42.720	± 0.019 ± 0.029
800.	LO: 45.562 NLL: 47.400	± 0.016 ± 0.034
1000.	LO: 48.532 NLL: 50.881	± 0.015 ± 0.041
1200.	LO: 50.261 NLL: 53.508	± 0.017 ± 0.049
1400.	LO: 50.945 NLL: 55.501	± 0.022 ± 0.057

Table 18. The MRST $A_C^{Fit}(\tilde{\chi}_1^\pm \tilde{\chi}_2^0)$ table with its theoretical uncertainty accounting for the correlations between the parameters fitting the A_C^{Raw} template curves.

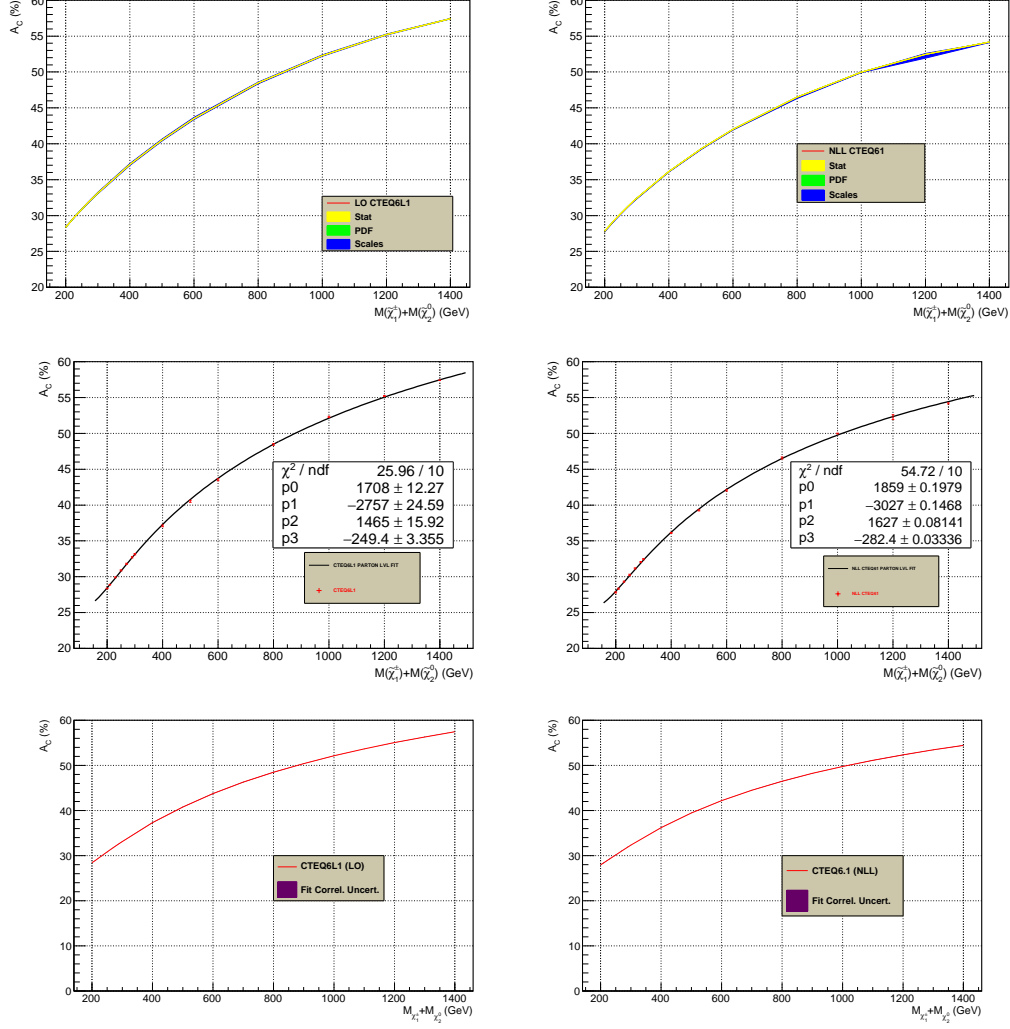


Figure 10. The theoretical CTEQ6 A_C template curves. The raw curve with its uncertainty bands and the corresponding fitted curve with uncorrelated and with correlated uncertainties are displayed on the top, the middle and the bottom rows, respectively. The LHS concerns the LO calculations based upon the CTEQ6L1 PDF and the RHS concerns the NLL calculations using the CTEQ6.1 PDF.

$M_{\chi_1^\pm} + M_{\chi_2^0}$ (GeV)	A_C (%)	$\delta(A_C)_{Stat}$ (%)	$\delta(A_C)_{Scale}$ (%)	$\delta(A_C)_{PDF}$ (%)	$\delta(A_C)_{Total}$ (%)
200.	LO: 28.367 NLL: 27.822	± 0.003 ± 0.010	-0.030 $+0.045$ $+0.076$ -0.074	0.000 not quoted	$+0.030$ -0.045 $+0.077$ -0.075
210.	LO: 28.896 NLL: 28.345	± 0.003 ± 0.008	-0.038 $+0.051$ $+0.084$ -0.069	0.000 not quoted	$+0.038$ -0.051 $+0.084$ -0.069
230.	LO: 29.911 NLL: 29.333	± 0.002 ± 0.006	-0.053 $+0.064$ $+0.102$ -0.054	0.000 not quoted	$+0.053$ -0.064 $+0.102$ -0.054
250.	LO: 30.880 NLL: 30.273	± 0.001 ± 0.004	-0.066 $+0.074$ $+0.093$ -0.064	0.000 not quoted	$+0.066$ $+0.074$ $+0.093$ -0.064
270.	LO: 31.808 NLL: 31.169	± 0.001 ± 0.003	-0.077 $+0.084$ $+0.078$ -0.070	0.000 not quoted	$+0.077$ -0.084 $+0.078$ -0.070
290.	LO: 32.701 NLL: 32.026	± 0.001 ± 0.002	-0.087 $+0.092$ $+0.065$ -0.090	0.000 not quoted	$+0.087$ -0.092 $+0.065$ -0.090
300.	LO: 33.135 NLL: 32.434	± 0.001 ± 0.002	-0.091 $+0.096$ $+0.065$ -0.089	0.000 not quoted	$+0.091$ -0.096 $+0.065$ -0.089
400.	LO: 37.104 NLL: 36.136	± 0.000 ± 0.001	-0.121 $+0.121$ $+0.080$ -0.055	0.000 not quoted	$+0.121$ -0.121 $+0.080$ -0.055
500.	LO: 40.531 NLL: 39.285	± 0.000 ± 0.000	-0.134 $+0.131$ $+0.088$ -0.057	0.000 not quoted	$+0.134$ -0.131 $+0.088$ -0.057
600.	LO: 43.527 NLL: 42.023	± 0.000 ± 0.000	-0.137 $+0.132$ $+0.056$ -0.119	0.000 not quoted	$+0.137$ -0.132 $+0.056$ -0.119
800.	LO: 48.473 NLL: 46.514	± 0.000 ± 0.000	-0.121 $+0.116$ $+0.094$ -0.194	0.000 not quoted	$+0.121$ -0.116 $+0.094$ -0.194
1000.	LO: 52.293 NLL: 49.985	± 0.000 ± 0.000	-0.094 $+0.090$ $+0.054$ -0.053	0.000 not quoted	$+0.094$ -0.090 $+0.054$ -0.053
1200.	LO: 55.219 NLL: 52.447	± 0.000 ± 0.000	-0.063 $+0.061$ $+0.528$ $+0.147$	0.000 not quoted	$+0.063$ -0.061 $+0.528$ -0.147
1400.	LO: 57.428 NLL: 54.190	± 0.000 ± 0.000	-0.034 $+0.033$ $+0.069$ -0.081	0.000 not quoted	$+0.034$ -0.033 $+0.069$ -0.081

Table 19. The CTEQ6 $A_C(\tilde{\chi}_1^\pm \tilde{\chi}_2^0)$ table with the breakdown of the different sources of theoretical uncertainty.

$M_{\chi_1^\pm} + M_{\chi_2^0}$ (GeV) (GeV)	A_C^{Fit} (%)	δA_C^{Fit} (%)
200.	LO: 28.407 NLL: 27.811	± 0.034 ± 0.027
210.	LO: 28.900 NLL: 28.340	± 0.027 ± 0.026
230.	LO: 29.876 NLL: 29.342	± 0.023 ± 0.024
250.	LO: 30.832 NLL: 30.282	± 0.027 ± 0.023
270.	LO: 31.766 NLL: 31.172	± 0.032 ± 0.022
290.	LO: 32.674 NLL: 32.018	± 0.037 ± 0.022
300.	LO: 33.119 NLL: 32.428	± 0.038 ± 0.022
400.	LO: 37.203 NLL: 36.126	± 0.046 ± 0.023
500.	LO: 40.687 NLL: 39.287	± 0.048 ± 0.026
600.	LO: 43.675 NLL: 42.041	± 0.052 ± 0.027
800.	LO: 48.507 NLL: 46.558	± 0.058 ± 0.030
1000.	LO: 52.220 NLL: 49.977	± 0.052 ± 0.033
1200.	LO: 55.133 NLL: 52.477	± 0.034 ± 0.041
1400.	LO: 57.447 NLL: 54.189	± 0.032 ± 0.052

Table 20. The CTEQ $A_C^{Fit}(\tilde{\chi}_1^\pm \tilde{\chi}_2^0)$ table with its theoretical uncertainty accounting for the correlations between the parameters fitting the A_C^{Raw} template curves.

3.1.3 $A_C(\tilde{\chi}_1^\pm + \tilde{\chi}_2^0)$ Template Curves for MSTW2008

The theoretical MSTW2008lo68cl A_C template curves are obtained by computing the A_C based upon the cross sections of the signed processes used for table 21. They are displayed in figure 11.

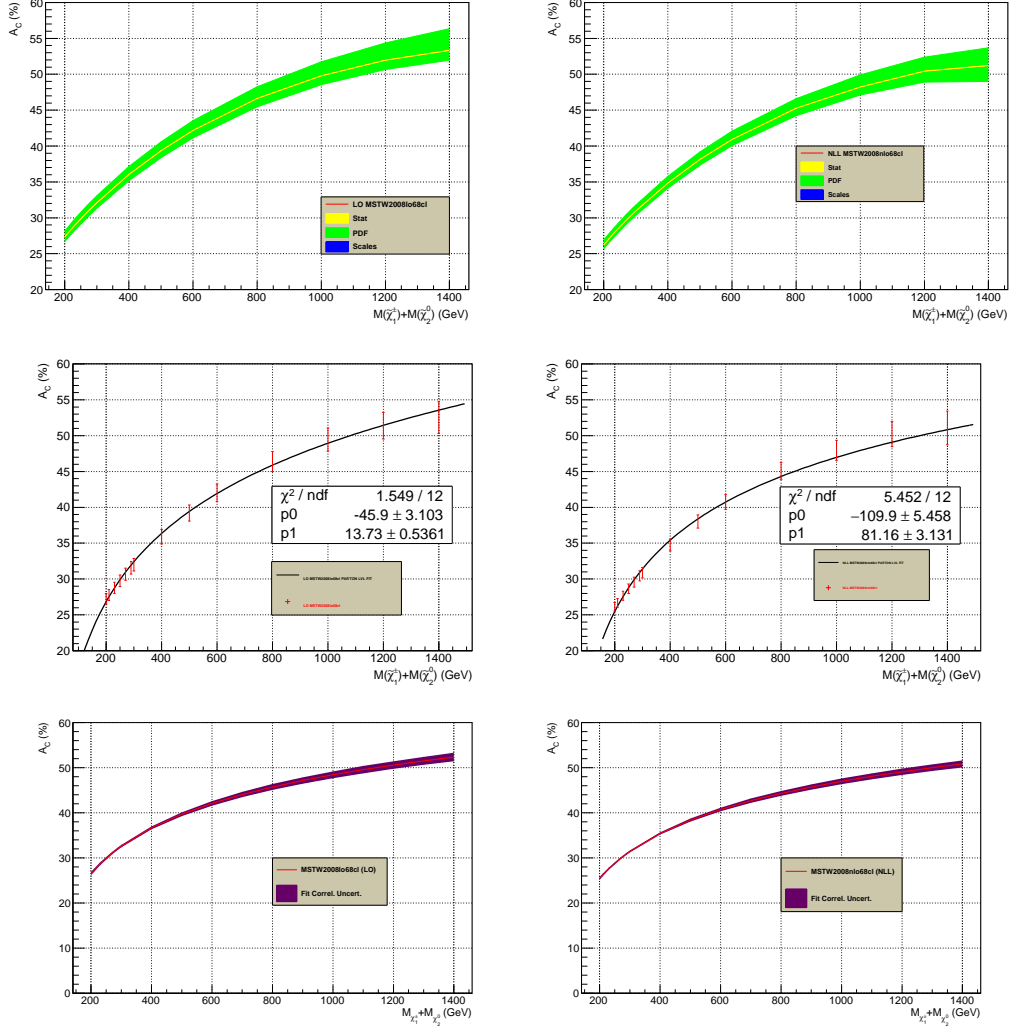


Figure 11. The theoretical MSTW2008 A_C template curves. The raw curve with its uncertainty bands and the corresponding fitted curve with uncorrelated and with correlated uncertainties are displayed on the top, the middle and the bottom rows, respectively. The LHS concerns the LO calculations based upon the MSTW2008lo68cl PDF and the RHS concerns the NLL calculations using the MSTW2008nlo68cl PDF.

$M_{\chi_1^\pm} + M_{\chi_2^0}$ (GeV)	A_C (%)	$\delta(A_C)_{Stat}$ (%)	$\delta(A_C)_{Scale}$ (%)	$\delta(A_C)_{PDF}$ (%)	$\delta(A_C)_{Total}$ (%)
200.	LO: 27.330	± 0.003	-0.034 +0.049	+0.827 -0.649	+0.828 -0.651
	NLL: 26.215	± 0.011	+0.091 -0.067	+0.682 -0.518	+0.688 -0.522
210.	LO: 27.857	± 0.003	-0.042 +0.056	+0.845 -0.663	+0.846 -0.665
	NLL: 26.744	± 0.009	+0.080 -0.056	+0.694 -0.530	+0.698 -0.533
230.	LO: 28.872	± 0.002	-0.056 -0.068	+0.878 -0.690	+0.880 -0.693
	NLL: 27.757	± 0.006	+0.085 -0.040	+0.722 -0.549	+0.727 -0.550
250.	LO: 29.842	± 0.001	-0.069 +0.078	+0.911 -0.716	+0.913 -0.720
	NLL: 28.730	± 0.004	+0.073 -0.053	+0.747 -0.573	+0.751 -0.575
270.	LO: 30.770	± 0.001	-0.080 +0.087	+0.942 -0.742	+0.945 -0.747
	NLL: 29.658	± 0.003	+0.063 -0.069	+0.773 -0.595	+0.775 -0.599
290.	LO: 31.662	± 0.001	-0.088 +0.094	+0.972 -0.766	+0.976 -0.772
	NLL: 30.540	± 0.002	+0.058 -0.080	+0.802 -0.608	+0.804 -0.613
300.	LO: 32.096	± 0.001	-0.092 +0.097	+0.987 -0.778	+0.991 -0.784
	NLL: 30.969	± 0.002	+0.068 -0.089	+0.802 -0.625	+0.805 -0.632
400.	LO: 36.028	± 0.000	-0.117 +0.117	+1.123 -0.885	+1.129 -0.893
	NLL: 34.846	± 0.001	+0.105 -0.043	+0.929 -0.713	+0.935 -0.714
500.	LO: 39.351	± 0.000	-0.123 +0.122	+1.250 -0.971	+1.256 -0.979
	NLL: 38.145	± 0.000	+0.097 -0.093	+1.042 -0.803	+1.047 -0.808
600.	LO: 42.179	± 0.000	-0.118 +0.116	+1.372 -1.043	+1.377 -1.050
	NLL: 40.906	± 0.000	+0.121 -0.103	+1.171 -0.841	+1.177 -0.847
800.	LO: 46.628	± 0.000	-0.088 +0.085	+1.627 -1.161	+1.629 -1.164
	NLL: 45.265	± 0.000	+0.101 -0.080	+1.352 -1.027	+1.356 -1.030
1000.	LO: 49.793	± 0.000	-0.051 +0.046	+1.953 -1.242	+1.953 -1.243
	NLL: 48.243	± 0.000	+0.112 -0.019	+1.674 -1.124	+1.678 -1.125
1200.	LO: 51.956	± 0.000	-0.014 +0.013	+2.407 -1.301	+2.408 -1.301
	NLL: 50.430	± 0.000	+0.031 -0.000	+1.966 -1.534	+1.966 -1.534
1400.	LO: 53.328	± 0.000	+0.018 -0.013	+3.019 -1.375	+3.019 -1.375
	NLL: 51.216	± 0.000	-0.082 +0.060	+2.470 -2.216	+2.472 -2.217

Table 21. The MSTW2008 $A_C(\tilde{\chi}_1^\pm \tilde{\chi}_2^0)$ table with the breakdown of the different sources of theoretical uncertainty.

3.1.4 Comparing the different A_C Template Curves

Here again we compare the A_C template curves produced with different PDFs using Resumino this time. From figure 12 we can see that the A_C of the different PDF used at LO and at NLO are in agreement only at the $\pm 3\sigma$ level. This figure also displays the $\frac{A_C^{NLL}}{A_C^{LO}}$ ratios for the three families of PDFs used.

$M_{\tilde{\chi}_1^\pm} + M_{\tilde{\chi}_2^0}$ (GeV)	A_C^{Fit} (%)	δA_C^{Fit} (%)
200.	LO: 26.841746 NLL: 25.767	± 0.358 ± 0.304
210.	LO: 27.512 NLL: 26.426	± 0.341 ± 0.286
230.	LO: 28.761 NLL: 27.656	± 0.310 ± 0.257
250.	LO: 29.905 NLL: 28.783	± 0.287 ± 0.235
270.	LO: 30.962 NLL: 29.824	± 0.271 ± 0.220
290.	LO: 31.943 NLL: 30.790	± 0.261 ± 0.212
300.	LO: 32.409 NLL: 31.248	± 0.258 ± 0.211
400.	LO: 36.358 NLL: 35.138	± 0.282 ± 0.251
500.	LO: 39.422 NLL: 38.1545	± 0.350 ± 0.328
600.	LO: 41.925 NLL: 40.619	± 0.423 ± 0.405
800.	LO: 45.875 NLL: 44.509	± 0.554 ± 0.537
1000.	LO: 48.939 NLL: 47.526	± 0.663 ± 0.644
1200.	LO: 51.442 NLL: 49.991	± 0.754 ± 0.733
1400.	LO: 53.559 NLL: 52.075	± 0.832 ± 0.810

Table 22. The MSTW $A_C^{Fit}(\tilde{\chi}_1^\pm \tilde{\chi}_2^0)$ table with its theoretical uncertainty accounting for the correlations between the parameters fitting the A_C^{Raw} template curve.

3.2 Experimental Measurement of $A_C(\tilde{\chi}_1^\pm + \tilde{\chi}_2^0 \rightarrow 3\ell^\pm + \cancel{E}_T)$

The aim of this sub-section is to repeat, in the context of the considered SUSY signal, a study similar to that of section 2.2.

We use Simplified Models to generate our signal in the two configurations shown in figure 13.

The first signal configuration, denoted S1, supposes that the lightest part of the SUSY mass spectrum is made of $\tilde{\chi}_1^\pm$, $\tilde{\chi}_2^0$, $\tilde{\ell}^\pm$ (i.e. \tilde{e}^\pm or $\tilde{\mu}^\pm$), and $\tilde{\chi}_1^0$, in order of decreasing mass.

practice, within the MSSM, these branching ratios not only depend on the envisaged mass hierarchy, but also on the fields composition of the $\tilde{\chi}_2^0$, the $\tilde{\chi}_1^\pm$, and the $\tilde{\chi}_1^0$. Regarding the SM leptonic decays of the W^\pm and the Z^0 gauge bosons, we used their actual SM branching ratios. This will have the obvious consequence of a much smaller event yield for the S2 signals compared to the S1 signals of same mass.

The hypotheses common to configurations S1 and S2 are that the lightest SUSY particle (LSP) is the $\tilde{\chi}_1^0$, and that the $\tilde{\chi}_2^0$ and the $\tilde{\chi}_1^\pm$ are mass degenerate.

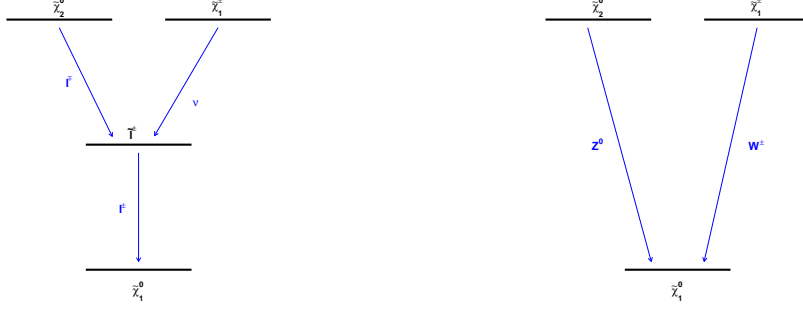


Figure 13. The sketch of the Simplified Models used to generate the signal samples: the S1 signal (LHS) has a $\tilde{\ell}^\pm$ NLSP whereas for the S2 signal (RHS) the mass degenerate $\tilde{\chi}_1^\pm$ and $\tilde{\chi}_2^0$ are the NLSPs. Both signals share the $\tilde{\chi}_1^0$ as the LSP.

3.2.1 Monte Carlo Generation

We generate a new set of MC samples. We report here only the MC parameters that are different from those used in sub-section 2.2.1. We use the following LO generator: Herwig++ v2.5.2 for the SUSY signal and for most of the background processes.

The other background processes: $W^+ + W^- + W^\pm$, $W^+ + W^- + \gamma^*/Z$, $W^\pm + \gamma^*/Z + \gamma^*/Z$, $W^\pm + 1c + 0Lp$, $W^\pm + 1c + 1Lp$, $W^\pm + c\bar{c} + 0Lp$, $W^\pm + b\bar{b} + 0Lp$, $W^\pm + t\bar{t} + 0Lp$ are generated using Alpgen v2.14 at the parton level. Those samples are passed on to Pythia v8.170 for the parton showering, the fragmentation of the colored particles, the modelling of the underlying event and the decay of the unstable particles.

For the $W^\pm + HF$ process, and the VVV processes in Alpgen the only decay mode generated is $\gamma^*/Z(\rightarrow f\bar{f})$ where $f = \ell^\pm, \tau^\pm, \nu, q$ and $75 < M(f\bar{f}) < 125$ GeV, whereas for the $W^\pm(\rightarrow e^\pm\nu_e/\mu^\pm\nu_\mu/\tau^\pm\nu_\tau)$ process no mass cuts are applied.

For the $W + HF$ processes, the renormalization scale is set to

$$\mu_R = \mu_F = \sqrt{M^2(W) + \sum_{i=1}^{N_p^{FS}} M_T^2(i)}$$

where the i index runs over the number of FS partons N_p^{FS} , and where $M_T^2 = M^2 + p_T^2$.

In particular for the signal samples, we test distinct mass hypotheses in different configurations.

For the S1 signal, we vary $M_{\tilde{\chi}_2^0}$ in the range [100,700] GeV by steps of 100 GeV, and we set $M_{\tilde{\chi}_1^0} = M_{\tilde{\chi}_2^0}/2$ and $M_{\tilde{\ell}^\pm} = [M_{\tilde{\chi}_2^0} + M_{\tilde{\chi}_1^\pm}]/2$.

For the S2 signal, we produce a single "S2a" sample, i.e. with $M_{\tilde{\chi}_2^0} - M_{\tilde{\chi}_1^0} < M_Z$, for which we set $M_{\tilde{\chi}_2^0} = 100$ GeV, $M_{\tilde{\chi}_1^0} = 50$ GeV. This enables to explore the case where the $\tilde{\chi}_1^\pm$ and the $\tilde{\chi}_2^0$ decay through a W^\pm and through a Z that are both off-shell. For the other S2 samples, denoted "S2b" and described in the following paragraph, both the W^\pm and the Z bosons are on-shell. In addition, we vary $M_{\tilde{\chi}_2^0}$ in the range [200,700] GeV by steps of 100 GeV, setting $M_{\tilde{\chi}_1^0} = M_{\tilde{\chi}_2^0}/2$. We also vary $M_{\tilde{\chi}_2^0}$ in the range [105,145] GeV by steps of 10 GeV with a fixed value of $M_{\tilde{\chi}_1^0} = 13.8$ GeV. And finally, we added two samples: $[M_{\tilde{\chi}_2^0}, M_{\tilde{\chi}_1^0}] = [150,50]$ GeV and $[250,125]$ GeV.

3.2.2 Analysis of the $\tilde{\chi}_1^\pm \tilde{\chi}_2^0 \rightarrow 3\ell^\pm + \cancel{E}_T$ Process

We considered only the electron and the muon channels. For these analyses we set the integrated luminosity to $\int \mathcal{L} dt = 20 \text{ fb}^{-1}$.

1). Event Selection in the Trilepton Channel

A first set of requirements related to the leptons are applied for the event selection as mentioned hereafter:

1. $N(\ell^\pm) \geq 3$
2. Electron candidates:
 - (a) $|\eta(e^\pm)| < 1.37 \text{ or } 1.53 < |\eta(e^\pm)| < 2.47$
 - (b) $p_T(e^\pm) > 10 \text{ GeV}$
3. Muon candidates:
 - (a) $|\eta(\mu^\pm)| < 2.4$
 - (b) $p_T(\mu^\pm) > 10 \text{ GeV}$
4. $p_T(\ell_1^\pm) > 20 \text{ GeV}$
5. $p_T(\ell_2^\pm) > 10 \text{ GeV}$
6. $p_T(\ell_3^\pm) > 10 \text{ GeV}$
7. Tracker Isolation: reject events with additional tracks of $p_T > 2 \text{ GeV}$ within a cone of $\Delta R = 0.5$ around the direction of the ℓ^\pm track
8. Calorimeter Isolation: ratio of the scalar sum of E_T deposits in the calorimeter within a cone of $\Delta R = 0.5$ around the direction of the ℓ^\pm , to the $p_T(\ell^\pm)$ must be less than 1.2 for e^\pm and less than 0.25 for μ^\pm
9. $\cancel{E}_T > 35 \text{ GeV}$

10. $M_{T2} > 75$ GeV

The latter cut is applied on the so-called "stransverse mass": M_{T2} . We used a boost-corrected calculation of this variable as described in [56] and implemented in MCTLib [57].

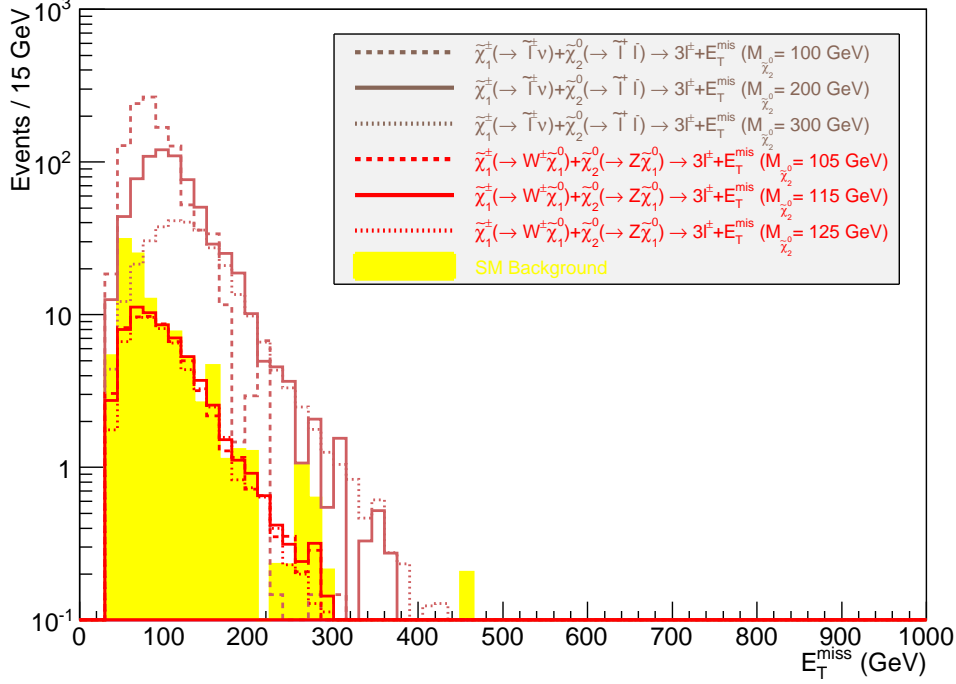


Figure 14. Distribution of the E_T after the event selection. The background, the S1, and the S2 signals are the filled yellow, the hollow brown, and the hollow red histograms, respectively.

The event selection efficiencies, event yields, signal significances and the expected integral charge asymmetries are reported in table 23. Figure 14 displays the E_T distribution after the event selection.

We note that the S1 signal significance exceeds 5σ for $M_{\tilde{\chi}_2^0} = M_{\tilde{\chi}_1^\pm}$ in the $[100, 400]$ GeV interval, whereas the S2 signal significance reaches only the 3σ for $100 < M_{\tilde{\chi}_2^0} = M_{\tilde{\chi}_1^\pm} < 150$ GeV.

In this simple version of the analysis, we keep the same event selection for both the S1 and the S2 signals. Therefore these signal samples share the same residual background as well as the same bias from the event selection. In these conditions, we could use a common A_C template curve for both of them. However, because we choose many overlapping masses between these two signal samples, we split them into two separate sets of experimental A_C template curves. The S1 A_C template curve, that include the propagation of the realistic experimental uncertainties into each term of equation 2.11, are displayed in figure 15, the S2 ones are displayed in figure 16. And the final signal template curves for which the

uncertainties account for the correlations between the parameters used to fit the A_C^{Meas} template curves are shown in figure 17, on the LHS for S1 and on the RHS for S2.

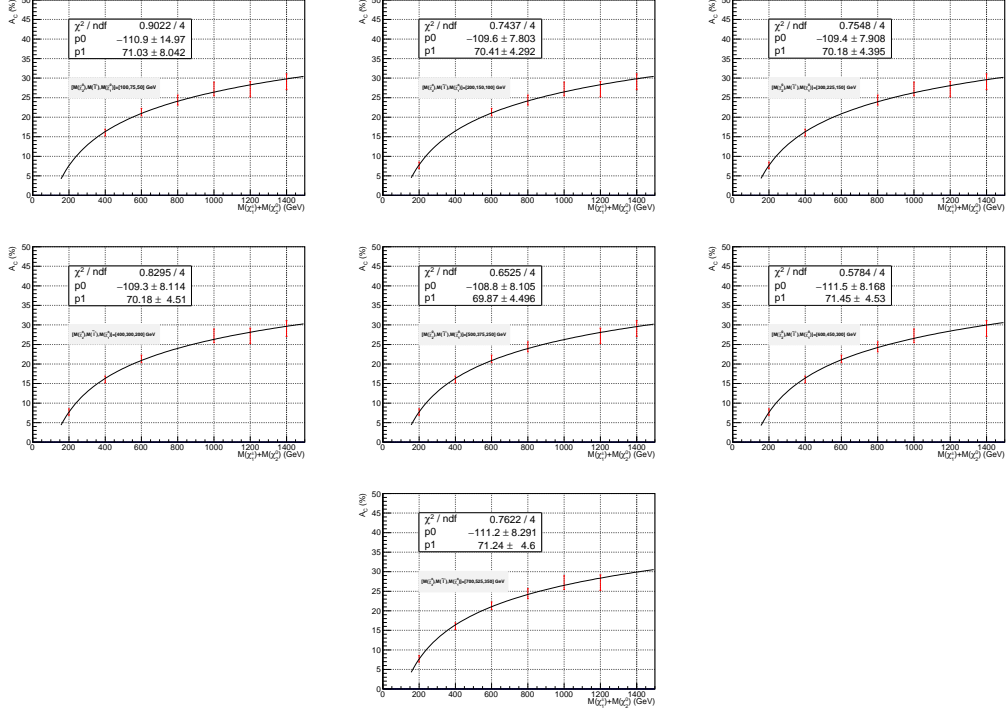


Figure 15. Experimental A_C template curves for the S1 signal samples, as they are listed, in table 23 from the top to the bottom rows. Here, they appear ordered by increasing $\tilde{\chi}_2^0$ mass, from the top to the bottom row and from left to right.

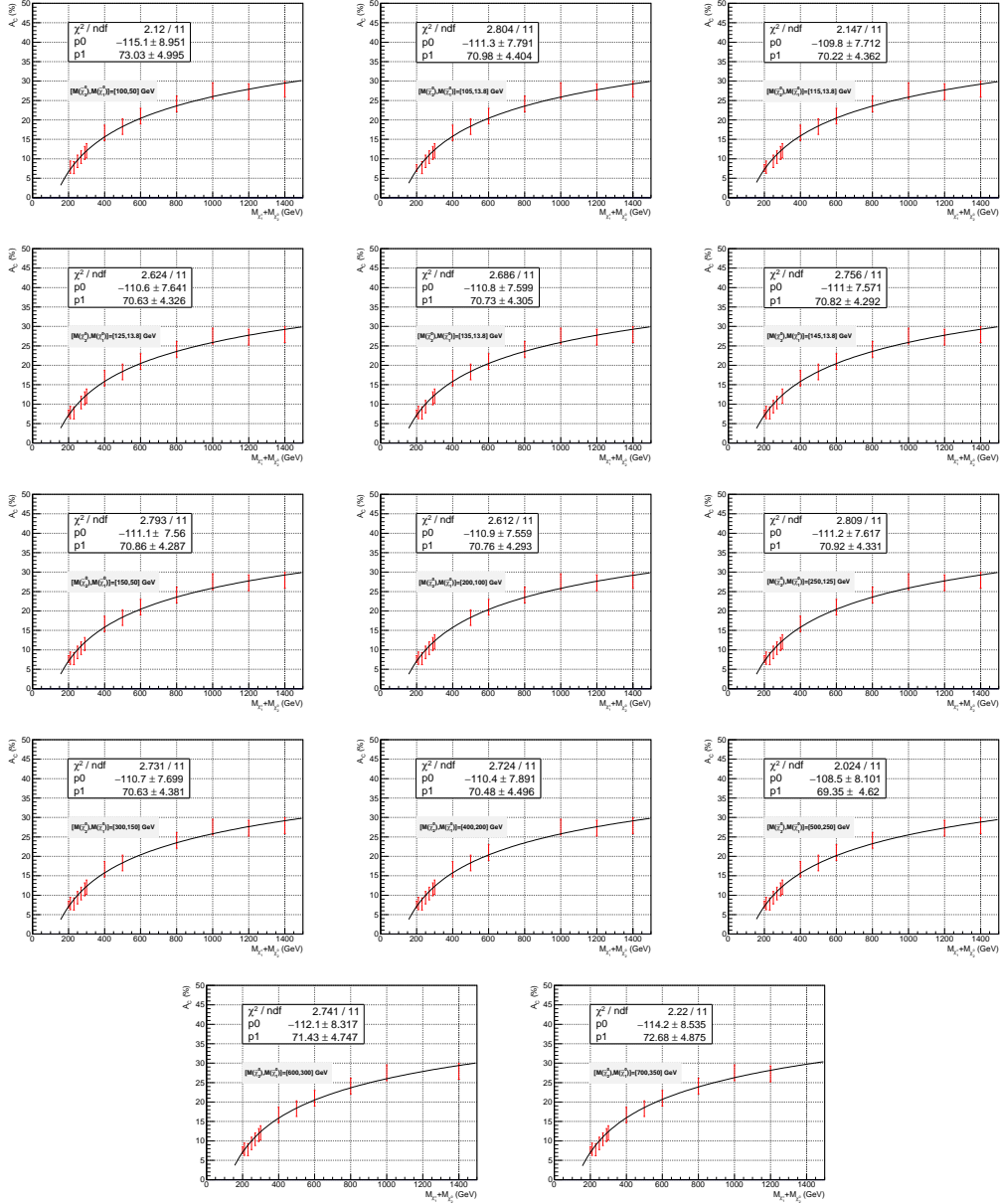


Figure 16. Experimental A_C template curves for the S2 signal samples, as they are listed, in table 23 from the top to the bottom rows. Here, they appear ordered by increasing $\tilde{\chi}_2^0$ mass, from the top to the bottom row and from left to right.

3.3 Indirect Determination of $M_{\tilde{\chi}_1^\pm} + M_{\tilde{\chi}_2^0}$

3.3.1 Experimental Result for the S1 Signal

Using the S1 signal experimental A_C template curves of figure 15, we can get the central values and the uncertainties of the indirectly measured $M_{\tilde{\chi}_1^\pm} + M_{\tilde{\chi}_2^0}$ for each input mass as reported in table 25.

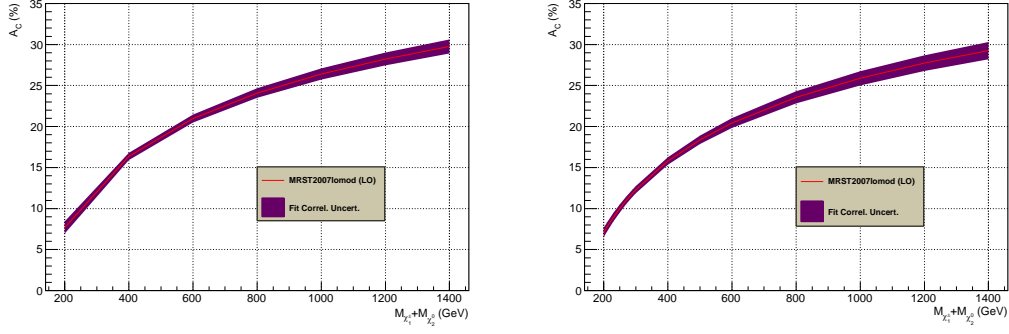


Figure 17. Fitted A_C template curves for the S1 (LHS) and the S2 (RHS) signal samples. The uncertainty accounts for the correlations between the parameters used to fit the A_C^{Meas} template curves.

This enables us to perform a closure test of our method on the S1 signal sample as displayed at the top of figure 18, where we can fit of the input versus the measured $M_{\chi_1^\pm} + M_{\chi_2^0}$ by a linear function.

This fit indicates, given the uncertainties, that the indirect measurement is:

$$\begin{cases} \text{linear : the slope of the fit function is compatible with 1} \\ \text{unbiased : the y - intercept of the fit function is compatible with 0} \end{cases} \quad (3.1)$$

Further elementary checks, forcing the parameters of the fit functions, tend to confirm these indications, as presented in table 26.

3.3.2 Experimental Result for the S2 Signal

As in the previous sub-section, using the S2 signal A_C template curves 16, we can get the results reported in table 27. The closure test on the S2 signal samples is displayed at the bottom of figure 18.

<i>Process</i>	ϵ (%)	N_{exp} (Evs)	Z_N	$A_C^{Exp} \pm \delta A_C^{Stat}$ (%)
S1 Signal				
$[M_{\tilde{\chi}_2^0}, M_{\tilde{\ell}^\pm}, M_{\tilde{\chi}_1^0}]$ GeV				
[100, 75, 50]	0.45 ± 0.01	1097.43	31.70	(7.70 ± 0.27)
[200, 150, 100]	4.39 ± 0.02	702.98	23.86	(16.06 ± 0.20)
[300, 225, 150]	11.41 ± 0.03	319.48	13.79	(21.30 ± 0.17)
[400, 300, 200]	16.15 ± 0.04	113.02	6.04	(24.40 ± 0.18)
[500, 375, 250]	18.98 ± 0.04	37.96	2.25	(27.21 ± 0.16)
[600, 450, 300]	21.01 ± 0.04	12.60	0.74	(27.20 ± 0.14)
[700, 525, 350]	22.66 ± 0.04	4.53	0.23	(29.06 ± 0.15)
S2 Signal				
$[M_{\tilde{\chi}_2^0}, M_{\tilde{\chi}_1^0}]$ GeV				
[100, 50]	9.33 ± 0.18	0.14	-0.06	(7.62 ± 0.38)
[105, 13.8]	2.10 ± 0.01	61.75	3.55	(7.84 ± 0.23)
[115, 13.8]	3.17 ± 0.02	65.46	3.74	(7.73 ± 0.21)
[125, 13.8]	3.85 ± 0.02	57.49	3.32	(9.34 ± 0.21)
[135, 13.8]	4.95 ± 0.02	54.84	3.18	(10.43 ± 0.17)
[145, 13.8]	5.85 ± 0.02	49.05	2.87	(11.50 ± 0.19)
[150, 50]	3.90 ± 0.02	28.65	1.71	(12.06 ± 0.19)
[200, 100]	4.59 ± 0.02	10.70	0.62	(16.66 ± 0.20)
[250, 125]	8.53 ± 0.03	7.79	0.44	(18.28 ± 0.18)
[300, 150]	12.42 ± 0.03	5.06	0.26	(20.98 ± 0.18)
[400, 200]	17.67 ± 0.04	1.80	0.05	(24.11 ± 0.17)
[500, 250]	20.09 ± 0.04	0.58	-0.03	(27.51 ± 0.16)
[600, 300]	21.70 ± 0.04	0.19	-0.06	(27.25 ± 0.18)
[700, 350]	22.17 ± 0.04	0.06	-0.07	(27.91 ± 0.17)
Background	-	109.51	-	(28.04 ± 0.20)
$W^\pm(\rightarrow e^\pm \nu_e / \mu^\pm \nu_\mu / \tau^\pm \nu_\tau / qq') + LF$	0.00 ± 0.00	0.00	-	-
$W^\pm(\rightarrow e^\pm \nu_e / \mu^\pm \nu_\mu / \tau^\pm \nu_\tau) + HF$	0.082 ± 0.004	0.96	-	(36.93 ± 1.76)
$t\bar{t}$	0.00 ± 0.00	0.00	-	-
$t + b, t + q(+b)$	0.00 ± 0.00	0.00	-	-
$W + W, W + \gamma^*/Z, \gamma^*/Z + \gamma^*/Z$	0.283 ± 0.002	106.78	-	(26.95 ± 0.25)
$W^+ + W^- + W^\pm, W^+ + W^- + \gamma^*/Z,$ $W^\pm + \gamma^*/Z + \gamma^*/Z, \gamma^*/Z + \gamma^*/Z + \gamma^*/Z$	0.576 ± 0.004	1.77	-	(29.84 ± 0.34)
$\gamma + \gamma, \gamma + jets, \gamma + W^\pm, \gamma + Z$	0.00 ± 0.00	0.00	-	-
$\gamma^*/Z + LF$	0.00 ± 0.00	0.00	-	-
$\gamma^*/Z + HF$	0.00 ± 0.00	0.00	-	-
QCD HF	0.00 ± 0.00	0.00	-	-
QCD LF	0.00 ± 0.00	0.00	-	-

Table 23. Event selection efficiencies, event yields, signal significances and charge asymmetries for the $p + p \rightarrow \tilde{\chi}_1^\pm \tilde{\chi}_2^0 \rightarrow 3\ell^\pm + \cancel{E}_T$ analysis.

<i>Process</i>	$\alpha^{Exp} \pm \delta\alpha^{Stat}$	Z_N (σ)	$A_C^{Meas.}$ (%)	$\delta A_C^{Tot.}$ (%)	$\delta A_C^{Meas.Fit}$ (%)
<u>S1 Signal</u> [$M_{\tilde{\chi}_2^0}, M_{\tilde{\ell}^\pm}, M_{\tilde{\chi}_1^0}$] GeV					
[100, 75, 50]	$(9.98 \pm 0.26) \times 10^{-2}$	31.70	7.70	0.83	0.74
[200, 150, 100]	$(15.58 \pm 0.36) \times 10^{-2}$	23.86	16.06	0.85	0.44
[300, 225, 150]	$(34.28 \pm 0.79) \times 10^{-2}$	13.79	21.30	0.96	0.48
[400, 300, 200]	$(96.89 \pm 2.22) \times 10^{-2}$	6.04	24.40	1.29	0.58
[500, 375, 250]	$(288.49 \pm 6.61) \times 10^{-2}$	2.25	27.21	1.75	0.69
[600, 450, 300]	$(869.13 \pm 19.89) \times 10^{-2}$	0.74	27.20	1.97	0.77
[700, 525, 350]	$(241.74 \pm 5.55) \times 10^{-1}$	0.23	29.06	2.02	0.85
<u>S2 Signal</u> [$M_{\tilde{\chi}_2^0}, M_{\tilde{\chi}_1^0}$] GeV					
[100, 50]	$(78.22 \pm 6989.64) \times 10^1$	-0.06	7.62	0.88	0.59
[105, 13.8]	$(177.34 \pm 4.21) \times 10^{-2}$	3.55	7.85	1.58	0.56
[115, 13.8]	$(167.29 \pm 3.91) \times 10^{-2}$	3.74	7.73	1.55	0.52
[125, 13.8]	$(190.49 \pm 4.44) \times 10^{-2}$	3.32	9.34	1.60	0.49
[135, 13.8]	$(199.69 \pm 4.61) \times 10^{-2}$	3.18	10.43	1.62	0.46
[145, 13.8]	$(223.26 \pm 5.16) \times 10^{-2}$	2.87	11.50	1.67	0.45
[150, 50]	$(382.23 \pm 8.90) \times 10^{-2}$	1.71	12.06	1.85	0.44
[200, 100]	$(102.35 \pm 2.34) \times 10^{-1}$	0.62	16.66	2.00	0.46
[250, 125]	$(140.58 \pm 3.23) \times 10^{-1}$	0.44	18.28	2.01	0.52
[300, 150]	$(216.42 \pm 4.96) \times 10^{-1}$	0.26	20.98	2.02	0.60
[400, 200]	$(608.39 \pm 13.89) \times 10^{-1}$	0.05	24.11	2.03	0.74
[500, 250]	$(18.88 \pm 0.43) \times 10^{-5}$	-0.03	27.51	2.03	0.86
[600, 300]	$(57.64 \pm 1.32) \times 10^{-5}$	-0.06	27.25	2.03	0.96
[700, 350]	$(182.52 \pm 4.17) \times 10^{-5}$	-0.07	27.91	2.03	1.04

Table 24. Noise to signal ratio, signal statistical significance, and expected and measured integral charge asymmetries for the S1 and S2 signal samples for the $p + p \rightarrow \tilde{\chi}_1^\pm \tilde{\chi}_2^0 \rightarrow 3\ell^\pm + \cancel{E}_T$ analysis.

$M_{\tilde{\chi}_1^\pm} + M_{\tilde{\chi}_2^0}$ Input Mass (GeV)	$A_C^{Meas.} \pm \delta A_C^{Meas.Fit}$ (%)	$M_{\tilde{\chi}_1^\pm} + M_{\tilde{\chi}_2^0}$ Measured Mass (GeV)
200.	7.70 ± 0.74	$200.37^{+11.51}_{-10.78}$
400.	16.06 ± 0.44	$390.18^{+14.83}_{-14.21}$
600.	21.30 ± 0.48	$617.94^{+27.70}_{-26.34}$
800.	24.40 ± 0.58	$824.61^{+46.98}_{-44.09}$
1000.	27.21 ± 0.69	$1083.15^{+76.95}_{-71.18}$
1200.	27.20 ± 0.77	$1082.08^{+86.18}_{-78.99}$
1400.	29.06 ± 0.85	$1304.01^{+118.38}_{-107.31}$

Table 25. Measured $A_C(S)$ of the S1 signal samples with their full experimental uncertainty. Indirect mass measurement and their full experimental uncertainty as a function of the signal sample.

Forced Parameter	Fit $\chi^2/Ndof$	Fit Y-Intercept	Fit Slope
Slope	5.328/6	-1.67 ± 8.26	1.0 ± 0.0
Y-Intercept	5.260/6	0.0 ± 0.0	0.9933 ± 0.0203

Table 26. Closure tests with a forced fit parameter for the S1 signal samples.

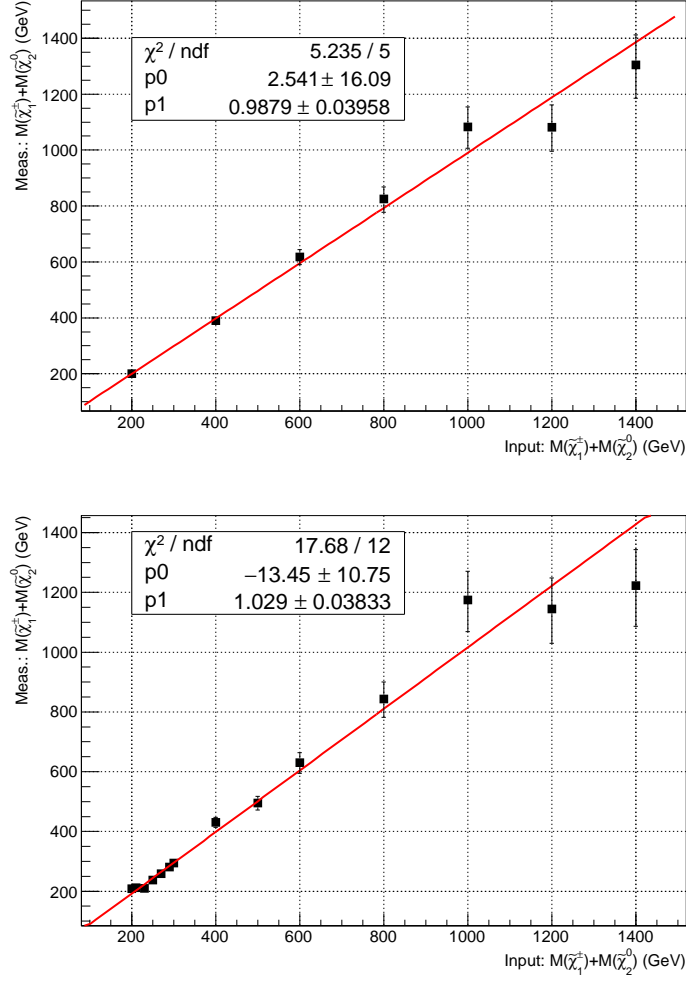


Figure 18. Closure test of the indirect measurement of $M_{\tilde{\chi}_1^\pm} + M_{\tilde{\chi}_2^0}$ for the S1 (top) and S2 (bottom) signal samples with only experimental uncertainties.

$M_{\tilde{\chi}_1^\pm} + M_{\tilde{\chi}_2^0}$ Input Mass (GeV)	$A_C^{Meas.} \pm \delta A_C^{Meas.Fit}$ (%)	$M_{\tilde{\chi}_1^\pm} + M_{\tilde{\chi}_2^0}$ Measured Mass (GeV)
200.	7.62 ± 0.59	$208.34^{+9.51}_{-9.01}$
210.	7.85 ± 0.56	$211.99^{+9.20}_{-8.75}$
230.	7.73 ± 0.52	$210.08^{+8.43}_{-8.05}$
250.	9.34 ± 0.49	$237.72^{+9.01}_{-8.97}$
270.	10.43 ± 0.46	$258.55^{+9.52}_{-9.13}$
290.	11.50 ± 0.45	$281.34^{+10.29}_{-9.86}$
300.	12.06 ± 0.44	$294.21^{+10.60}_{-10.17}$
400.	16.66 ± 0.46	$430.69^{+17.35}_{-16.57}$
500.	18.28 ± 0.52	$495.51^{+23.17}_{-21.97}$
600.	20.98 ± 0.60	$630.50^{+35.51}_{-33.34}$
800.	24.11 ± 0.74	$843.48^{+61.79}_{-57.00}$
1000.	27.51 ± 0.86	$1174.45^{+105.82}_{-95.96}$
1200.	27.25 ± 0.96	$1144.45^{+115.34}_{-103.44}$
1400.	27.91 ± 1.04	$1222.38^{+135.40}_{-120.22}$

Table 27. Measured $A_C(S)$ of the S2 signal samples with their full experimental uncertainty. Indirect mass measurement and their full experimental uncertainty as a function of the signal sample.

Here again the fit indicates, within the uncertainties, that the indirect mass measurement is linear and unbiased. The checks, forcing the parameters of the fit functions, tend to confirm these indications, as presented in table 28.

Forced Parameter	Fit $\chi^2/Ndof$	Fit Y-Intercept	Fit Slope
Slope	18.27/13	-5.601 ± 3.349	1.0 ± 0.0
Y-Intercept	19.25/13	0.0 ± 0.0	0.9838 ± 0.0120

Table 28. Closure tests with a forced fit parameter for the S2 signal samples.

3.4 Final Result for MRST2007lomod

3.4.1 Final Result for the S1 Signal

Meas. $M_{\tilde{\chi}_1^\pm} + M_{\tilde{\chi}_2^0}$ (GeV)	Expt. Uncert. (GeV)	Theor. Uncert. (GeV)	Total Uncert. (GeV)
200.37	+11.51 -10.78	+0.90 -0.90	+11.55 -10.82
390.18	+14.83 -14.21	+1.07 -1.12	+14.87 -14.25
617.94	+27.70 -26.34	+2.15 -2.24	+27.78 -26.44
824.61	+46.98 -44.09	+2.69 -2.70	+47.06 -44.17
1083.15	+76.95 -71.18	+2.13 -2.24	+76.98 -71.22
1082.08	+86.18 -78.99	+2.16 -2.24	+86.21 -79.02
1304.01	+118.38 -107.31	+5.76 -5.38	+118.52 -107.44

Table 29. Final results for the S1 samples with experimental and theoretical uncertainties.

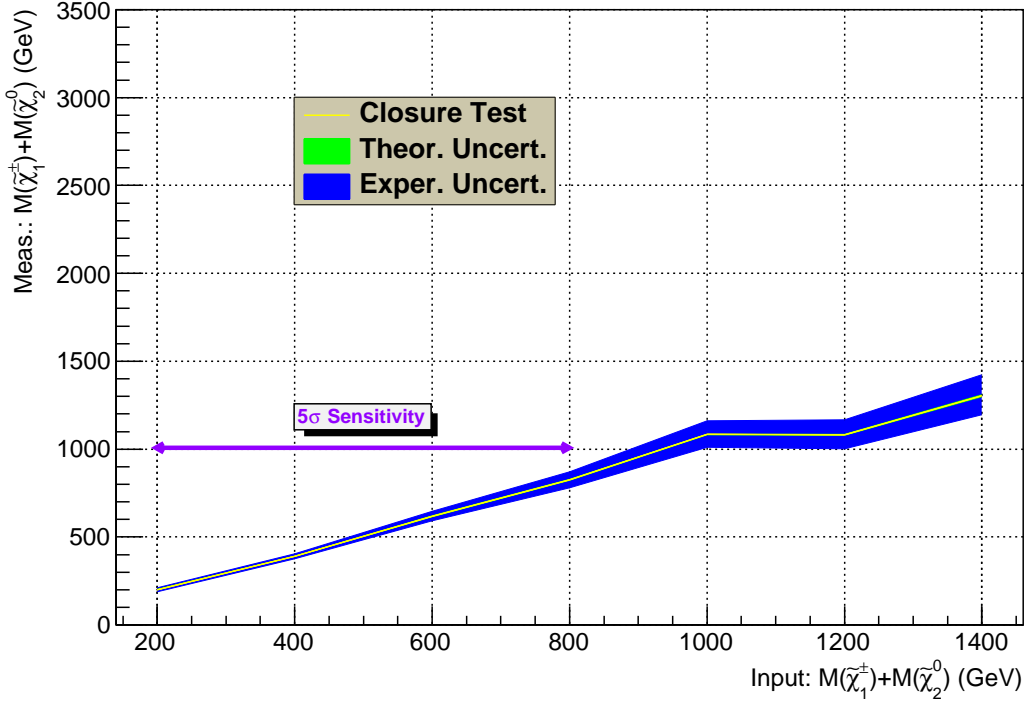


Figure 19. Closure test of the indirect measurement of $M_{\tilde{\chi}_1^\pm} + M_{\tilde{\chi}_2^0}$ for the S1 signal samples with both theoretical and experimental uncertainties. The sub-range with a signal sensitivity of 5σ is highlighted.

For the S1 sub-samples with a signal significance in excess of 5σ , the indirect measurements

of $M_{\tilde{\chi}_1^\pm} + M_{\tilde{\chi}_2^0}$ are performed with an overall accuracy better than 6% for input masses $M_{\tilde{\chi}_2^0} = M_{\tilde{\chi}_1^\pm}$ in the [100,300] GeV interval, and better than 10% for $M_{\tilde{\chi}_2^0} = M_{\tilde{\chi}_1^\pm} \geq 400$ GeV. This is reported in table 29 and displayed in figure 19.

3.4.2 Final Result for the S2 Signal

Meas. $M_{\tilde{\chi}_1^\pm} + M_{\tilde{\chi}_2^0}$ (GeV)	Expt. Uncert. (GeV)	Theor. Uncert. (GeV)	Total Uncert. (GeV)
208.34	+9.51 -9.01	+0.70 -0.76	+9.54 -9.04
211.99	+9.20 -8.75	+0.66 -0.69	+9.22 -8.78
210.08	+8.43 -8.05	+0.55 -0.76	+8.45 -8.09
237.72	+9.01 -8.97	+0.61 -0.64	+9.03 -8.99
258.55	+9.52 -9.13	+0.65 -0.76	+9.54 -9.16
281.34	+10.29 -9.86	+0.77 -0.86	+10.32 -9.90
294.21	+10.60 -10.17	+0.86 -0.87	+10.63 -10.21
430.69	+17.35 -16.57	+1.34 -1.44	+17.40 -16.63
495.51	+23.17 -21.97	+1.37 -1.46	+23.21 -22.02
630.50	+35.51 -33.34	+2.12 -2.24	+35.57 -33.42
843.48	+61.79 -57.00	+2.57 -2.74	+61.84 -57.07
1174.45	+105.82 -95.96	+2.44 -2.47	+105.85 -95.99
1144.45	+115.34 -103.44	+2.40 -2.53	+115.36 -103.47
1222.38	+135.40 -120.22	+3.38 -3.34	+135.44 -120.27

Table 30. Final results for the S2 samples with experimental and theoretical uncertainties.

For the S2 sub-samples with a signal significance in excess of 3σ , the indirect measurements of $M_{\tilde{\chi}_1^\pm} + M_{\tilde{\chi}_2^0}$ are performed with an overall accuracy better than 4.5% for respective input masses $M_{\tilde{\chi}_2^0} = M_{\tilde{\chi}_1^\pm}$ in the [105,145] GeV interval and better than 11.1% for considered masses outside this interval. This is reported in table 30 and displayed in figure 20.

3.5 Summary of the $M_{\tilde{\chi}_1^\pm} + M_{\tilde{\chi}_2^0}$ Measurements and their Accuracy

We sum up the indirect mass measurements of $M_{\tilde{\chi}_1^\pm} + M_{\tilde{\chi}_2^0}$ extracted from the integral charge asymmetry of the $\tilde{\chi}_1^\pm + \tilde{\chi}_2^0 \rightarrow 3\ell^\pm + \cancel{E}_T$ inclusive process within tables 31 (S1 signal) and 32 (S2 signal).

For the S1 signal at LO, this new method enables to get an accuracy better than 6% for the range with 5σ sensitivity to the signal and better than 10% elsewhere. Whereas for the S2 signal at LO, we get an accuracy better than 4.5% for the range with 3σ sensitivity to the signal and better than 11.2% elsewhere. All these indirect measurements are statistically compatible with the total uncertainty of the method.

One should bear in mind however that these results do not account for the dominant theoretical uncertainty ($\delta(A_C)_{PDF}$).

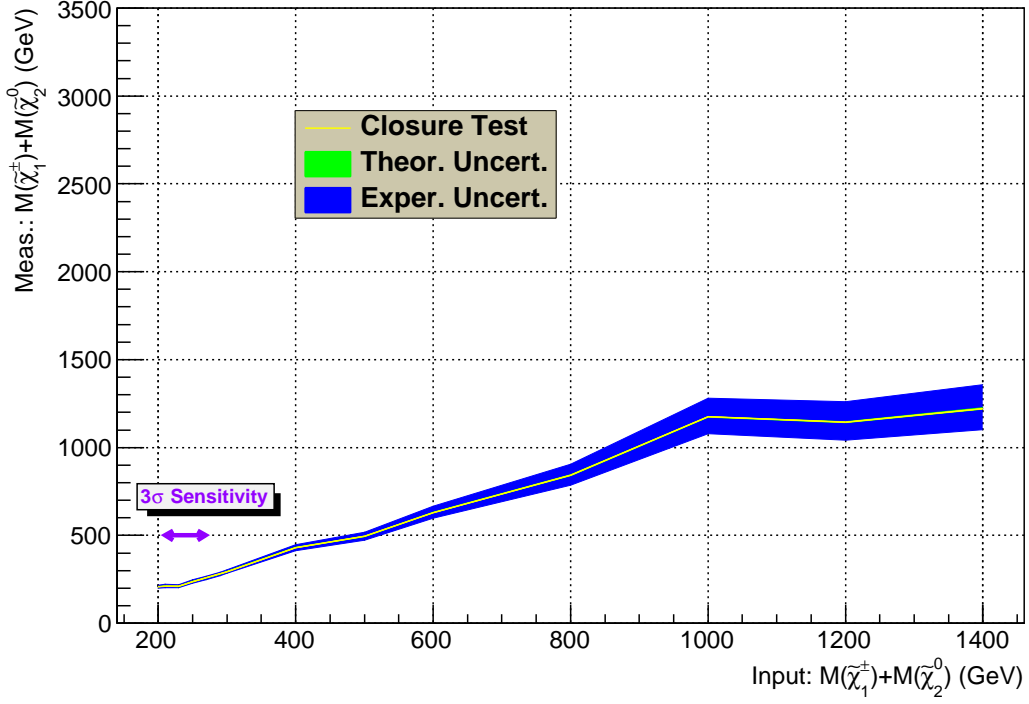


Figure 20. Closure test of the indirect measurement of $M_{\tilde{\chi}_1^\pm} + M_{\tilde{\chi}_2^0}$ for the S2 signal samples with both theoretical and experimental uncertainties. The sub-range with a signal sensitivity of 3σ is highlighted.

S1 Signal Input $M_{\tilde{\chi}_1^\pm} + M_{\tilde{\chi}_2^0}$ (GeV)	Figures of Merit		
	1.	2.	3.
	$\frac{\delta M_{\tilde{\chi}_1^\pm \tilde{\chi}_2^0}^{Fit}}{M_{\tilde{\chi}_1^\pm \tilde{\chi}_2^0}^{Fit}}$	$\frac{(M_{\tilde{\chi}_1^\pm \tilde{\chi}_2^0}^{Fit} - M_{\tilde{\chi}_1^\pm \tilde{\chi}_2^0}^{True})}{M_{\tilde{\chi}_1^\pm \tilde{\chi}_2^0}^{True}}$	$\frac{(M_{\tilde{\chi}_1^\pm \tilde{\chi}_2^0}^{Fit} - M_{\tilde{\chi}_1^\pm \tilde{\chi}_2^0}^{True})}{\delta M_{\tilde{\chi}_1^\pm \tilde{\chi}_2^0}^{Fit}}$
200.	5.8%	+0.2%	+0.03 σ
400.	3.8%	-2.5%	-0.7 σ
600.	4.5%	+3.0%	+0.7 σ
800.	5.7%	+3.1%	+0.5 σ
1000.	7.1%	+8.3%	+1.1 σ
1200.	8.0%	-9.8%	-1.4 σ
1400.	9.1%	-6.9%	-0.8 σ

Table 31. Summary of the indirect mass measurements of $M_{\tilde{\chi}_1^\pm} + M_{\tilde{\chi}_2^0}$ extracted from the integral charge asymmetry of the S1 signal samples. Different figures of merit of the accuracy of these measurements are presented.

S2 Signal Input $M_{\tilde{\chi}_1^\pm} + M_{\tilde{\chi}_2^0}$ (GeV)	Figures of Merit		
	1.	2.	3.
	$\frac{\delta M^{Fit}}{\tilde{\chi}_1^\pm \tilde{\chi}_2^0}$	$\frac{(M^{Fit} - M^{True})}{\tilde{\chi}_1^\pm \tilde{\chi}_2^0}$	$\frac{(M^{Fit} - M^{True})}{\tilde{\chi}_1^\pm \tilde{\chi}_2^0}$
	$\frac{M^{Fit}}{\tilde{\chi}_1^\pm \tilde{\chi}_2^0}$	$\frac{M^{True}}{\tilde{\chi}_1^\pm \tilde{\chi}_2^0}$	$\frac{\delta M^{Fit}}{\tilde{\chi}_1^\pm \tilde{\chi}_2^0}$
200.	4.6%	+4.2%	+0.9 σ
210.	4.4%	+1.0%	+0.2 σ
230.	4.0%	-8.7%	-2.4 σ
250.	3.8%	-4.9%	-1.4 σ
270.	3.7%	-4.2%	-1.2 σ
290.	3.7%	-3.0%	-0.8 σ
300.	3.6%	-1.9%	-0.5 σ
400.	4.0%	+7.7%	+1.8 σ
500.	4.7%	-0.9%	-0.2 σ
600.	5.6%	+5.1%	+0.9 σ
800.	7.3%	+5.4%	+0.7 σ
1000.	9.0%	+17.5%	+1.7 σ
1200.	10.1%	-4.6%	-0.5 σ
1400.	11.1%	-12.7%	-1.3 σ

Table 32. Summary of the indirect mass measurements of $M_{\tilde{\chi}_1^\pm} + M_{\tilde{\chi}_2^0}$ extracted from the integral charge asymmetry of the S2 signal samples. Different figures of merit of the accuracy of these measurements are presented.

3.6 Comparison with Other Mass Measurement Methods

3.6.1 Dilepton Mass Edge

In this sub-section, we'll compare the *ICA* (Integral Charge Asymmetry) indirect mass measurement technique with two other direct mass measurement techniques.

But before entering this topic, let us mention the issue of the combinatorics within the trilepton search topology we've chosen. For our signal, resolving this combinatorics consists in matching the correct dilepton to its parent $\tilde{\chi}_2^0$ whilst associating the third lepton to its parent $\tilde{\chi}_1^\pm$. The $\tilde{\chi}_2^0$ leptonic decay yields two leptons with opposite-signs (OS) and same flavours (SF). In events with mixed flavours ($e^+e^-\mu^\pm$ or $\mu^+\mu^-e^\pm$), the correct assignment is obvious: the dilepton of SF comes from the $\tilde{\chi}_2^0$ and the single lepton with the other flavour comes from the $\tilde{\chi}_1^\pm$. However in order to exploit the full signal statistics, one also needs to resolve this combinatorics in tri-electron and tri-muon events. For each of these event topology involving a single flavour, there are always two combinations of OS dileptons and one combination of same-sign (SS) dilepton. Therefore we adopt a statistical solution to lift the combinatorics. In the calculation of any physical observable, for each $3e^\pm$ or $3\mu^\pm$ event, we fill the corresponding histogram with two entries from the two OS dileptons with a weight of +1 and with one entry from the single SS dilepton with a weight of -1. This systematically subtracts from the observable histogram the wrong combination which associates a lepton from the $\tilde{\chi}_1^\pm$ decay with one of the $\tilde{\chi}_2^0$ decay.

3.6.1. a. Experimental Observable

The fact that the OS-SF dilepton coming from the second neutralino decay has an edge in its invariant mass was noted long ago in [58]. It has been used extensively in the litterature [69][70] [71][72], including in a few reviews like [76] and in references therein.

For the S1 signal, we have the following mass hierarchy $M_{\tilde{\chi}_2^0} = M_{\tilde{\chi}_1^\pm} > M_{\tilde{\ell}^\pm} > M_{\tilde{\chi}_1^0}$ and we consider $\tilde{\chi}_2^0$ and $\tilde{\chi}_1^\pm$ two-body decays proceeding through an intermediate slepton. In this case, the edge is given by:

$$M_{\ell^\pm\ell^\mp}^{Max} = M_{\tilde{\chi}_2^0} \times \sqrt{\left(1 - \frac{M_{\tilde{\ell}^\pm}^2}{M_{\tilde{\chi}_2^0}^2}\right) \left(1 - \frac{M_{\tilde{\chi}_1^0}^2}{M_{\tilde{\ell}^\pm}^2}\right)} \quad (3.2)$$

For the S2 signal, we have the following mass hierarchy $M_{\tilde{\chi}_2^0} = M_{\tilde{\chi}_1^\pm} > M_{\tilde{\chi}_1^0}$ and we consider $\tilde{\chi}_2^0$ and $\tilde{\chi}_1^\pm$ decays proceeding through W^\pm and Z bosons. In these cases, the edge is given by:

$$M_{\ell^\pm\ell^\mp}^{Max} = (M_{\tilde{\chi}_2^0} - M_{\tilde{\chi}_1^0}) < M_Z \quad (3.3)$$

for a $\tilde{\chi}_2^0$ three-body decay proceeding through an off-shell Z^* (S2a), and by

$$M_{\ell^\pm\ell^\mp}^{Max} = (M_{\tilde{\chi}_2^0} - M_{\tilde{\chi}_1^0}) \geq M_Z \quad (3.4)$$

for a $\tilde{\chi}_2^0$ two-body decay proceeding through an on-shell Z (S2b).

In light of these formulae, we see that the mass reconstruction capabilities of this method that we'll call *DileME*, for "Dilepton Mass Edge", regard exclusively the reconstruction of mass differences.

The main systematic uncertainties of the *DileME* method come from the lepton energy scales. These are known to a 0.05% accuracy in the ATLAS experiment at the LHC Run1, both for the electrons [73] and the muons [74]. Since the dilepton invariant mass is:

$$M_{\ell_1^\pm \ell_2^\mp}^2 = 2E_{\ell_1^\pm} E_{\ell_2^\mp} (1 - \cos \alpha_{1,2}) \quad (3.5)$$

The index with values 1 or 2 refers to either of the two OS-SF leptons from the $\tilde{\chi}_2^0$ decay, and $\alpha_{1,2}$ is the angle in space between their flight directions. Neglecting the uncertainty on the angle, the relative uncertainty on $M_{\ell^\pm \ell^\mp}$ writes:

$$\frac{\delta M_{\ell^\pm \ell^\mp}}{M_{\ell^\pm \ell^\mp}} = \frac{\delta E_{\ell^\pm}}{E_{\ell^\pm}} \quad (3.6)$$

3.6.1. b. Theoretical Shape

For unpolarized $\tilde{\chi}_2^0$ and for their two-body decays, the theoretical shape of the dilepton invariant mass is known [66] to be:

$$\frac{1}{\Gamma} \frac{d\Gamma}{dM_{\ell^\pm \ell^\mp}} = 2M_{\ell^\pm \ell^\mp} \quad (3.7)$$

As seen in subsection 3.2.2, the main background process in the $\tilde{\chi}_1^\pm + \tilde{\chi}_2^0 \rightarrow 3\ell^\pm + \cancel{E}_T$ analysis is the $W^\pm + \gamma^*/Z^0 \rightarrow 3\ell^\pm + \cancel{E}_T$ process, which constitutes an irreducible background. The OS-SF dilepton coming from the γ^*/Z^0 decay forms a peak centered around M_Z . Therefore, we model the invariant mass distribution of events surviving our selection using the following 6-parameters functional form:

$$M^{Fit}(x) = \frac{C_3}{2\pi} \times \frac{C_5}{(x - C_4)^2 + \frac{C_5^2}{4}} + \begin{cases} 2C_1 \times \frac{x}{C_0^2}, & \text{for } x < C_0; \text{ and} \\ 0, & \text{for } x > C_0 \end{cases} \quad (3.8)$$

In order to account for the detector finite resolution, we convoluted the previous functional form with a gaussian distribution centered on zero and with an RMS set to C_2 . The other parameters represent:

- C_0 : $M_{\ell^\pm \ell^\mp}^{Max}$, i.e. the position of the dilepton edge;
- C_1 : N_S^{Exp} , i.e. the number of expected signal events under the triangle;
- C_3 : N_B^{Exp} , i.e. the number of expected background events under the Z peak;
- C_4 : M_Z , i.e. the position of the Z peak; and,
- C_5 : Γ_Z , i.e. the width of the Z peak.

For the S2b signal samples, we expect $N_S^{Exp} + N_B^{Exp}$ events under the Z peak.

After a few trials we find it is sufficient to use the same triangle distribution to describe both the two-body and the three-body $\tilde{\chi}_2^0$ decay in these fits.

The results of these fits are presented in tables 33 and 34. The plots 21 and 22 illustrate a few of these fits. Obviously the highest $M_{\tilde{\chi}_2^0}$ mass hypotheses unable any measurement

Process	Theor. $M_{\ell^+\ell^-}^{Edge}$ (GeV)	Meas. $M_{\ell^+\ell^-}^{Edge}$ (GeV)	Fit χ^2/N_{dof}
Signal S1 [$M_{\tilde{\chi}_2^0}, M_{\tilde{\ell}^\pm}, M_{\tilde{\chi}_1^0}$] GeV			
[100, 75, 50]	49.301	$49.000 \pm 0.000(stat) \pm 0.025(syst)$	1.010
[200, 150, 100]	98.601	$97.000 \pm 0.000(stat) \pm 0.049(syst)$	0.263
[300, 225, 150]	147.902	$147.8 \pm 4.8(stat) \pm 0.074(syst)$	0.120
[400, 300, 200]	197.203	$196.500 \pm 0.000(stat) \pm 0.098(syst)$	0.067
[500, 375, 250]	246.503	$246.93 \pm 0.08(stat) \pm 0.123(syst)$	0.093
[600, 450, 300]	295.804	$300.8 \pm 0.7(stat) \pm 0.150(syst)$	0.097
[700, 525, 350]	345.105	—	—

Table 33. Dilepton mass edge measurements for the S1 samples.

Process	Theor. $M_{\ell^+\ell^-}^{Edge}$ (GeV)	Meas. $M_{\ell^+\ell^-}^{Edge}$ (GeV)	Fit χ^2/N_{dof}
Signal S2 [$M_{\tilde{\chi}_2^0}, M_{\tilde{\chi}_1^0}$] GeV			
[100, 50]	50.0	$52.35 \pm 0.22(stat) \pm 0.026(syst)$	0.274
[105, 13.8]	91.2	$91.16 \pm 7.52(stat) \pm 0.046(syst)$	0.172
[115, 13.8]	101.2	$90.28 \pm 6.62(stat) \pm 0.045(syst)$	0.154
[125, 13.8]	111.2	$88.16 \pm 3.33(stat) \pm 0.040(syst)$	0.132
[135, 13.8]	121.2	$90.13 \pm 6.54(stat) \pm 0.045(syst)$	0.116
[145, 13.8]	131.2	$88.29 \pm 6.03(stat) \pm 0.044(syst)$	0.125
[150, 50]	100.0	$99.54 \pm 4.16(stat) \pm 0.050(syst)$	0.230
[200, 100]	100.0	$91.92 \pm 1.99(stat) \pm 0.046(syst)$	0.125
[250, 125]	125.0	$91.27 \pm 1.97(stat) \pm 0.046(syst)$	0.154
[300, 150]	150.0	$91.17 \pm 0.94(stat) \pm 0.046(syst)$	0.126
[400, 200]	200.0	—	—
[500, 250]	250.0	—	—
[600, 300]	300.0	—	—
[700, 350]	350.0	—	—

Table 34. Dilepton mass edge measurements for the S2 samples.

of the dilepton invariant mass edge because of their unsufficient signal-to-noise ratio. This situation is met for $M_{\tilde{\chi}_2^0} \geq 700$ GeV for the S1 samples and $M_{\tilde{\chi}_2^0} \geq 400$ GeV for the S2 samples.

First of all we notice, that *ICA* and *DileME* methods do not give access to the same informations: $M_{\tilde{\chi}_2^0} + M_{\tilde{\chi}_1^0}$, versus $M_{\tilde{\chi}_2^0} - M_{\tilde{\chi}_1^0}$ or $M_{\tilde{\chi}_2^0} \times \sqrt{\left(1 - \frac{M_{\tilde{\ell}^\pm}^2}{M_{\tilde{\chi}_2^0}^2}\right) \left(1 - \frac{M_{\tilde{\chi}_1^0}^2}{M_{\tilde{\ell}^\pm}^2}\right)}$, respectively.

We notice that the *DileME* method is very accurate: better than 3.5% (and most often better than 1%) for the S1 samples, and better than 0.5% for the S2a sample. However, for the S2b signal samples, it fails to extract any sensible informations about the mass difference because of the resonant mode of the $\tilde{\chi}_2^0$ decay. For the sample (105, 13.8) S2b sample, the correct mass difference is found by chance, whereas for the other S2b samples, the *DileME* method systematically provides a wrong answer: $M_{\tilde{\chi}_2^0} - M_{\tilde{\chi}_1^0} = M_Z$. In regard of these observations, we conclude that the *ICA* and *DileME* methods complement very well each other.

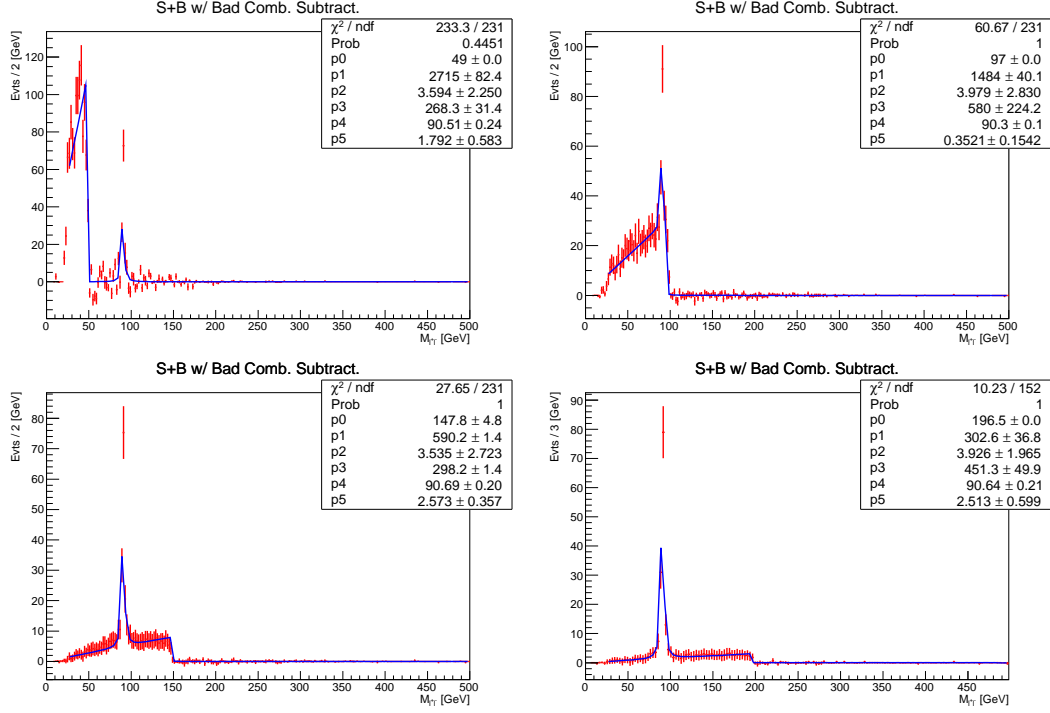


Figure 21. A few examples of *DileME* measurements on the S1 samples for $100 \leq M_{\tilde{\chi}_2^0} \leq 400$ GeV

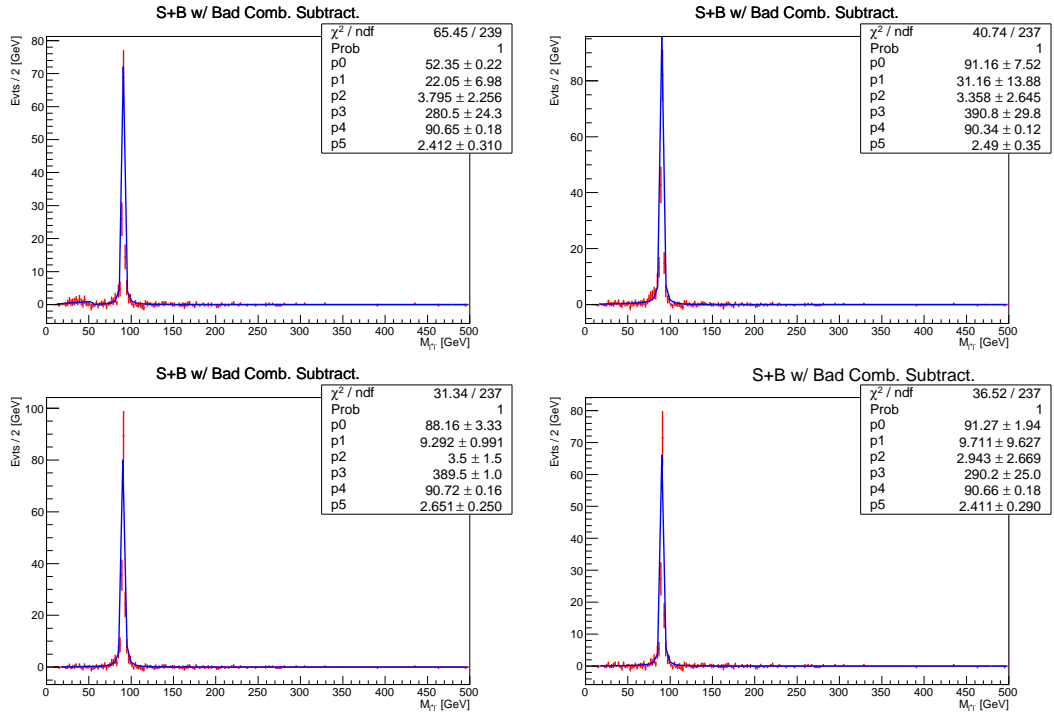


Figure 22. A few examples of *DileME* measurements on the S2 samples for $100 \leq M_{\tilde{\chi}_2^0} \leq 250$ GeV

3.6.2 Stranverse Mass End-Point

3.6.2. a. Experimental Observable

Let's consider an event where two particles (X) and (Y) are produced. Let's consider they both undergo decay chains, both ending up by the same invisible particle, denoted χ , while emitting some visible energy in each hemispheres (A) and (B): $E^{vis(A)}$ and $E^{vis(B)}$. For an hypothesized mass of χ , M_χ^{trial} , the event stranverse mass M_{T2} is defined as:

$$M_{T2}(vis^{(A)}, vis^{(B)} | M_\chi^{trial}) = \min_{\vec{E}_T^{(A)} + \vec{E}_T^{(B)} = \vec{E}_T} \left\{ \max[M_T(\vec{p}_T^{vis(A)}, \vec{E}_T^{(A)}); M_T(\vec{p}_T^{vis(B)}, \vec{E}_T^{(B)})] \right\} \quad (3.9)$$

where

$$M_T^{2(A)} = M^{2(A)} + M^{2(\chi_A)} + 2[E_T^{(A)} \cdot E_T^{(\chi_A)} - \vec{p}_T^{(A)} \cdot \vec{p}_T^{(\chi_A)}] \quad (3.10)$$

, and

$$E_T^2 = M^2 + p_T^2 \quad (3.11)$$

The stranverse mass has two important properties. On the one hand, it's very effective to discriminate R-parity conserved SUSY signals from their SM background processes. On the other hand it enables to measure the mass of the parent particles (X) and (Y) and of children particle (χ) and for this second purpose, we'll denote this method $MT2$ in the rest of this article.

Regarding the signal and background discrimination described in section 3.2, we arbitrarily chose the following assignment:

- $\ell_1^\pm \leftrightarrow$ visible energy (A),
- $\ell_2^\pm \leftrightarrow$ visible energy (B),
- $\ell_3^\pm \leftrightarrow$ downstream additional visible particle,

where the index $i = 1, 2, 3$ refers to the decreasing p_T of the leptons, and we set $M_\chi^{trial} = 0$ GeV. This choice does not accurately reflect the actual kinematics of our signal samples, but it is sufficient to provide a good and simple signal to background discrimination applicable to all of them.

On the contrary, in the current section, in order to assess the mass measurement capability of the $MT2$ method we have to properly assign the OS-SF dilepton to the $\tilde{\chi}_2^0$ decay, say into the visible energy (A), and the additional lepton to the $\tilde{\chi}_1^\pm$ decay into the visible energy (B). This precise assignment is done via the solution we adopted to solve the trilepton combinatorics which is presented in the preamble of the current section.

The main systematic uncertainties for the $MT2$ method come from the reconstruction of the different objects in our search topology. As inferred from [75], we consider as sources of uncertainty: the trigger, the reconstruction, the identification, the energy resolution and the isolation for both the electrons and the muons. The resulting uncertainties are 4.6% (e^\pm) and 1.1% (μ^\pm), respectively. These changes in the electrons and muons kinematics are propagated onto a corrected missing transverse energy E_T^{Corr} . Then, the impact of the

uncertainties of the calorimeter cluster energy scale, of the jet energy scale and the jet energy resolution, and of the pile-up on the E_T , are also summed in quadrature, amounting to an uncertainty of 0.8% with which the E_T^{Corr} is smeared. We input the smeared E_T^{Corr} and the smeared lepton kinematics into the calculation of a smeared $M_{T2}^{Smeared}$. Finally, the systematic uncertainty on M_{T2} is taken as the absolute value of the relative difference between the nominal M_{T2} and $M_{T2}^{Smeared}$:

$$\frac{\delta M_{T2}}{M_{T2}} = \frac{|M_{T2} - M_{T2}^{Smeared}|}{M_{T2}}. \quad (3.12)$$

This procedure is re-iterated for each value of M_χ^{trial} , as reported in table 35.

M_χ^{trial} (GeV)	$\frac{\delta M_{T2}}{M_{T2}}$ (%)
0.	1.86
13.8	1.80
50.	1.47
100.	1.10
125.	1.02
150.	0.97
200.	0.90
250.	0.85
300.	0.83
350.	0.81

Table 35. Systematic uncertainty on M_{T2} for different M_χ^{trial} .

3.6.2. b. Theoretical End-Points

In order to measure the end-points (M_{T2}^{Max}) of the M_{T2} distributions we use either descending step functions or continuous but not derivable linear functions, depending on the position of this end-points with respect to the remaining background.

The positions of these end-points depend on the hypothesized value of M_χ^{trial} and have a kink at $M_\chi^{trial} = M_{\tilde{\chi}_1^0}$ [78]. Therefore, they are described by continuous functions (yet not derivable at the kink position): one, that we'll denote f_{down} for $M_\chi^{trial} < M_{\tilde{\chi}_1^0}$ and another one, denoted f_{up} for $M_\chi^{trial} > M_{\tilde{\chi}_1^0}$.

For two-body decays, the f_{down} and f_{up} functions are:

$$f_{down}^{2-body} = M_{T2}^{Max} \left(\ell_{(A)}^\pm, \ell_{(B)}^\pm \ell_{(B)}^\mp | M_\chi^{trial} < M_{\tilde{\chi}_1^0} \right) = \left(\frac{M_{\tilde{\chi}_2^0}^2 + M_{\tilde{\ell}^\pm}^2 - M_{\tilde{\chi}_1^0}^2}{2M_{\tilde{\chi}_2^0}} \right) + \sqrt{\left(\frac{M_{\tilde{\chi}_2^0}^2 - M_{\tilde{\ell}^\pm}^2 + M_{\tilde{\chi}_1^0}^2}{2M_{\tilde{\chi}_2^0}} \right)^2 + [(M_\chi^{trial})^2 - M_{\tilde{\chi}_1^0}^2]} \quad (3.13)$$

and,

$$f_{up}^{2-body} = M_{T2}^{Max} \left(\ell_{(A)}^{\pm}, \ell_{(B)}^{\mp} | M_{\chi}^{trial} > M_{\tilde{\chi}_1^0} \right) = \frac{M_{\tilde{\chi}_2^0}}{2} \left(\left(1 - \frac{M_{\tilde{\ell}^{\pm}}^2}{M_{\tilde{\chi}_2^0}^2} \right) + \left(1 - \frac{M_{\tilde{\chi}_1^0}^2}{M_{\tilde{\ell}^{\pm}}^2} \right) \right) + \sqrt{\left[\frac{M_{\tilde{\chi}_2^0}}{2} \left(\left(1 - \frac{M_{\tilde{\ell}^{\pm}}^2}{M_{\tilde{\chi}_2^0}^2} \right) - \left(1 - \frac{M_{\tilde{\chi}_1^0}^2}{M_{\tilde{\ell}^{\pm}}^2} \right) \right) \right]^2 + (M_{\chi}^{trial})^2} \quad (3.14)$$

Whereas, for three-body decays, the f_{down} and f_{up} functions are:

$$f_{down}^{3-body} = M_{T2}^{Max} \left(\ell_{(A)}^{\pm}, \ell_{(B)}^{\mp} | M_{\chi}^{trial} < M_{\tilde{\chi}_1^0} \right) = \left(\frac{M_{\tilde{\chi}_2^0}^2 - M_{\tilde{\chi}_1^0}^2}{2M_{\tilde{\chi}_2^0}} \right) + \sqrt{\left(\frac{M_{\tilde{\chi}_2^0}^2 - M_{\tilde{\chi}_1^0}^2}{2M_{\tilde{\chi}_2^0}} \right)^2 + (M_{\chi}^{trial})^2} \quad (3.15)$$

and,

$$f_{up}^{3-body} = M_{T2}^{Max} \left(\ell_{(A)}^{\pm}, \ell_{(B)}^{\mp} | M_{\chi}^{trial} > M_{\tilde{\chi}_1^0} \right) = (M_{\tilde{\chi}_2^0} - M_{\tilde{\chi}_1^0}) + M_{\chi}^{trial} \quad (3.16)$$

It's important to note, that for f_{down}^{2-body} , small values of M_{χ}^{trial} are not always permitted. In the particular for our simplified models, we have the following relations: $M_{\tilde{\chi}_2^0} = 2M_{\tilde{\chi}_1^0}$, and for the S1 samples, $M_{\tilde{\ell}^{\pm}} = \frac{3}{2}M_{\tilde{\chi}_1^0}$. Therefore we need to keep $M_{\chi}^{trial} \geq \sqrt{\frac{135}{256}} \times M_{\tilde{\chi}_1^0}$ in order for f_{down}^{2-body} to be defined.

For the $MT2$ method, we need to perform two series of fits. We start with primary fits to the M_{T2} distributions for each signal sample so as to measure their M_{T2}^{Max} . Then we proceed with the secondary fits for each signal sample. The latter use as inputs the different M_{T2}^{Max} values obtained for each M_{χ}^{trial} hypothesis and they enable simultaneously to measure the mass of the parent particle, here $M_{\tilde{\chi}_2^0} = M_{\tilde{\chi}_1^{\pm}}$, of the end daughter particle $M_{\tilde{\chi}_1^0}$ and, for the S1 samples, the mass of the intermediate particle, $M_{\tilde{\ell}^{\pm}}$. The 2-body functional forms are utilized to fit the S1 samples and the 3-body ones are utilized to fit the S2 samples. Note that these functional forms also provide the prior knowledge of the M_{T2}^{Max} for each signal hypothesis which serve as starting points in the minimization process of the primary fits. Here are a few important observations that justify our strategy for the primary fits:

- the M_{T2} distribution of the remaining background events cluster into a Z peak which is located at $M_Z + M_{\chi}^{trial}$,
- the M_{T2} distribution of the S2b samples also cluster into a Z peak which is located at $M_Z + M_{\chi}^{trial}$ and which may either be truncated or exhibit an asymmetric shoulder,
- S1 samples: without an analytical description of the full M_{T2} distribution, we just fit the M_{T2} falling edge.

This leads us to use similar functional forms as for the dilepton mass distributions for the primary fits, but with 8 parameters:

$$M^{Fit}(x) = \frac{C_5}{2\pi} \times \frac{C_7}{(x - C_6)^2 + \frac{C_7^2}{4}} + \begin{cases} C_1 \times (x - C_0) + C_2, & \text{for } x < C_0; \text{ and} \\ C_3 \times (x - C_0) + C_2, & \text{for } x > C_0 \end{cases} \quad (3.17)$$

In order to account for the detector finite resolution, we convoluted the previous functional form with a gaussian distribution centered on zero and with an RMS set to C_4 . The other parameters represent:

- C_0 : M_{T2}^{Max} , i.e. the position of the M_{T2} end-point;
- C_1 : slope of the first line;
- C_2 : height of the kink between the two lines;
- C_3 : slope of the second line;
- C_5 : N_B^{Exp} , i.e. the number of expected background events under the Z peak;
- C_6 : $M_Z + M_\chi^{trial}$, i.e. the position of the (pseudo) Z peak; and,
- C_7 : the width of the pseudo Z peak.

The results of the primary fits are presented in tables 36 to 55. Figures 23 and 24 illustrate a few of them. Again, no M_{T2}^{Max} measurements on our samples are feasible when $M_{\tilde{\chi}_2^0} \geq 700$ GeV for the S1 samples and $M_{\tilde{\chi}_2^0} \geq 400$ GeV for the S2 samples.

For the secondary fits, the f_{down} and f_{up} functional forms are directly applied onto the $(M_{T2}^{Max}, M_\chi^{trial})$ two-dimensional plots. The results of these latter fits, that allow to extract the mass measurements, are presentend in tables 56 to 57 and a few of them are illustrated in figures 25 and 26.

Process	Theor. M_{T2}^{Max} (GeV)	M_{T2} (GeV)	Fit χ^2/N_{dof}
Signal S1 [$M_{\tilde{\chi}_2^0}, M_{\tilde{\ell}^\pm}, M_{\tilde{\chi}_1^0}$] GeV			
[100, 75, 50]	Undef.	—	—
[200, 150, 100]	Undef.	—	—
[300, 225, 150]	Undef.	—	—
[400, 300, 200]	Undef.	—	—
[500, 375, 250]	Undef.	—	—
[600, 450, 300]	Undef.	—	—
[700, 525, 350]	Undef.	—	—

Table 36. M_{T2}^{Max} measurements of the S1 samples for $M_\chi^{trial} = 0$ GeV.

Process	Theor. M_{T2}^{Max} (GeV)	M_{T2} (GeV)	Fit χ^2/N_{dof}
Signal S2 [$M_{\tilde{\chi}_2^0}, M_{\tilde{\chi}_1^0}$] GeV			
[100, 50]	75.0	$60.00 \pm 18.71(stat) \pm 1.12(syst)$	1.239
[105, 13.8]	103.2	$102.39 \pm 0.42(stat) \pm 1.90(syst)$	2.637
[115, 13.8]	113.3	$102.50 \pm 0.12(stat) \pm 1.91(syst)$	0.764
[125, 13.8]	123.5	$122.50 \pm 0.03(stat) \pm 2.28(syst)$	1.006
[135, 13.8]	133.6	$127.80 \pm 2.46(stat) \pm 2.38(syst)$	0.806
[145, 13.8]	143.7	$136.52 \pm 14.31(stat) \pm 2.54(syst)$	0.719
[150, 50]	133.3	$119.99 \pm 17.12(stat) \pm 2.23(syst)$	1.205
[200, 100]	150.0	$146.15 \pm 9.99(stat) \pm 2.72(syst)$	1.210
[250, 125]	187.5	$188.52 \pm 14.57(stat) \pm 3.51(syst)$	1.245
[300, 150]	225.0	$216.17 \pm 14.50(stat) \pm 4.02(syst)$	1.007
[400, 200]	—	—	—
[500, 250]	—	—	—
[600, 300]	—	—	—
[700, 350]	—	—	—

Table 37. M_{T2}^{Max} measurements of the S2 samples for $M_{\chi}^{trial} = 0$ GeV.

Process	Theor. M_{T2}^{Max} (GeV)	M_{T2} (GeV)	Fit χ^2/N_{dof}
Signal S1 [$M_{\tilde{\chi}_2^0}, M_{\tilde{\ell}^\pm}, M_{\tilde{\chi}_1^0}$] GeV			
[100, 75, 50]	Undef.	—	—
[200, 150, 100]	Undef.	—	—
[300, 225, 150]	Undef.	—	—
[400, 300, 200]	Undef.	—	—
[500, 375, 250]	Undef.	—	—
[600, 450, 300]	Undef.	—	—
[700, 525, 350]	—	—	—

Table 38. M_{T2}^{Max} measurements of the S1 samples for $M_{\chi}^{trial} = 13.8$ GeV.

Process	Theor. M_{T2}^{Max} (GeV)	M_{T2} (GeV)	Fit χ^2/N_{dof}
<u>Signal S2</u> $[M_{\tilde{\chi}_2^0}, M_{\tilde{\chi}_1^0}]$ GeV			
[100, 50]	77.5	$67.49 \pm 0.05(stat) \pm 1.21(syst)$	0.976
[105, 13.8]	105.0	$117.50 \pm 0.07(stat) \pm 2.11(syst)$	1.423
[115, 13.8]	115.0	$117.50 \pm 0.24(stat) \pm 2.11(syst)$	1.993
[125, 13.8]	125.0	$117.50 \pm 0.22(stat) \pm 2.11(syst)$	0.776
[135, 13.8]	135.0	$128.25 \pm 7.48(stat) \pm 2.31(syst)$	0.687
[145, 13.8]	145.0	$158.99 \pm 1.12(stat) \pm 2.86(syst)$	0.478
[150, 50]	134.7	$142.67 \pm 9.03(stat) \pm 2.57(syst)$	0.974
[200, 100]	151.3	$143.74 \pm 14.88(stat) \pm 2.59(syst)$	0.794
[250, 125]	188.5	$192.72 \pm 4.00(stat) \pm 3.47(syst)$	0.590
[300, 150]	225.8	$219.64 \pm 3.88(stat) \pm 3.95(syst)$	0.697
[400, 200]	—	—	—
[500, 250]	—	—	—
[600, 300]	—	—	—
[700, 350]	—	—	—

Table 39. M_{T2}^{Max} measurements of the S2 samples for $M_{\chi}^{trial} = 13.8$ GeV.

Process	Theor. M_{T2}^{Max} (GeV)	M_{T2} (GeV)	Fit χ^2/N_{dof}
<u>Signal S1</u> $[M_{\tilde{\chi}_2^0}, M_{\tilde{\ell}^\pm}, M_{\tilde{\chi}_1^0}]$ GeV			
[100, 75, 50]	100.0	$102.20 \pm 0.31(stat) \pm 1.50(syst)$	2.555
[200, 150, 100]	Undef.	—	—
[300, 225, 150]	Undef.	—	—
[400, 300, 200]	Undef.	—	—
[500, 375, 250]	Undef.	—	—
[600, 450, 300]	Undef.	—	—
[700, 525, 350]	—	—	—

Table 40. M_{T2}^{Max} measurements of the S1 samples for $M_{\chi}^{trial} = 50$ GeV.

Process	Theor. M_{T2}^{Max} (GeV)	M_{T2} (GeV)	Fit χ^2/N_{dof}
<u>Signal S2</u> $[M_{\tilde{\chi}_2^0}, M_{\tilde{\chi}_1^0}]$ GeV			
[100, 50]	100.0	$102.49 \pm 0.18(stat) \pm 1.51(syst)$	1.096
[105, 13.8]	141.2	$148.26 \pm 14.09(stat) \pm 2.18(syst)$	1.371
[115, 13.8]	151.2	$152.50 \pm 0.01(stat) \pm 2.24(syst)$	1.366
[125, 13.8]	161.2	$153.14 \pm 3.67(stat) \pm 2.25(syst)$	0.759
[135, 13.8]	171.2	$152.50 \pm 0.05(stat) \pm 2.24(syst)$	0.493
[145, 13.8]	181.2	$190.26 \pm 9.54(stat) \pm 2.80(syst)$	0.602
[150, 50]	150.0	$152.50 \pm 0.06(stat) \pm 2.24(syst)$	1.101
[200, 100]	165.1	$156.85 \pm 3.68(stat) \pm 2.31(syst)$	1.038
[250, 125]	200.0	$197.50 \pm 2.89(stat) \pm 2.90(syst)$	0.630
[300, 150]	235.6	$246.67 \pm 1.91(stat) \pm 3.63(syst)$	0.680
[400, 200]	—	—	—
[500, 250]	—	—	—
[600, 300]	—	—	—
[700, 350]	—	—	—

Table 41. M_{T2}^{Max} measurements of the S2 samples for $M_{\chi}^{trial} = 50$ GeV.

Process	Theor. M_{T2}^{Max} (GeV)	M_{T2} (GeV)	Fit χ^2/N_{dof}
<u>Signal S1</u> $[M_{\tilde{\chi}_2^0}, M_{\tilde{\ell}^\pm}, M_{\tilde{\chi}_1^0}]$ GeV			
[100, 75, 50]	149.8	$152.98 \pm 0.15(stat) \pm 1.68(syst)$	2.436
[200, 150, 100]	200.0	$199.91 \pm 0.35(stat) \pm 2.20(syst)$	0.559
[300, 225, 150]	Undef.	—	—
[400, 300, 200]	Undef.	—	—
[500, 375, 250]	Undef.	—	—
[600, 450, 300]	Undef.	—	—
[700, 525, 350]	—	—	—

Table 42. M_{T2}^{Max} measurements of the S1 samples for $M_{\chi}^{trial} = 100$ GeV.

Process	Theor. M_{T2}^{Max} (GeV)	M_{T2} (GeV)	Fit χ^2/N_{dof}
<u>Signal S2</u> $[M_{\tilde{\chi}_2^0}, M_{\tilde{\chi}_1^0}]$ GeV			
[100, 50]	150.0	$152.49 \pm 0.09(stat) \pm 1.68(syst)$	0.584
[105, 13.8]	191.2	$200.44 \pm 18.86(stat) \pm 2.20(syst)$	1.052
[115, 13.8]	201.2	$202.50 \pm 0.01(stat) \pm 2.23(syst)$	1.138
[125, 13.8]	211.2	$202.50 \pm 0.13(stat) \pm 2.23(syst)$	0.565
[135, 13.8]	221.2	$210.14 \pm 4.50(stat) \pm 2.31(syst)$	0.491
[145, 13.8]	231.2	$237.70 \pm 12.79(stat) \pm 2.61(syst)$	0.558
[150, 50]	200.0	$202.50 \pm 0.10(stat) \pm 2.23(syst)$	0.799
[200, 100]	200.0	$202.49 \pm 0.01(stat) \pm 2.23(syst)$	0.673
[250, 125]	230.8	$239.16 \pm 14.75(stat) \pm 2.63(syst)$	0.574
[300, 150]	263.0	$250.15 \pm 1.24(stat) \pm 2.75(syst)$	0.540
[400, 200]	—	—	—
[500, 250]	—	—	—
[600, 300]	—	—	—
[700, 350]	—	—	—

Table 43. M_{T2}^{Max} measurements of the S2 samples for $M_\chi^{trial} = 100$ GeV.

Process	Theor. M_{T2}^{Max} (GeV)	M_{T2} (GeV)	Fit χ^2/N_{dof}
<u>Signal S1</u> $[M_{\tilde{\chi}_2^0}, M_{\tilde{\ell}^\pm}, M_{\tilde{\chi}_1^0}]$ GeV			
[100, 75, 50]	174.8	$177.86 \pm 0.13(stat) \pm 1.81(syst)$	1.814
[200, 150, 100]	224.9	$225.28 \pm 0.78(stat) \pm 2.30(syst)$	1.284
[300, 225, 150]	258.2	$277.64 \pm 0.32(stat) \pm 2.83(syst)$	0.526
[400, 300, 200]	Undef.	—	—
[500, 375, 250]	Undef.	—	—
[600, 450, 300]	Undef.	—	—
[700, 525, 350]	—	—	—

Table 44. M_{T2}^{Max} measurements of the S1 samples for $M_\chi^{trial} = 125$ GeV.

Process	Theor. M_{T2}^{Max} (GeV)	M_{T2} (GeV)	Fit χ^2/N_{dof}
<u>Signal S2</u> $[M_{\tilde{\chi}_2^0}, M_{\tilde{\chi}_1^0}]$ GeV			
[100, 50]	175.0	$177.50 \pm 0.06(stat) \pm 1.81(syst)$	0.742
[105, 13.8]	216.2	$227.01 \pm 18.62(stat) \pm 2.32(syst)$	1.296
[115, 13.8]	226.2	$227.50 \pm 0.01(stat) \pm 2.32(syst)$	1.228
[125, 13.8]	236.2	$227.49 \pm 0.03(stat) \pm 2.32(syst)$	0.493
[135, 13.8]	246.2	$227.50 \pm 0.04(stat) \pm 2.32(syst)$	0.461
[145, 13.8]	256.2	$246.11 \pm 6.54(stat) \pm 2.51(syst)$	0.566
[150, 50]	225.0	$227.50 \pm 0.005(stat) \pm 2.32(syst)$	1.167
[200, 100]	225.0	$227.50 \pm 0.02(stat) \pm 2.32(syst)$	0.965
[250, 125]	250.0	$250.99 \pm 18.17(stat) \pm 2.56(syst)$	0.586
[300, 150]	280.7	$266.70 \pm 1.93(stat) \pm 2.72(syst)$	0.566
[400, 200]	—	—	—
[500, 250]	—	—	—
[600, 300]	—	—	—
[700, 350]	—	—	—

Table 45. M_{T2}^{Max} measurements of the S2 samples for $M_\chi^{trial} = 125$ GeV.

Process	Theor. M_{T2}^{Max} (GeV)	M_{T2} (GeV)	Fit χ^2/N_{dof}
<u>Signal S1</u> $[M_{\tilde{\chi}_2^0}, M_{\tilde{\ell}^\pm}, M_{\tilde{\chi}_1^0}]$ GeV			
[100, 75, 50]	199.8	$202.50 \pm 0.0003(stat) \pm 1.96(syst)$	1.857
[200, 150, 100]	249.8	$250.29 \pm 0.37(stat) \pm 2.43(syst)$	0.623
[300, 225, 150]	300.0	$302.54 \pm 0.52(stat) \pm 2.93(syst)$	0.345
[400, 300, 200]	300.0	$352.50 \pm 0.01(stat) \pm 3.42(syst)$	0.239
[500, 375, 250]	Undef.	—	—
[600, 450, 300]	Undef.	—	—
[700, 525, 350]	—	—	—

Table 46. M_{T2}^{Max} measurements of the S1 samples for $M_\chi^{trial} = 150$ GeV.

Process	Theor. M_{T2}^{Max} (GeV)	M_{T2} (GeV)	Fit χ^2/N_{dof}
<u>Signal S2</u> $[M_{\tilde{\chi}_2^0}, M_{\tilde{\chi}_1^0}]$ GeV			
[100, 50]	200.0	$202.50 \pm 0.51(stat) \pm 1.96(syst)$	0.920
[105, 13.8]	241.2	$252.50 \pm 0.003(stat) \pm 2.45(syst)$	1.684
[115, 13.8]	251.2	$252.50 \pm 0.02(stat) \pm 2.45(syst)$	1.574
[125, 13.8]	261.2	$252.50 \pm 0.02(stat) \pm 2.45(syst)$	0.716
[135, 13.8]	271.2	$252.50 \pm 0.03(stat) \pm 2.45(syst)$	0.505
[145, 13.8]	281.2	$267.16 \pm 19.58(stat) \pm 2.59(syst)$	0.600
[150, 50]	250.0	$252.50 \pm 0.003(stat) \pm 2.45(syst)$	1.552
[200, 100]	250.0	$252.50 \pm 0.07(stat) \pm 2.45(syst)$	1.372
[250, 125]	275.0	$252.48 \pm 0.09(stat) \pm 2.45(syst)$	0.701
[300, 150]	300.0	$286.68 \pm 2.41(stat) \pm 2.78(syst)$	0.645
[400, 200]	—	—	—
[500, 250]	—	—	—
[600, 300]	—	—	—
[700, 350]	—	—	—

Table 47. M_{T2}^{Max} measurements of the S2 samples for $M_\chi^{trial} = 150$ GeV.

Process	Theor. M_{T2}^{Max} (GeV)	M_{T2} (GeV)	Fit χ^2/N_{dof}
<u>Signal S1</u> $[M_{\tilde{\chi}_2^0}, M_{\tilde{\ell}^\pm}, M_{\tilde{\chi}_1^0}]$ GeV			
[100, 75, 50]	249.7	$252.54 \pm 0.04(stat) \pm 2.27(syst)$	1.908
[200, 150, 100]	299.7	$290.92 \pm 0.16(stat) \pm 2.62(syst)$	2.085
[300, 225, 150]	349.7	$352.89 \pm 0.55(stat) \pm 3.18(syst)$	0.360
[400, 300, 200]	400.0	$402.50 \pm 0.01(stat) \pm 3.62(syst)$	0.217
[500, 375, 250]	412.0	$432.60 \pm 0.01(stat) \pm 3.89(syst)$	0.008
[600, 450, 300]	Undef.	—	—
[700, 525, 350]	—	—	—

Table 48. M_{T2}^{Max} measurements of the S1 samples for $M_\chi^{trial} = 200$ GeV.

Process	Theor. M_{T2}^{Max} (GeV)	M_{T2} (GeV)	Fit χ^2/N_{dof}
<u>Signal S2</u> [$M_{\tilde{\chi}_2^0}, M_{\tilde{\chi}_1^0}$] GeV			
[100, 50]	250.0	$255.83 \pm 3.81(stat) \pm 2.30(syst)$	1.128
[105, 13.8]	291.2	$302.50 \pm 0.05(stat) \pm 2.72(syst)$	1.739
[115, 13.8]	301.2	$302.49 \pm 0.18(stat) \pm 2.72(syst)$	1.733
[125, 13.8]	311.2	$302.50 \pm 0.05(stat) \pm 2.72(syst)$	0.603
[135, 13.8]	321.2	$302.49 \pm 0.05(stat) \pm 2.72(syst)$	0.642
[145, 13.8]	331.2	$302.50 \pm 0.07(stat) \pm 2.72(syst)$	0.592
[150, 50]	300.0	$302.49 \pm 0.07(stat) \pm 2.72(syst)$	1.597
[200, 100]	300.0	$302.50 \pm 0.08(stat) \pm 2.72(syst)$	1.613
[250, 125]	325.0	$313.23 \pm 3.74(stat) \pm 2.82(syst)$	0.844
[300, 150]	350.0	$333.17 \pm 0.86(stat) \pm 3.00(syst)$	0.694
[400, 200]	—	—	—
[500, 250]	—	—	—
[600, 300]	—	—	—
[700, 350]	—	—	—

Table 49. M_{T2}^{Max} measurements of the S2 samples for $M_\chi^{trial} = 200$ GeV.

Process	Theor. M_{T2}^{Max} (GeV)	M_{T2} (GeV)	Fit χ^2/N_{dof}
<u>Signal S1</u> [$M_{\tilde{\chi}_2^0}, M_{\tilde{\ell}^\pm}, M_{\tilde{\chi}_1^0}$] GeV			
[100, 75, 50]	299.7	$302.51 \pm 0.02(stat) \pm 2.57(syst)$	2.215
[200, 150, 100]	349.6	$350.38 \pm 0.38(stat) \pm 2.98(syst)$	1.160
[300, 225, 150]	399.6	$401.39 \pm 3.10(stat) \pm 3.41(syst)$	0.329
[400, 300, 200]	449.7	$441.63 \pm 1.70(stat) \pm 3.75(syst)$	1.042
[500, 375, 250]	500.0	$502.50 \pm 0.15(stat) \pm 4.27(syst)$	0.212
[600, 450, 300]	516.4	$556.34 \pm 10.55(stat) \pm 4.73(syst)$	0.102
[700, 525, 350]	—	—	—

Table 50. M_{T2}^{Max} measurements of the S1 samples for $M_\chi^{trial} = 250$ GeV.

Process	Theor. M_{T2}^{Max} (GeV)	M_{T2} (GeV)	Fit χ^2/N_{dof}
<u>Signal S2</u> [$M_{\tilde{\chi}_2^0}, M_{\tilde{\chi}_1^0}$] GeV			
[100, 50]	300.0	$305.18 \pm 3.40(stat) \pm 2.59(syst)$	1.084
[105, 13.8]	341.2	$352.49 \pm 0.02(stat) \pm 3.00(syst)$	1.717
[115, 13.8]	351.2	$352.49 \pm 0.21(stat) \pm 3.00(syst)$	1.898
[125, 13.8]	361.2	$352.50 \pm 0.05(stat) \pm 3.00(syst)$	0.796
[135, 13.8]	371.2	$352.50 \pm 0.06(stat) \pm 3.00(syst)$	0.614
[145, 13.8]	381.2	$362.14 \pm 2.43(stat) \pm 3.08(syst)$	0.608
[150, 50]	350.0	$352.50 \pm 0.10(stat) \pm 3.00(syst)$	1.874
[200, 100]	350.0	$352.50 \pm 0.05(stat) \pm 3.00(syst)$	1.551
[250, 125]	375.0	$362.70 \pm 4.50(stat) \pm 3.08(syst)$	0.878
[300, 150]	400.0	$380.55 \pm 1.37(stat) \pm 3.23(syst)$	0.643
[400, 200]	—	—	—
[500, 250]	—	—	—
[600, 300]	—	—	—
[700, 350]	—	—	—

Table 51. M_{T2}^{Max} measurements of the S2 samples for $M_\chi^{trial} = 250$ GeV.

Process	Theor. M_{T2}^{Max} (GeV)	M_{T2} (GeV)	Fit χ^2/N_{dof}
<u>Signal S1</u> [$M_{\tilde{\chi}_2^0}, M_{\tilde{\ell}^\pm}, M_{\tilde{\chi}_1^0}$] GeV			
[100, 75, 50]	349.7	$349.56 \pm 0.12(stat) \pm 2.90(syst)$	1.852
[200, 150, 100]	399.5	$399.04 \pm 0.15(stat) \pm 3.31(syst)$	0.746
[300, 225, 150]	449.5	$452.50 \pm 0.01(stat) \pm 3.76(syst)$	0.360
[400, 300, 200]	499.5	$503.32 \pm 4.22(stat) \pm 4.18(syst)$	0.298
[500, 375, 250]	549.7	$552.50 \pm 0.57(stat) \pm 4.59(syst)$	0.253
[600, 450, 300]	600.0	$599.40 \pm 16.88(stat) \pm 4.97(syst)$	0.113
[700, 525, 350]	—	—	—

Table 52. M_{T2}^{Max} measurements of the S1 samples for $M_\chi^{trial} = 300$ GeV.

Process	Theor. M_{T2}^{Max} (GeV)	M_{T2} (GeV)	Fit χ^2/N_{dof}
<u>Signal S2</u> [$M_{\tilde{\chi}_2^0}, M_{\tilde{\chi}_1^0}$] GeV			
[100, 50]	350.0	$355.75 \pm 7.34(stat) \pm 2.95(syst)$	0.982
[105, 13.8]	391.2	$402.50 \pm 0.31(stat) \pm 3.34(syst)$	1.465
[115, 13.8]	401.2	$402.50 \pm 0.15(stat) \pm 3.34(syst)$	1.596
[125, 13.8]	411.2	$402.50 \pm 0.18(stat) \pm 3.34(syst)$	0.643
[135, 13.8]	421.2	$402.50 \pm 0.21(stat) \pm 3.34(syst)$	0.545
[145, 13.8]	431.2	$402.50 \pm 0.07(stat) \pm 3.34(syst)$	0.517
[150, 50]	400.0	$402.50 \pm 0.02(stat) \pm 3.34(syst)$	1.755
[200, 100]	400.0	$402.50 \pm 0.26(stat) \pm 3.34(syst)$	1.456
[250, 125]	425.0	$403.75 \pm 9.21(stat) \pm 3.35(syst)$	0.730
[300, 150]	450.0	$427.50 \pm 0.34(stat) \pm 3.55(syst)$	0.635
[400, 200]	—	—	—
[500, 250]	—	—	—
[600, 300]	—	—	—
[700, 350]	—	—	—

Table 53. M_{T2}^{Max} measurements of the S2 samples for $M_{\chi}^{trial} = 300$ GeV.

Process	Theor. M_{T2}^{Max} (GeV)	M_{T2} (GeV)	Fit χ^2/N_{dof}
Signal S1 $[M_{\tilde{\chi}_2^0}, M_{\tilde{\ell}^\pm}, M_{\tilde{\chi}_1^0}]$ GeV			
[100, 75, 50]	399.7	$399.58 \pm 0.12(stat) \pm 3.24(syst)$	2.513
[200, 150, 100]	449.5	$450.82 \pm 0.69(stat) \pm 3.65(syst)$	1.140
[300, 225, 150]	499.4	$502.50 \pm 0.04(stat) \pm 4.07(syst)$	0.429
[400, 300, 200]	549.4	$552.50 \pm 0.01(stat) \pm 4.48(syst)$	0.384
[500, 375, 250]	599.5	$586.74 \pm 11.04(stat) \pm 4.75(syst)$	0.130
[600, 450, 300]	649.7	$651.60 \pm 2.46(stat) \pm 5.28(syst)$	0.108
[700, 525, 350]	—	—	—

Table 54. M_{T2}^{Max} measurements of the S1 samples for $M_\chi^{trial} = 350$ GeV.

Process	Theor. M_{T2}^{Max} (GeV)	M_{T2} (GeV)	Fit χ^2/N_{dof}
<u>Signal S2</u> $[M_{\tilde{\chi}_2^0}, M_{\tilde{\chi}_1^0}]$ GeV			
[100, 50]	400.0	$405.33 \pm 5.85(stat) \pm 3.28(syst)$	1.156
[105, 13.8]	441.2	$452.50 \pm 0.01(stat) \pm 3.67(syst)$	1.391
[115, 13.8]	451.2	$452.50 \pm 0.29(stat) \pm 3.67(syst)$	1.656
[125, 13.8]	461.2	$452.50 \pm 0.07(stat) \pm 3.67(syst)$	0.748
[135, 13.8]	471.2	$452.48 \pm 0.06(stat) \pm 3.67(syst)$	0.612
[145, 13.8]	481.2	$452.50 \pm 0.19(stat) \pm 3.67(syst)$	0.593
[150, 50]	450.0	$470.85 \pm 3.14(stat) \pm 3.81(syst)$	1.471
[200, 100]	450.0	$452.50 \pm 0.06(stat) \pm 3.67(syst)$	1.147
[250, 125]	475.0	$480.09 \pm 11.87(stat) \pm 3.89(syst)$	0.846
[300, 150]	500.0	$475.29 \pm 0.63(stat) \pm 3.85(syst)$	0.709
[400, 200]	—	—	—
[500, 250]	—	—	—
[600, 300]	—	—	—
[700, 350]	—	—	—

Table 55. M_{T2}^{Max} measurements of the S2 samples for $M_{\tilde{\chi}}^{trial} = 350$ GeV.

3.6.2. c. Mass Extraction

Process	$M_{\tilde{\chi}_2^0}^{Fit}$ (GeV)	$M_{\tilde{\ell}^\pm}^{Fit}$ (GeV)	$M_{\tilde{\chi}_1^0}^{Fit}$ (GeV)	Fit χ^2/N_{dof}
<u>Signal S1</u> $[M_{\tilde{\chi}_2^0}, M_{\tilde{\ell}^\pm}, M_{\tilde{\chi}_1^0}]$ GeV				
[100, 75, 50]	102.49 ± 9.76	78.16 ± 14.48	49.82 ± 9.95	0.355
[200, 150, 100]	199.86 ± 13.87	160.50 ± 19.05	100.00 ± 14.35	2.492
[300, 225, 150]	278.16 ± 37.77	178.15 ± 44.21	125.45 ± 34.60	0.023
[400, 300, 200]	349.20 ± 288.96	198.48 ± 336.04	147.22 ± 299.12	2.681
[500, 375, 250]	501.50 ± 2.96	339.83 ± 15.23	250.00 ± 0.10	1.576
[600, 450, 300]	555.32 ± 1059.60	312.33 ± 1239.21	249.66 ± 1125.28	—
[700, 525, 350]	—	—	—	—

Table 56. Mass extraction from M_{T2}^{Max} measurements of the S1 samples.

Once again, we notice, that *ICA* and *MT2* methods do not give access to the same informations: $M_{\tilde{\chi}_2^0} + M_{\tilde{\chi}_1^\pm}$, versus $M_{\tilde{\chi}_2^0}$, and $M_{\tilde{\chi}_1^0}$ (plus possibly $M_{\tilde{\ell}^\pm}$), respectively. The precision of the *MT2* mass measurements are summarized hereafter:

- S1 signal:

- $\delta M_{\tilde{\chi}_2^0}/M_{\tilde{\chi}_2^0} < 7 - 14\%$ for $M_{\tilde{\chi}_2^0} < 400$ GeV
- $\delta M_{\tilde{\ell}^\pm}/M_{\tilde{\ell}^\pm} < 12 - 25\%$ for $M_{\tilde{\chi}_2^0} < 400$ GeV
- $\delta M_{\tilde{\chi}_1^0}/M_{\tilde{\chi}_1^0} < 14 - 28\%$ for $M_{\tilde{\chi}_2^0} < 400$ GeV
- S2a signal:
 - $\delta M_{\tilde{\chi}_2^0}/M_{\tilde{\chi}_2^0} < 41\%$ for $M_{\tilde{\chi}_2^0} < 400$ GeV
 - bad sensitivity to $M_{\tilde{\chi}_1^0}$
- S2b signal:
 - $\delta M_{\tilde{\chi}_2^0}/M_{\tilde{\chi}_2^0} < 0.6 - 12\%$ for $M_{\tilde{\chi}_2^0} < 400$ GeV
 - $\delta M_{\tilde{\chi}_1^0}/M_{\tilde{\chi}_1^0} < 4 - 13\%$ for $M_{\tilde{\chi}_2^0} < 150$ GeV

Even though the $MT2$ method, appears to be slightly less accurate than ICA (itself being much less accurate than $DileME$), it provides much more informations on different individual particles mass than ICA , or $DileME$, or even a combination of ICA and $DileME$. However M_{T2} end-points are known to be sometimes difficult to measure [77], especially for small signals in the presence of some background.

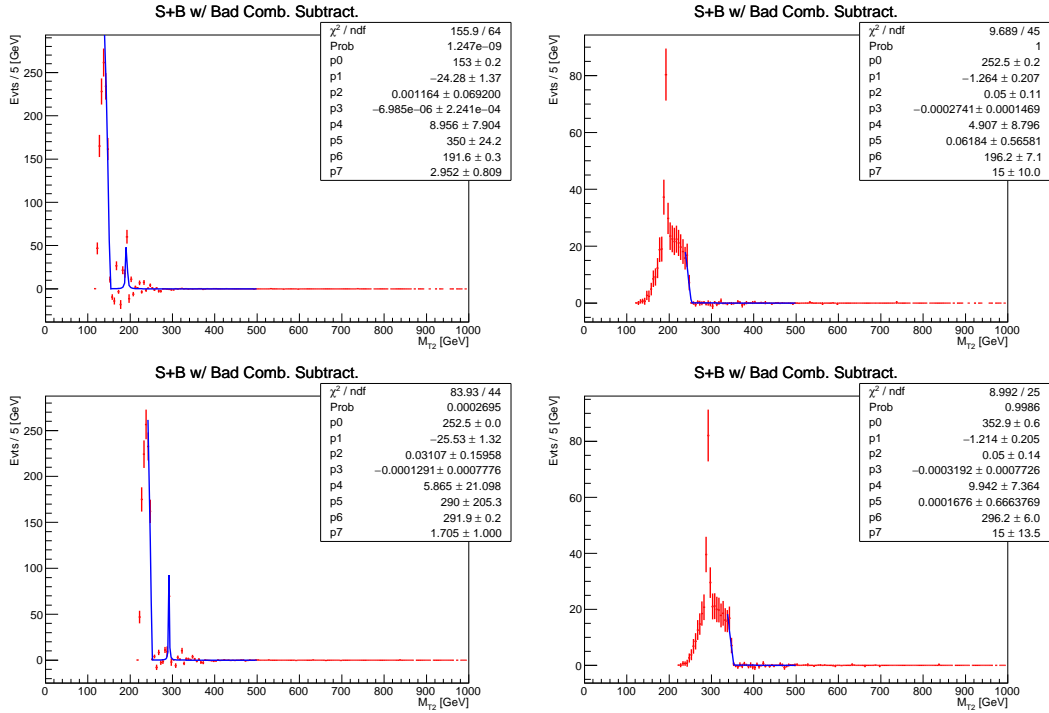


Figure 23. A few examples of M_{T2}^{Max} measurements on the S1 samples. For the top and the bottom row $M_{trial}^X = 100$ and 200 GeV, respectively. For the left and the right column $M_{\tilde{\chi}_2^0} = 100$ and 300 GeV, respectively.

The last remark, is that *ICA* appears to have a higher mass reach than *DileME* and *MT2*. This is mostly due to the *ICA* reduced systematic uncertainty in its background subtraction. So, we see that the three methods have quite different advantages and drawbacks, they also have different systematic uncertainties. They are therefore complementary and the best SUSY mass informations can be extracted by combining them.

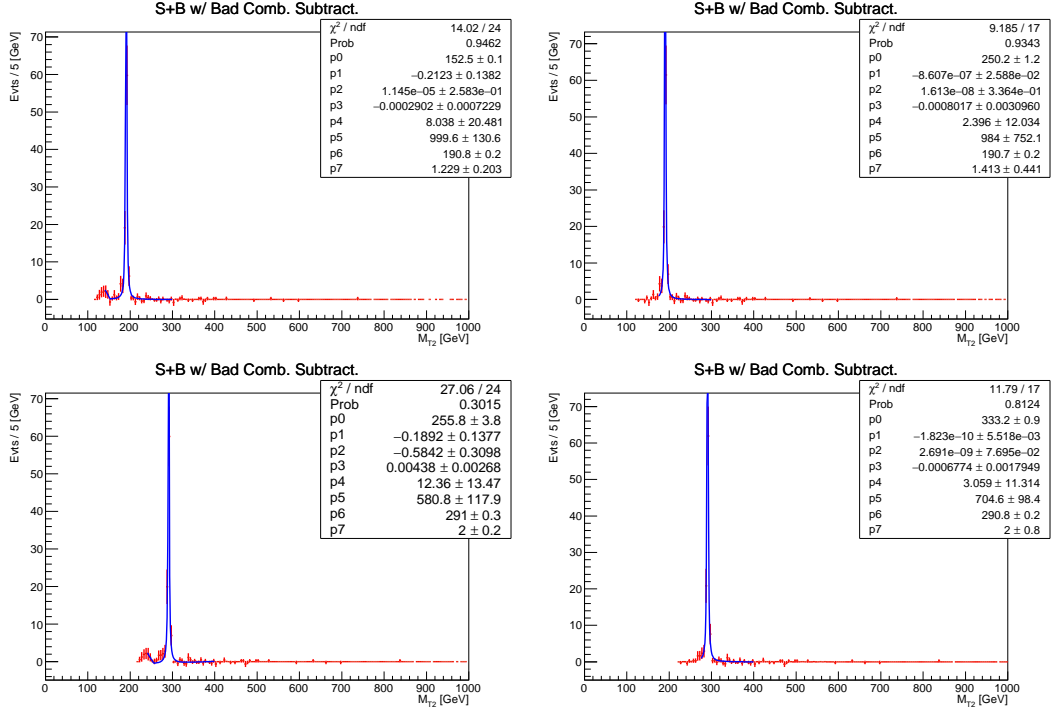


Figure 24. A few examples of M_{T2}^{Max} measurements on the S2 samples. For the top and the bottom row $M_{trial}^X = 100$ and 200 GeV, respectively. For the left and the right column $M_{X_2^0} = 100$ and 300 GeV, respectively.

Process	$M_{\tilde{\chi}_2^0}^{Fit}$ (GeV)	$M_{\tilde{\chi}_1^0}^{Fit}$ (GeV)	Fit χ^2/N_{dof}
<u>Signal S2</u> [$M_{\tilde{\chi}_2^0}, M_{\tilde{\chi}_1^0}$] GeV			
[100, 50]	61.04 ± 24.80	7.97 ± 24.82	0.195
[105, 13.8]	109.09 ± 0.96	8.28 ± 0.36	1.661
[115, 13.8]	109.67 ± 0.78	8.28 ± 0.32	1.788
[125, 13.8]	122.14 ± 2.26	19.61 ± 2.65	0.561
[135, 13.8]	135.55 ± 5.53	32.76 ± 5.76	0.276
[145, 13.8]	217.75 ± 14.22	112.56 ± 15.09	2.706
[150, 50]	152.17 ± 18.13	49.01 ± 18.22	1.811
[200, 100]	166.44 ± 11.20	63.95 ± 11.43	0.027
[250, 125]	262.12 ± 1.55	150.00 ± 0.03	4.118
[300, 150]	424.48 ± 45.70	297.99 ± 48.13	4.131
[400, 200]	—	—	—
[500, 250]	—	—	—
[600, 300]	—	—	—
[700, 350]	—	—	—

Table 57. Mass extraction from M_{T2}^{Max} measurements of the S2 samples.

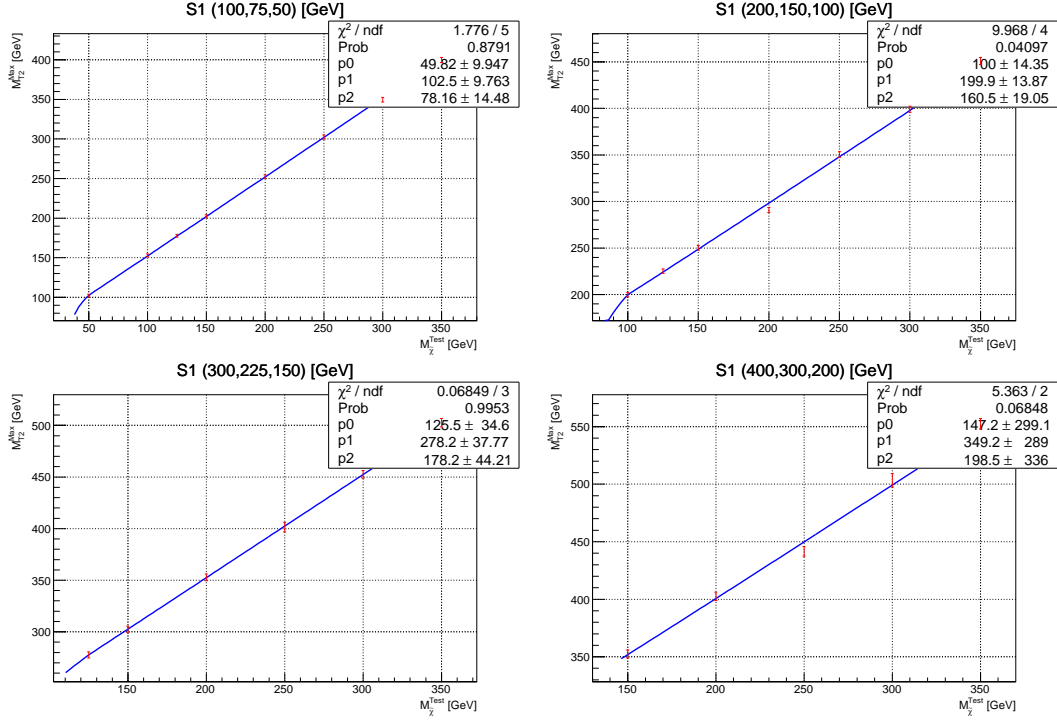


Figure 25. Examples of $MT2$ secondary fits to the S1 samples for $M_{\tilde{\chi}_2^0} = 100$ (top left), 200 (top right), 300 (bottom left) and 400 (bottom right) GeV.

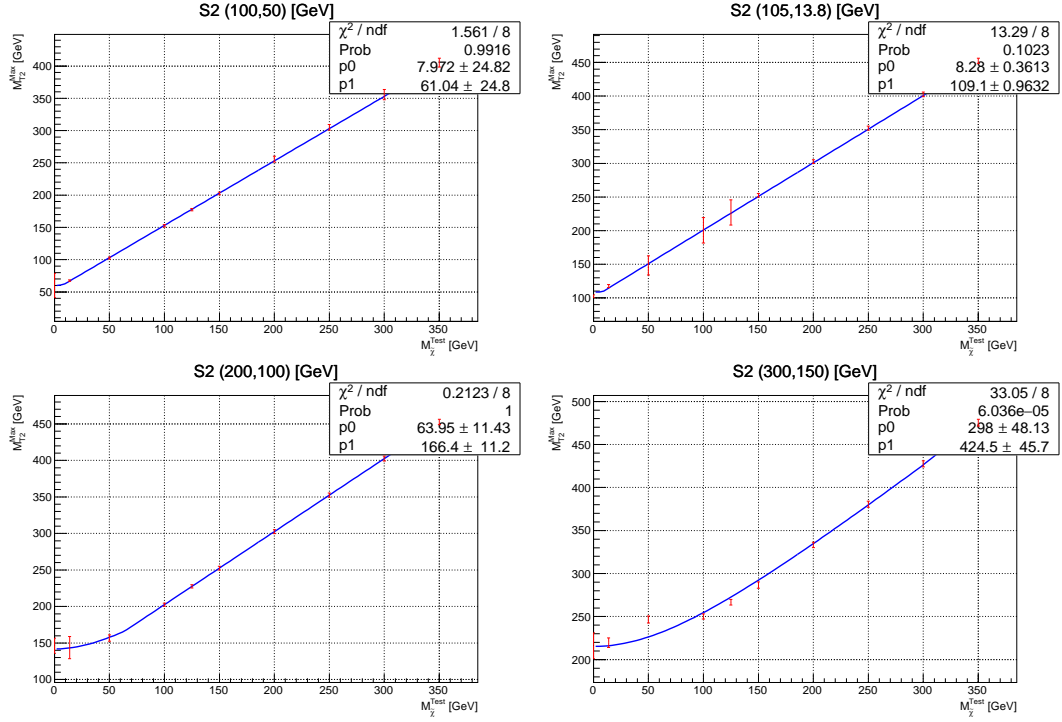


Figure 26. Examples of $MT2$ secondary fits to the S2 samples for $M_{\tilde{\chi}_2^0} = 100$ (top left), 105 (top right), 200 (bottom left) and 300 (bottom right) GeV.

4 Conclusions

We propose a new method to measure the mass of charged final states using the integral charge asymmetry A_C at the LHC.

At first we detail and test this method on the $p + p \rightarrow W^\pm \rightarrow \ell^\pm \nu$ inclusive process. Then we apply it on a SUSY search of interest, namely the $p + p \rightarrow \tilde{\chi}_1^\pm + \tilde{\chi}_2^0 \rightarrow 3\ell^\pm + \cancel{E}_T$ inclusive process. For each process, we start by calculating the central values of A_C using cross section integrators with LO MEs and with three different LO PDFs. MCFM is used for the SM process and Resummino is used for the SUSY process. The same tools are also used to estimate the theoretical uncertainties on A_C . These calculations are repeated varying the mass of the charged final state. Over the studied mass ranges we find that A_C is a monotonically increasing function of $M(FS^\pm)$. This function is well described by a polynomial of logarithms of logarithms of $M(FS^\pm)$. The PDF uncertainty turns out to be the dominant source of the theoretical uncertainty.

The experimental extraction of A_C requires a quantitative estimate of the biases caused by the event selection and by the residual background. To this end MC samples are generated for the considered signal and its related background processes. These samples are passed through a fast simulation of the ATLAS detector response. Realistic values for the systematic uncertainties are taken from publications of LHC data analyses. The full experimental uncertainties as well as the effect of the residual background are consistently propagated through a central value and uncertainties of the measured A_C . This way the measured A_C of each signal sample can be translated into a central value and uncertainties of an indirect measurement of the corresponding $M(FS^\pm)$. The theoretical uncertainties of each measured $M(FS^\pm)$ is summed in quadrature with the experimental uncertainties so as to provide the full uncertainty for this new method.

For the $p + p \rightarrow W^\pm \rightarrow \ell^\pm \nu$ inclusive process, M_{W^\pm} can be indirectly measured with an overall accuracy better than 1.2%. We note that the dispersion of the central values of M_{W^\pm} indirectly measured with the three PDFs are compatible with the total uncertainty of the MSTW2008lo68cl prediction.

For the $p + p \rightarrow \tilde{\chi}_1^\pm + \tilde{\chi}_2^0 \rightarrow 3\ell^\pm + \cancel{E}_T$ inclusive process, without accounting for $\delta(A_C)_{PDF}$, $M_{\tilde{\chi}_1^\pm} + M_{\tilde{\chi}_2^0}$ can be measured with an overall accuracy better than 6% for a sensitivity to the signal in excess of 5σ and with an accuracy better than 4.5% for a sensitivity to the signal in excess of 3σ . These indirect mass measurements are independent of the details of the decay chains of the signal samples. For the considered SUSY process, basic closure tests indicate the indirect mass estimate does not need any linearity nor offset corrections.

We recommend to apply this method using at least NLO A_C templates both for the theoretical and the experimental parts. Indeed, the most precise cross sections and event generations constitute more reliable theory predictions and are in better agreement with the data than LO predictions. NLO or NLL theoretical templates reduce the theoretical

uncertainty, as shown in table 21 for example. Besides, the measurements of $\frac{dA_C(W^\pm \rightarrow \ell^\pm \nu)}{d\eta(\ell^\pm)}$ by the LHC experiments [3] [4] [5] [6] [7] were found to agree well with NLO theory predictions. Even if our asymmetry ratios of the A_C theoretical templates: $\frac{A_C^{NLO}}{A_C^{LO}}$ in Fig. 4 and $\frac{A_C^{NLL}}{A_C^{LO}}$ in Fig. 12, reveal important shape difference of the higher orders with respect to LO, the size of the corrections remain nevertheless quite modest.

Finally, the comparison of the *ICA* (Integral Charge Asymmetry) method for SUSY mass measurements, to the *DileME* (Dilepton Mass Edge) and to the *MT2* (stransverse mass), shows that these three methods are quite complementary.

- the *DileME* method is the most precise one, but it can only access a mass difference and it has a strong bias in certain situations (S2b signal);
- the *MT2* method is the least precise one, it may be difficult to exploit in certain cases, but it provides constraints on individual mass (parent, possibly intermediate and end daughter particle);
- the *MT2* method is slightly more precise than *MT2*, it has the largest mass reach, but it can only access a mass sum.

5 Prospects

In this article we have envisaged two production processes for which the mass measurement from the integral charge asymmetry is applicable. One SM inclusive process $p + p \rightarrow W^\pm \rightarrow 1\ell^\pm + \cancel{E}_T$ and one SUSY inclusive process $p + p \rightarrow \tilde{\chi}_1^\pm + \tilde{\chi}_2^0 \rightarrow 3\ell^\pm + \cancel{E}_T$. Here are the typical physics cases where we think the indirect mass measurement is applicable and complementary with respect to usual mass reconstruction techniques:

- Initial state (IS): processes induced by $q + \bar{q}$, or $q + g$
- Final state (FS): situations where the clasiscal reconstruction techniques are degraded because of
 - bad energy resolution for some objects (τ_{had}^\pm , jets, b-jets,...) combined with a limited statistical significance
(i.e. channels with τ_{had}^\pm compared to channels with e^\pm or μ^\pm)
 - and especially where many particles are undetected

For models with an extended Higgs sector: the $H^{\pm\pm}(\rightarrow W^\pm W^\pm) + H^\mp(\rightarrow \ell^\mp \nu) \rightarrow \ell^\pm \ell^\pm + \ell^\mp + \cancel{E}_T$ channel could be a good physics case because there are 3 undetected neutrinos. On the contrary, for $H^{\pm\pm} + H^\mp \rightarrow \ell^\pm \ell^\pm + \ell^\mp + \cancel{E}_T$, M_T templates should be more accurate. Other physics cases could be searches for $W'^\pm \rightarrow \mu^\pm \nu$ and for $W'^\pm \rightarrow t\bar{b}$.

In SUSY models, here's a non-exhaustive list of processes of interest:

- For "semi-weak" processes:

- $\tilde{\chi}_1^\pm + \tilde{q}$, for which $M_{\tilde{\chi}_1^\pm} + M_{\tilde{q}}$ could be measured
- $\tilde{\chi}_1^\pm + \tilde{g}$, for which $M_{\tilde{\chi}_1^\pm} + M_{\tilde{g}}$ could be measured
- For "weak" processes:
 - Slepton sector: $\tilde{\ell}^\pm + \tilde{\nu}$, for which $M_{\tilde{\ell}^\pm} + M_{\tilde{\nu}}$ could be measured
 - Chargino-neutralino sector: $\tilde{\chi}_1^\pm + \tilde{\chi}_{1,2,3}^0$, to measure $M_{\tilde{\chi}_1^\pm} + M_{\tilde{\chi}_{1,2,3}^0}$

Note, that with the increasing center-of-mass energies and the increasing integrated luminosities of the LHC runs in the years to come, all the vector boson fusion production modes of the above cited processes could also become testable.

This new method only applies after a given event selection and it is indicative of the mass of the final state produced by a charged current process, only when the event selection provides a good statistical significance for that process. Further studies should determine whether a differential charge asymmetry can be used to improve the separation between a given signal and its related background processes and therefore improve the sensitivity to some of this signal properties.

Differential charge asymmetries have been extensively used in other search contexts. For example, in attempts to explain the large forward-backward asymmetries of the $t\bar{t}$ production measured at the TEVATRON by both the CDF [59] and the D0 [60] experiments, some studies were carried out at the LHC to constrain possible contributions from an extra W'^\pm boson. See for example [61][62], using a differential charge asymmetry with respect to a three-body invariant mass, and also [63], using an integral charge asymmetry, and the references therein. Such analyses, using charge asymmetries with respect to the $t\bar{t}$ system rapidity, invariant mass and transverse momentum, have also been performed by the ATLAS and CMS collaborations, see [64] and [65], respectively. We should also mention the differential charge asymmetry with respect to a two-body invariant mass which served as a discriminant between some BSM underlying models [66][67], namely SUSY versus Universal Extra Dimension [68] models, in the study of some specific decay chains.

For what concerns the current article, a first look at the differential charge asymmetry versus the pseudo-rapidity of the charged lepton coming from the chargino decay, reveals promising shape differences between the SM background and the $p + p \rightarrow \tilde{\chi}_1^\pm + \tilde{\chi}_2^0$ SUSY signals. However detailed results are awaiting further studies.

Acknowledgments

We would like to thank the CCIN2P3 computing facility in Lyon where we produced, stored and analyzed our MC samples. The corresponding author thanks Ben O'Leary, Abdelhak Djouadi, and Gordon Watts for useful discussions. He also addresses a special word of thanks to the authors of Resummino, of MCFM, and of Delphes for their help and availability.

A Appendix: Toy Models for the Evolution of A_C

This section is by no mean a formal proof of the properties of the functional forms utilized to fit the different A_C template curves. It's rather a numerical illstrution that render these properties plausible.

A.1 Numerical Example of Evolution of the PDFs, the Quark Currents and A_C

In this paragraph, we describe in a simplified scheme, the choice of these functional forms aimed at fitting:

1. the proton u and d quarks and anti-quarks density functions,
2. the quark currents in the initial state,
3. the dominant flavour contribution to the LO expression of A_C which is recalled in Eq. A.1.

$$A_C \approx \frac{u(x_{1,2}, Q^2)\bar{d}(x_{2,1}, Q^2) - \bar{u}(x_{1,2}, Q^2)d(x_{2,1}, Q^2)}{u(x_{1,2}, Q^2)\bar{d}(x_{2,1}, Q^2) + \bar{u}(x_{1,2}, Q^2)d(x_{2,1}, Q^2)} \quad (\text{A.1})$$

In order to illustrate numerically the Q evolution of the different quantities listed above, we used QCDNUM and the MSTW2008nlo68cl PDF. We set the Björken momentum fractions to arbitray values (compatible with the W^\pm production in p+p collisions at $\sqrt{s} = 7$ TeV), $x_1 = 0.15$ and $x_2 = 8.79 \times 10^{-4}$, and varied Q . The quark density functions $x_1 \cdot u(x_1, Q^2)$, $x_1 \cdot \bar{u}(x_1, Q^2)$, $x_1 \cdot d(x_1, Q^2)$, $x_1 \cdot \bar{d}(x_1, Q^2)$, and $x_2 \cdot u(x_2, Q^2)$, $x_2 \cdot \bar{u}(x_2, Q^2)$, $x_2 \cdot d(x_2, Q^2)$, $x_2 \cdot \bar{d}(x_2, Q^2)$ are shown in the top RHS and LHS of Fig. 27, respectively. At the bottom row of the same figure the positively and negatively charged currents $x_{1,2} \cdot x_{2,1} \cdot u(x_{1,2}, Q^2) \cdot \bar{d}(x_{2,1}, Q^2)$, and $x_{1,2} \cdot x_{2,1} \cdot \bar{u}(x_{1,2}, Q^2) \cdot d(x_{2,1}, Q^2)$ as well as A_C are displayed on the LHS, with a zoom on the low Q end on the RHS.

In sub-section 2.1.3 we consider different polynomials of functions of Q as fit functions to describe the Q evolution of the PDFs. Let's consider here a polynomial of $\text{Log}(\text{Log}(Q))$, in this example, the momentum fractions carried by the incoming quarks: $x_i \cdot f(x_i, Q^2)$ can be fitted by first degree polynomials of $\text{Log}(\text{Log}(Q))$ (though $x_2 \cdot f(x_2, Q^2)$ fits are actually improved by using a second degree polynomial). First degree polynomials of $\text{Log}(\text{Log}(Q))$ give very good fits of the evolution of the "quark currents": $x_1 \cdot x_2 \cdot f_{flav1}(x_1, Q^2) \cdot f_{flav2}(x_2, Q^2)$ c, and, given the hierarchy of the coefficients of these quark currents polynomials, of the A_C as well.

A.2 Toy Models for the Main Properties of A_C^{Fit}

Hereafter, we make the hypothesis that quark currents and A_C can be fitted by the different polynomials of functions of Q evoked above. We want to figure out how the coefficients of such polynomials arrange so as to give the A_C template curves presented in sub-section 2.1, i.e. monotonically increasing functions of Q with a monotonically decreasing slope.

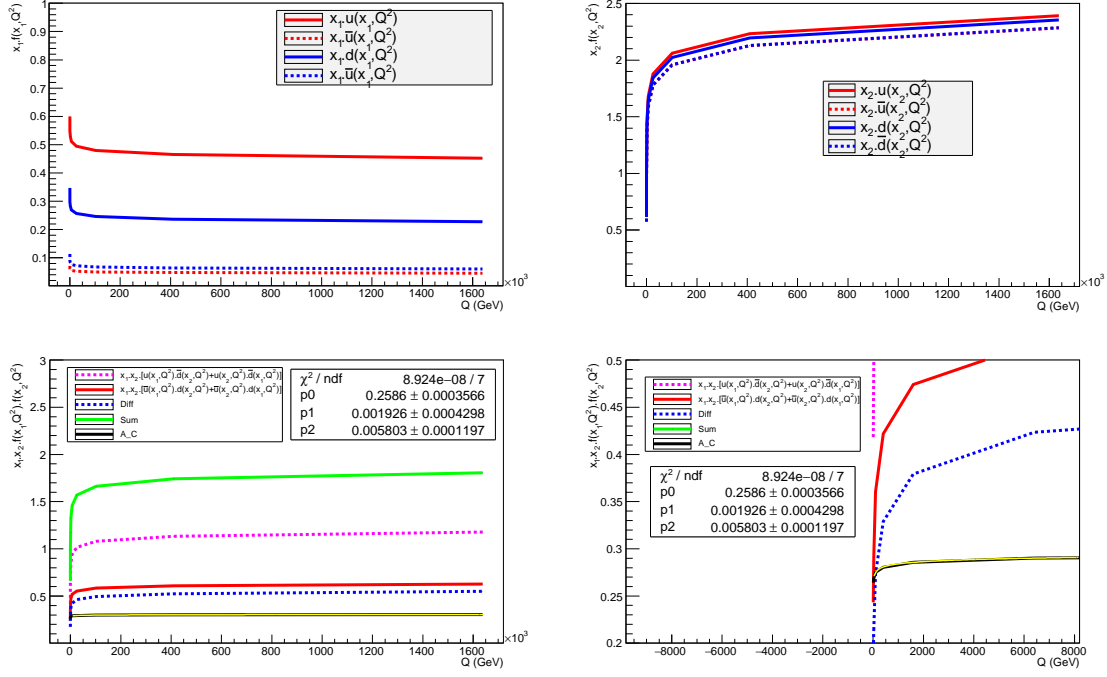


Figure 27. Evolutions of the quark PDFs (top), of the quark currents in the IS and of A_C (bottom) calculated with QCDNUM using the MSTW2008nlo68cl parametrization.

Again, let's consider the simplest case where the first degree polynomials are sufficient. If we denote $x = Q$, and $f(x)$ the fit function, we can write the charged cross sections:

$$\begin{cases} \sigma^+(x) = P_0 + P_1 \cdot f(x) \\ \sigma^-(x) = M_0 + M_1 \cdot f(x) \end{cases} \quad (\text{A.2})$$

therefore

$$A_C(x) = \frac{(P_0 - M_0) + (P_1 - M_1) \cdot f(x)}{(P_0 + M_0) + (P_1 + M_1) \cdot f(x)} \quad (\text{A.3})$$

Provided that $\lim_{x \rightarrow +\infty} |f(x)| = +\infty$ (which holds for all the fit functions we considered), it appears that A_C has an asymptote given by:

$$\lim_{x \rightarrow +\infty} A_C(x) = \frac{(P_1 - M_1)}{(P_1 + M_1)} \quad (\text{A.4})$$

The derivative of $A_C(x)$ can be expressed as:

$$\frac{dA_C(x)}{dx} = \frac{2 \cdot (P_1 M_0 - P_0 M_1) \cdot f'(x)}{[(P_0 + M_0) + (P_1 + M_1) \cdot f(x)]^2} \quad (\text{A.5})$$

Hence the condition to get a monotonically increasing $A_C(x)$ writes:

$$\frac{dA_C(x)}{dx} \geq 0 \iff (P_1 M_0 - P_0 M_1) \cdot f'(x) \geq 0 \quad (\text{A.6})$$

And finally, that fact that A_C can be fitted with the same functional form as $\sigma^+(x)$ and $\sigma^-(x)$ relies on the (approximate) fulfillment of the following second degree functional equation:

$$(A_1 M_1) \cdot (f(x))^2 + (A_0 M_1 + A_1 M_0 - P_1) \cdot f(x) + (A_0 M_0 - P_0) = 0 \quad (\text{A.7})$$

This equation has an analytical solution if its determinant is positive or null:

$$\Delta = \sqrt{(A_0 M_1 + A_1 M_0 - P_1)^2 - 4 \cdot (A_1 M_1) \cdot (A_0 M_0 - P_0)} \geq 0.$$

The fits of $\sigma^+(x)$, $\sigma^-(x)$ and A_C with the 3 considered functional forms are performed and the corresponding values of the fit parameters are presented in table 58.

Fit Parameter	Polynomial of $\text{Log}(Q)$	Polynomial of $\text{Log}(\text{Log}(Q))$	Laguerre Polynomials
P_0	0.33 ± 0.03	0.01 ± 0.03	0.79 ± 0.08
P_1	0.064 ± 0.004	0.43 ± 0.02	$(-2.9 \pm 1.5) \times 10^{-7}$
M_0	0.21 ± 0.02	0.04 ± 0.01	0.44 ± 0.04
M_1	0.032 ± 0.002	0.220 ± 0.006	$(-1.4 \pm 0.8) \times 10^{-7}$
A_0	0.258 ± 0.002	0.242 ± 0.002	0.283 ± 0.004
A_1	0.0036 ± 0.0002	0.023 ± 0.001	$(-1.6 \pm 0.8) \times 10^{-8}$

Table 58. Values of the fits parameters.

A.2.1 Polynomials of $\text{Log}(x)$

In this case, our toy model writes:

$$A_C(x) = \frac{(P_0 - M_0) + (P_1 - M_1) \cdot \text{Log}(x)}{(P_0 + M_0) + (P_1 + M_1) \cdot \text{Log}(x)} \quad (\text{A.8})$$

with

$$\frac{dA_C(x)}{dx} = \frac{2 \cdot (P_1 M_0 - P_0 M_1)}{x \cdot [(P_0 + M_0) + (P_1 + M_1) \cdot \text{Log}(x)]^2} \quad (\text{A.9})$$

and, since $x > 0$,

$$\frac{dA_C(x)}{dx} \geq 0 \iff (P_1 M_0 - P_0 M_1) \geq 0 \quad (\text{A.10})$$

Given the values of the fits parameters:

- the asymptoteic A_C is 33.0%
- $P_1 M_0 - P_0 M_1 = 2.51 \times 10^{-3} \geq 0$
- $\Delta = 3.12 \times 10^{-3} \geq 0$

Therefore $A_C(x)$ can be fitted by a first order polynomial of $\text{Log}(x)$, it's a monotonically increasing function, yet its has an asymptote.

A.2.2 Polynomials of $\text{Log}(\text{Log}(x))$

In this case, our toy model writes:

$$A_C(x) = \frac{(P_0 - M_0) + (P_1 - M_1) \cdot \text{Log}(\text{Log}(x))}{(P_0 + M_0) + (P_1 + M_1) \cdot \text{Log}(\text{Log}(x))} \quad (\text{A.11})$$

with

$$\frac{dA_C(x)}{dx} = \frac{2 \cdot (P_1 M_0 - P_0 M_1)}{x \cdot \text{Log}(x) \cdot [(P_0 + M_0) + (P_1 + M_1) \cdot \text{Log}(\text{Log}(x))]^2} \quad (\text{A.12})$$

and, since $x > 0$ (in practice $x > 10$ GeV) and $\text{Log}(x) > 0$,

$$\frac{dA_C(x)}{dx} \geq 0 \iff (P_1 M_0 - P_0 M_1) \geq 0 \quad (\text{A.13})$$

Given the values of the fits parameters:

- the asymptotic A_C is 32.6%
- $P_1 M_0 - P_0 M_1 = 1.57 \times 10^{-2} \geq 0$
- $\Delta = 0.144 \geq 0$

Therefore $A_C(x)$ can be fitted by a first order polynomial of $\text{Log}(\text{Log}(x))$, it's a monotonically increasing function, yet its has an asymptote.

A.2.3 Laguerre Polynomials $L_n(x)$

The toy model writes:

$$A_C(x) = \frac{(P_0 - M_0) + (P_1 - M_1) \cdot (1 - x)}{(P_0 + M_0) + (P_1 + M_1) \cdot (1 - x)} \quad (\text{A.14})$$

with

$$\frac{dA_C(x)}{dx} = \frac{-2 \cdot (P_1 M_0 - P_0 M_1)}{[(P_0 + M_0) + (P_1 + M_1) \cdot (1 - x)]^2} \quad (\text{A.15})$$

and,

$$\frac{dA_C(x)}{dx} \geq 0 \iff (P_1 M_0 - P_0 M_1) \leq 0 \quad (\text{A.16})$$

Given the values of the fits parameters:

- the asymptoteic A_C is 34.2%
- $P_1 M_0 - P_0 M_1 = -1.46 \times 10^{-3} \leq 0$
- $\Delta = 6.3 \times 10^{-14} \geq 0$

Therefore $A_C(x)$ can be fitted by a first order polynomial of $(1 - x)$, it's a monotonically increasing function, yet its has an asymptote.

We verified that for the case without longitudinal boost: $x_1 = x_2 = 1.15 \times 10^{-2}$, the conclusions listed above remain valid.

References

- [1] A. D. Martin, W. J. Stirling, R. S. Thorne and G. Watt, Eur. Phys. J. C **63** (2009) 189 [arXiv:0901.0002 [hep-ph]].
- [2] A. Cafarella, C. Coriano and M. Guzzi, Nucl. Phys. B **748** (2006) 253 [hep-ph/0512358].
- [3] G. Aad *et al.* [ATLAS Collaboration], Phys. Lett. B **701** (2011) 31 [arXiv:1103.2929 [hep-ex]].
- [4] S. Chatrchyan *et al.* [CMS Collaboration], Phys. Rev. Lett. **109** (2012) 111806 [arXiv:1206.2598 [hep-ex]].
- [5] S. Chatrchyan *et al.* [CMS Collaboration], arXiv:1312.6283 [hep-ex].
- [6] The LHCb Collaboration [LHCb Collaboration], “Updated measurements of W and Z production at $\sqrt{s} = 7$ TeV with the LHCb experiment,” LHCb-CONF-2011-039.
- [7] [ATLAS Collaboration], ATLAS-CONF-2011-129.
- [8] L. Schoeffel, Nucl. Instrum. Meth. A **423** (1999) 439.
- [9] M. Botje, Comput. Phys. Commun. **182** (2011) 490 [arXiv:1005.1481 [hep-ph]].
- [10] A. Djouadi *et al.* [MSSM Working Group Collaboration], hep-ph/9901246.
- [11] S. Muanza, GDR SUSY Internal Note, May 2000. Unpublished.
http://susy.in2p3.fr/GDR-Notes/GDR_SUSY_PUBLIC/GDR-S-076.ps.
- [12] G. P. Lepage, CLNS-80/447.
- [13] J. Alwall, P. Schuster and N. Toro, Phys. Rev. D **79** (2009) 075020 [arXiv:0810.3921 [hep-ph]].
- [14] B. Fuks, M. Klasen, D. R. Lamprea and M. Rothering, Eur. Phys. J. C **73** (2013) 2480 [arXiv:1304.0790 [hep-ph]].
- [15] C. Anastasiou, K. Melnikov and F. Petriello, “Fully differential Higgs boson production and the di-photon signal through next-to-next-to-leading order,” Nucl. Phys. B **724** (2005) 197 [arXiv:hep-ph/0501130].
- [16] S. Catani, L. Cieri, G. Ferrera, D. de Florian and M. Grazzini, “Vector boson production at hadron colliders: a fully exclusive QCD calculation at NNLO,” Phys. Rev. Lett. **103** (2009) 082001 [arXiv:0903.2120 [hep-ph]].
- [17] J. Pumplin, D. R. Stump, J. Huston, H. L. Lai, P. M. Nadolsky and W. K. Tung, JHEP **0207** (2002) 012 [hep-ph/0201195].
- [18] P. M. Nadolsky, H. L. Lai, Q. H. Cao, J. Huston, J. Pumplin, D. Stump, W. K. Tung and C.-P. Yuan, Phys. Rev. D **78** (2008) 013004 [arXiv:0802.0007 [hep-ph]].
- [19] A. Sherstnev and R. S. Thorne, Eur. Phys. J. C **55** (2008) 553 [arXiv:0711.2473 [hep-ph]].
- [20] A. D. Martin, R. G. Roberts, W. J. Stirling and R. S. Thorne, Phys. Lett. B **604** (2004) 61 [hep-ph/0410230].
- [21] T. Sjostrand, S. Mrenna and P. Z. Skands, “PYTHIA 6.4 Physics and Manual,” JHEP **0605** (2006) 026 [arXiv:hep-ph/0603175].
- [22] A.D. Martin, W.J. Stirling, R.S. Thorne, G. Watt, “Parton distributions for the LHC,” Eur. Phys. J. C **63** (2009) 189-285.

- [23] J. M. Campbell, J. W. Huston and W. J. Stirling, “Hard Interactions of Quarks and Gluons: A Primer for LHC Physics,” Rept. Prog. Phys. **70** (2007) 89 [arXiv:hep-ph/0611148].
- [24] M. R. Whalley, D. Bourilkov and R. C. Group, hep-ph/0508110.
- [25] G. Miu and T. Sjostrand, Phys. Lett. B **449** (1999) 313 [arXiv:hep-ph/9812455].
- [26] C. Balazs, J. Huston and I. Puljak, Phys. Rev. D **63** (2001) 014021 [arXiv:hep-ph/0002032].
- [27] G. Aad *et al.* [ATLAS Collaboration], arXiv:1103.1816 [hep-ex].
- [28] K. Nakamura *et al.* [Particle Data Group], J. Phys. G **37** (2010) 075021.
- [29] S. Ovin, X. Rouby and V. Lemaitre, arXiv:0903.2225 [hep-ph].
- [30] M. Dobbs, J. B. Hansen, Comput. Phys. Commun. **134** (2001) 41-46.
- [31] T. Schörner-Sadenius and S. Tapprogge, ATL-DAQ-2003-004.
- [32] M. Cacciari, G. P. Salam and G. Soyez, JHEP **0804** (2008) 063 [arXiv:0802.1189 [hep-ph]].
- [33] J. M. Campbell and R. K. Ellis, Phys. Rev. D **60** (1999) 113006 [arXiv:hep-ph/9905386].
- [34] J. M. Campbell and R. K. Ellis, Phys. Rev. D **62** (2000) 114012 [arXiv:hep-ph/0006304].
- [35] J. M. Campbell and R. K. Ellis, Phys. Rev. D **65** (2002) 113007 [arXiv:hep-ph/0202176].
- [36] W. Beenakker, M. Klasen, M. Kramer, T. Plehn, M. Spira and P. M. Zerwas, Phys. Rev. Lett. **83** (1999) 3780 [Erratum-ibid. **100** (2008) 029901] [arXiv:hep-ph/9906298].
- [37] W. Beenakker, M. Kramer, T. Plehn, M. Spira and P. M. Zerwas, Nucl. Phys. B **515** (1998) 3 [arXiv:hep-ph/9710451].
- [38] W. Beenakker, R. Hopker, M. Spira and P. M. Zerwas, Nucl. Phys. B **492** (1997) 51 [arXiv:hep-ph/9610490].
- [39] M. Spira, arXiv:hep-ph/0211145.
- [40] T. Plehn, Czech. J. Phys. **55** (2005) B213 [arXiv:hep-ph/0410063].
- [41] S. Gieseke *et al.*, arXiv:1102.1672 [hep-ph].
- [42] <http://cc.in2p3.fr/docenligne/13/en>
- [43] J. Ohnemus, Phys. Rev. D **47**, 940 (1993).
- [44] R. Hamberg, W. L. van Neerven and T. Matsuura, Nucl. Phys. B **359** (1991) 343 [Erratum-ibid. B **644** (2002) 403].
- [45] J. M. Campbell, R. Frederix, F. Maltoni and F. Tramontano, Phys. Rev. Lett. **102** (2009) 182003 [arXiv:0903.0005 [hep-ph]].
- [46] J. M. Campbell, R. K. Ellis and F. Tramontano, Phys. Rev. D **70** (2004) 094012 [arXiv:hep-ph/0408158].
- [47] R. Gavin, Y. Li, F. Petriello and S. Quackenbush, arXiv:1011.3540 [hep-ph].
- [48] S. Chatrchyan *et al.* [CMS Collaboration], JHEP **1110** (2011) 132 [arXiv:1107.4789 [hep-ex]].
- [49] Delphes ticket submitted and solved by S. Muanza,
<https://cp3.irmp.ucl.ac.be/projects/delphes/ticket/44>
- [50] M.L. Mangano,
<http://mlm.web.cern.ch/mlm/talks/lund-alpgen.pdf>

- [51] M.L. Mangano, M. Moretti, F. Piccinini and M. Treccani, JHEP **0701** (2007) 013 [hep-ph/0611129].
- [52] K. Cranmer, Statistical Problems in Particle Physics, Astrophysics and CosmoLogY, Conf. Proc. (2006) 112
- [53] RooStats Tutorial, K. Cranmer (2009)
http://root.cern.ch/root/html/tutorials/roostats/rs_numbercountingutils.C.html.
- [54] G. Aad *et al.* [ATLAS Collaboration], Eur. Phys. J. C **72** (2012) 2173 [arXiv:1208.1390 [hep-ex]].
- [55] G. Aad *et al.* [ATLAS Collaboration], ATLAS-CONF-2013-021.
- [56] G. Polesello and D. R. Tovey, JHEP **1003** (2010) 030 [arXiv:0910.0174 [hep-ph]].
- [57] D. R. Tovey, <http://projects.hepforge.org/mctlib>.
- [58] H. Baer, C. h. Chen, F. Paige and X. Tata, Phys. Rev. D **50** (1994) 4508 [hep-ph/9404212].
- [59] T. Aaltonen *et al.* [CDF Collaboration], Phys. Rev. D **83** (2011) 112003 [arXiv:1101.0034 [hep-ex]].
- [60] V. M. Abazov *et al.* [D0 Collaboration], Phys. Rev. D **84** (2011) 112005 [arXiv:1107.4995 [hep-ex]].
- [61] S. Knapen, Y. Zhao and M. J. Strassler, Phys. Rev. D **86** (2012) 014013 [arXiv:1111.5857 [hep-ph]].
- [62] S. Chatrchyan *et al.* [CMS Collaboration], Phys. Lett. B **717** (2012) 351 [arXiv:1206.3921 [hep-ex]].
- [63] N. Craig, C. Kilic and M. J. Strassler, Phys. Rev. D **84** (2011) 035012 [arXiv:1103.2127 [hep-ph]].
- [64] G. Aad *et al.* [ATLAS Collaboration], JHEP **1402** (2014) 107 [arXiv:1311.6724 [hep-ex]].
- [65] S. Chatrchyan *et al.* [CMS Collaboration], JHEP **1404** (2014) 191 [arXiv:1402.3803 [hep-ex]].
- [66] A. J. Barr, Phys. Lett. B **596** (2004) 205 [hep-ph/0405052].
- [67] J. M. Smillie and B. R. Webber, JHEP **0510** (2005) 069 [hep-ph/0507170].
- [68] T. Appelquist, H. C. Cheng and B. A. Dobrescu, Phys. Rev. D **64** (2001) 035002 [hep-ph/0012100].
- [69] S. Muanza [ATLAS Collaboration],
- [70] S. Muanza, In Turin 1996, Diquarks 3, 109-115
- [71] G. S. Muanza, PCCF-T-96-01.
- [72] H. Bachacou, I. Hinchliffe and F. E. Paige, Phys. Rev. D **62** (2000) 015009 doi:10.1103/PhysRevD.62.015009 [hep-ph/9907518].
- [73] G. Aad *et al.* [ATLAS Collaboration], Eur. Phys. J. C **74** (2014) 10, 3071 doi:10.1140/epjc/s10052-014-3071-4 [arXiv:1407.5063 [hep-ex]].
- [74] G. Aad *et al.* [ATLAS Collaboration], Eur. Phys. J. C **74** (2014) 11, 3130 doi:10.1140/epjc/s10052-014-3130-x [arXiv:1407.3935 [hep-ex]].
- [75] G. Aad *et al.* [ATLAS Collaboration], Eur. Phys. J. C **72** (2012) 2173 doi:10.1140/epjc/s10052-012-2173-0 [arXiv:1208.1390 [hep-ex]].

- [76] A. J. Barr and C. G. Lester, J. Phys. G **37** (2010) 123001
doi:10.1088/0954-3899/37/12/123001 [arXiv:1004.2732 [hep-ph]].
- [77] D. Curtin, Phys. Rev. D **85** (2012) 075004 doi:10.1103/PhysRevD.85.075004
[arXiv:1112.1095 [hep-ph]].
- [78] W. S. Cho, K. Choi, Y. G. Kim and C. B. Park, JHEP **0802** (2008) 035
doi:10.1088/1126-6708/2008/02/035 [arXiv:0711.4526 [hep-ph]].